THE UNIVERSITY OF CHICAGO

HYDROGEN EXCHANGE/MASS SPECTROMETRY ELUCIDATES DYNAMICS OF MEMBRANE PROTEINS BOTH IN VITRO AND IN VIVO

A DISSERTATION SUBMITTED TO

THE FACULTY OF THE DIVISION OF THE BIOLOGICAL SCIENCES

AND THE PRITZKER SCHOOL OF MEDICINE

IN CANDIDACY FOR THE DEGREE OF

DOCTOR OF PHILOSOPHY

GRADUATE PROGRAM IN BIOCHEMISTRY AND MOLECULAR BIOPHYSICS

BY

XIAOXUAN LIN

CHICAGO, ILLINOIS

MARCH 2024

To my parents

All models are wrong, some are useful.

George Box

TABLE OF CONTENTS

LIST OF FIGURES viii

LIST OF TABLES x

ACKNOWLEDGMENTS xi

ABSTRACT xiii

1 INTRODUCTION 1

1.1 Introduction to HDX-MS 1
1.2 Current challenges of conducting HDX-MS on complex biological systems 4

2 HDX-MS ON A PIEZOELECTRIC MOTOR PRESTIN AND OUTER HAIR CELL ELECTROMOTILITY 8

2.1 Folding of Prestin's Anion-Binding Site and the Mechanism of Outer Hair Cell Electromotility 9
2.1.1 Abstract 10
2.1.2 Introduction 11
2.1.3 Results 13
2.1.3.1 Prestin's anion-binding site is less stable than SLC26A9's. 14
2.1.3.2 Anion binding drives the folding of prestin's binding site. 19
2.1.3.3 Prestin in a lipid bilayer exhibits a highly dynamic TM6. 22
2.1.3.4 Incremental unfolding of prestin's binding site versus cooperative unfolding of the lipid-facing helices. 24
2.1.4 Discussion 27
2.1.4.1 Structure of prestin in HEPES and low Cl^- levels 32
2.1.5 Conclusions 33
2.1.6 Materials and Methods 33
2.1.7 Acknowledgments 41
2.1.8 Data availability 41
2.1.9 Supporting information 41
2.1.9.1 Supporting Information Text 1: Heterogeneity and HDX kinetics. 41
2.1.9.2 Supporting Information Text 2: Combining HDX-MS and cryo-EM in structural biology. 43
2.1.9.3 Supporting Information Text 3: Structure of prestin in HEPES and low Cl^- levels. 45
2.1.10 Supplementary figures 46

3 DEVELOPMENT AND APPLICATIONS OF IN VIVO HDX-MS 67

3.1 Development of *in vivo* HDX-MS with applications to a TonB-dependent transporter and other proteins. 68
3.1.1 Abstract 69
3.1.2 Importance 69

3.1.3 Introduction 70
3.1.4 Results 72
3.1.4.1 The in vivo allosteric response of BtuBp to B12 binding. 73
3.1.4.2 In vivo HDX of endogenous proteins co-measured with BtuB. 75
3.1.5 Discussion 75
3.1.5.1 HDX Protocol considerations 76
3.1.6 Conclusion 78
3.1.7 Materials and methods 78
3.1.8 Author Contributions 80
3.1.9 Acknowledgments 81
3.1.10 Figures and Tables 82
3.1.11 Supplementary figures 86
3.1.12 References 93
3.2 HDX-MS conducted on yeast Pab1 in live bacteria 96
3.2.1 Summary 96
3.2.2 Motivation 96
3.2.3 Materials and methods 97
3.2.4 HDX results and discussion 99
3.2.4.1 Peptide assignments for Pab1 from in vivo HDX 99
3.2.4.2 Soluble Pab1 had a less dynamic RRM2 in live cells than purified soluble Pab1 100

4 PUSHING THE TECHNIQUE OF HDX-MS TO MEMBRANE PROTEINS IN NANODISCS AND LIPOSOMES 103

4.1 Advancing the technique of HDX-MS on membrane proteins in a lipid bilayer 103
4.1.1 Motivations 103
4.1.2 Proteoliposome sample preparation for HDX-MS 105
4.1.3 Optimize protease digestion and signal-to-noise for membrane proteins in liposomes 107
4.1.3.1 Quench conditions and detergents 108
4.1.3.2 Protease and protease cartridges 114
4.1.3.3 LC and carryover 116
4.1.4 Summary of the optimized HDX-MS protocol for KvAP 123
4.2 Probing voltage-dependent conformation changes of KvAP using HDX-MS under an applied electric field 124
4.2.1 Abstract 124
4.2.2 Introduction 125
4.2.3 Results 129
4.2.3.1 Establishing a membrane potential 129
4.2.3.2 Obtaining a peptide map for KvAP 130
4.2.3.3 HDX-MS on KvAP liposomes under membrane potential 132
4.2.4 Discussion and next steps 136
4.2.5 Materials and methods 139
4.2.5.1 KvAP expression and purification 139
4.2.5.2 KvAP proteoliposome reconstitution 140

4.2.5.3 HDX-MS on KvAP 141
4.2.6 Supplementary figures 141
5 EFFECTS OF BIOLOGICAL SOLVENTS ON THE FOLDING OF PROTEIN BACKBONES 143
5.1 Summary 143
5.2 Does a polypeptide backbone contract in water and in biological solvents? 143
5.2.1 Introduction 143
5.2.2 Results 144
5.2.3 Discussion 149
5.2.4 Materials and methods 150
5.2.5 Supplementary figures 151
5.3 Contribution to the publication Baxa M., Lin X., et al., 2024 152
6 CONCLUSIONS AND FUTURE DIRECTIONS 154
REFERENCES 157

LIST OF FIGURES

Figure 1.1 General concept, workflow, and example data for HDX-MS. 4
Figure 2.1: Distinct HDX response of prestin and SLC26A9 to Cl- binding. 15
Figure 2.2: The anion-binding pockets for prestin and SLC26A9 exhibit distinct stability changes upon Cl- binding, albeit highly conserved. 16
Figure 2.3: Anion binding folds and stabilizes prestin's binding site. 19
Figure 2.4: Prestin's dynamics are regulated by anions of varying identities. 21
Figure 2.5: Prestin in nanodisc displays similar folding stability to prestin in micelle, except for a more dynamic TM6. 23
Figure 2.6: Helix folding cooperativity and the proposed mechanism for prestin's electromotility. 25
Figure 2.7: Volcano plot analysis of HDX for prestin (A) and SLC26A9 (B) in response to Cl- binding. 46
Figure 2.8: Site-resolved protection factors for prestin and SLC26A9 obtained using PyHDX. 47
Figure 2.9: PyHDX fitting supports that prestin exhibits helix fraying at the N-terminus of TM3 and mild cooperativity at the intracellular portion of TM6. 48
Figure 2.10: Mammalian prestin has a conserved and helix-destabilizing proline 136 on TM3. 49
Figure 2.11: HDX-MS sequence coverage and measurements for prestin and SLC26A9 in Cl-. 50
Figure 2.12: Regions unresolved in cryo-EM structures are unfolded in all conditions examined. 51
Figure 2.13: HDX for prestin occurs via EX2 mechanism. 52
Figure 2.14: Heterogeneity and HDX kinetics in TM1 and TM9. 53
Figure 2.15: Deuterium uptake curves for all peptides covering prestin's transmembrane domain. 54
Figure 2.16: Deuterium uptake curves for all peptides covering SLC26A9's transmembrane domain. 60
Figure 2.17: The cryo-EM structure for prestin in a HEPES-based buffer containing 1 mM Cl- (blue; PDB 8UC1) highly resembles the structure in the reported Cl--bound state. 63
Figure 2.18: Workflow for the processing of the cryo-EM data. 64
Figure 3.1: Experimental workflow and sequence coverage for in vivo HDX-MS on BtuB. 82
Figure 3.2: Effects of B12 binding on BtuBp's HDX measured in vivo and in vitro. 83
Figure 3.3: B12 binding induces unfolding of the Ionic Lock region of BtuBp in vivo similarly to in vitro. 84
Figure 3.4: HDX of endogenous E. coli proteins measured in experiments targeting BtuB. 85
Figure 3.5: BtuBp's HDX is independent of the choice of carbon source within sampled label times. 86
Figure 3.6: Mass spectra of a set of representative peptides. 87
Figure 3.7: B12 binding-induced dynamics in BtuBp are insensitive to dissipation of the proton motive force via CCCP. 88
Figure 3.8: HDX back exchange occurs primarily during the post-quench sample work-up. 89
Figure 3.9: Uptake curves for all available BtuBp peptides. 90
Figure 3.10: SDS-PAGE gel showing samples used for in vivo HDX-MS of Pab1. 100

Figure 3.11: Uptake plots for representative peptides at RRM1 (A) and RRM2 (B) comparing Pab1 HDX in vivo and in purified proteins. 101
Figure 3.12: Woods plot showing the %D differences for Pab1 labeled in vivo and as purified proteins. 101
Figure 3.13: Pab1 in live *E. coli* exhibits conformational heterogeneity at the C-terminus. 102
Figure 4.1 Elution profile of the quench buffer containing C12E8 (top, black) and KvAP peptides quenched with C12E8 (bottom, red). 113
Figure 4.2: Ribbon representation of KvAP cryo-EM structure. 128
Figure 4.3: Ratiometric fluorescence measurements of membrane potential. 130
Figure 4.4: Modified workflow for running KvAP proteoliposome samples in LC-MS. 131
Figure 4.5: The sequence coverage of KvAP. 132
Figure 4.6: HDX for the voltage-sensing domain of KvAP. 134
Figure 4.7: HDX for the pore domain and the termini of KvAP. 135
Figure 4.8: Site resolved HDX for the selectivity filter of KvAP. 135
Figure 4.9: 4-20% gel for KvAP Co purification. 141
Figure 4.10: SEC chromatogram for liposome reconstitution of KvAP. 142
Figure 4.11: 4-20% gel for liposome reconstitution of KvAP (lanes 9-12). 142
Figure 5.1: The crystal structure of sfAFP under oxidizing conditions (PDB 2PNE). 144
Figure 5.2: CD and NMR hetNOE measurements showing red-sfAFP is unfolded. 145
Figure 5.3: HSQC spectra and HX rates of red-sfAFP are unaffected by the presence of biological solvents. 147
Figure 5.4: The glycine-clustered mutant of red-sfAFP did not form hydrogen-bonds and were unstructured. 147
Figure 5.5: SAXS measurements on mutants of red-sfAFP containing various glycine stretches show SARW behaviors. 149
Figure 5.6: Fitting HX rates for the CLEANEX-PM measurements on red-sfAFP. 151
Figure 5.7: Protection factors for red-sfAFP are less than 2. 152
Figure 5.8: Sequences of red-sfAFP and its variants used in this study. 152

LIST OF TABLES

Table 1: Biochemical and statistical details for HDX 65
Table 1: Biochemical and statistical details for HDX 65
Table 2: HDX summary table. 91
Table 3: Top 20 E. coli K12 proteome search hits ranked by the number of identified peptides. 92
Table 4: Detergent screening in the quench buffer to increase the signal-to-noise of KvAP peptides. 112
Table 5: Wash solutions tested to reduce KvAP carryover from the LC columns. 120
Table 6: Conditions tested to further reduce KvAP carryover. 122

ACKNOWLEDGMENTS

This work would not be possible without the aid and contributions from my mentors, colleagues, friends, and family. I would like to first thank my thesis advisor, Dr. Tobin Sosnick, who introduced to me the world of biophysics, a field I have been fascinated with and decided to continue pursuing after my graduation at The University of Chicago. My initial encounter with Tobin was at the interview for the graduate program admission in early 2019. I was greatly impacted, slightly shocked, by his strong desire to talk about science and work being done in his laboratory. It was not a joke to say that I was not the person being interviewed there. Tobin's enthusiasm and constant excitement about science drove me into his laboratory and has influenced me to always be excited about asking questions and making scientific discoveries. Each conversation with Tobin had sparked a little idea to solve problems or some seemingly crazy ideas that I later went on testing and produced findings that are in fact groundbreaking.

I would also like to thank my collaborators and mentors, Dr. Eduardo Perozo and Dr. Navid Bavi, who have taught me everything about membrane proteins, systems that again I decided to pursue for the continuation of my scientific career. The fact that we each think about a biological question from distinct perspectives has made this collaboration the best experience I have had. I am grateful that I was accessible to knowledge from both Sosnick and Perozo Labs which are highly complementary and insightful.

My gratitude extends to the rest of my committee, Dr. Rama Ranganathan and Dr. Francisco Bezanilla, for their guidance throughout my scientific journey. Their valuable insights have helped me grow into a more independent thinker and scientist.

I would like to thank all members of the Sosnick Lab, not just as colleagues but as my dearest friends – Isabelle Haskins for always making the lab a pleasant workplace and never saying no to offer a favor; Dr. Michael Baxa for keeping our beast mass spectrometry running; Dr. Adam Maciek Zmyslowski and Dr. Ruofan Chen for accompanying through the early mass spectrometry times when we had to learn everything in dark; Dr. Andrew Molina, Dr. Hendrick Glauninger, Abigail Schroeter, Julia Shangguan, Noah Schwartz, and Estefania Cuevas-Zepeda for more mass spectrometry times and accompanying along the journey to solve "the lipid problem"; Dr. Xiangda Peng, Dr. Nabil Faruk, and Yiheng Wu for mentoring and assisting me with coding and learning molecular dynamics simulations; Viridiana Leon for being a great listener and glue to bring everyone together. I would also like to thank "the NMR Joe", Dr. Joseph Sachleben, for introducing me to the world of NMR – I always enjoy you stopping by the lab. I would like to thank my peer Patrick Haller in the Perozo Lab for being a productive and always trustworthy collaborator.

Lastly, I would like to thank my family and parents in China, especially my mother YUAN Haijing. You are always my inspiration for being a strong and independent woman. Thank you for always supporting me, no matter what decisions I make, even when it may seem like I am taking the long way. Although we couldn't see each other in person very often, knowing that you are always there for me, welcome me, and support me makes me the strongest woman I could ever be to face all challenges in front of me while I am away from home. I love you and will always be there for you, just as you have always been for me.

ABSTRACT

Membrane proteins (MPs) are critical contact points for transducing environmental cues across cell membranes and hence have become major pharmaceutical targets. Despite recent advances in structural biology, elucidation of MP function and mechanisms remains challenging partly because structures only represent static snapshots at the endpoints of protein dynamics, while the higher complexity of MPs requires exploration of the full energy landscape. My thesis aims to advance our understanding of MP mechanisms by non-invasively probing MP dynamics in solution using hydrogen-deuterium exchange coupled with mass spectrometry (HDX-MS).

The main project details investigation of the thermodynamics and dynamics of prestin, whose voltage-dependent conformational changes underlie the acute hearing sensitivity for mammals. We find that the conformational stability of the helices associated with the anion-binding site accounts, in large part, for prestin's distinct differentiation from its transporter-evolutionary origin. Our results argue that the folding equilibrium of the anion-binding site plays a novel and central role in prestin's voltage-sensing mechanism and electromotility.

Additionally, we present the development and application of *in vivo* HDX-MS to BtuB, a TonB-dependent B12 transporter found in *E. coli* outer membranes. HDX-MS measured in living *E. coli* cells showed that B12 alone is sufficient to break a critical salt bridge in BtuB, leading to the unfolding of the amino terminus for TonB binding. The ability to measure HDX *in vivo* is generalizable which opens up a wide range of HDX studies on proteins in their native context.

Overall, our studies on prestin have deepened our understanding of mammalian hearing sensation. We have significantly advanced the utility of HDX-MS to *in vivo* systems and MPs

embedded in lipid bilayers. This work on HDX-MS and MPs have advanced our knowledge of MP functions and mechanisms from a distinct thermodynamic perspective.

1 INTRODUCTION

Hydrogen-deuterium exchange mass spectrometry (HDX-MS) is a powerful biophysical tool for nonperturbatively probing the thermodynamics and dynamics of biomolecules, particularly proteins, through isotope labeling. In recent decades, there have been burgeoning applications of HDX-MS including epitope mapping, protein-protein interactions, protein-small molecule interactions, as well as protein structures and mechanisms.[1] In this chapter, I will first provide an overview of HDX-MS from chemistry and technique perspectives, followed by a discussion of the current challenges in the application of HDX-MS to answer complex biological questions.

1.1 Introduction to HDX-MS

The basic principle of HDX-MS lies in hydrogen exchange (HX), a spontaneous exchange process between protons on the protein amide backbone and protons in the aqueous solvent. The phenomenon of HX can be simply described as a thermodynamic tug-of-war defined by the protein transfer theory, in which the proton acceptor and donor collide, redistribute the proton, and separate.[2] The probability of exchange is largely defined by the relative acidity of the amide proton and the solvent proton, i.e., ΔpKa. Here I provide a brief introduction to HX and HDX-MS in the context of general application to biomolecules.

Under physiological conditions and most experimental conditions, the pH of the environment is near neutral, where HX is mainly catalyzed by base OH^-. As one increases the pH by one unit, the concentration of OH^- increases by 10-fold, leading to the same 10-fold increase in the HX rate. In addition to pH, the exchange rate rises with temperatures, following the Erying equation.[3]

Since HX occurs spontaneously as a result of thermal fluctuations, one can obtain the thermodynamic and dynamic information for a protein in solution without incorporating synthetic labels. These features have presented HX with large advantages over other methods. For example, structural methods including X-ray crystallography and cryo-EM only probe the static snapshots of proteins at their low energy states, either under highly nonnative chemical environments or under cryogenic conditions. One of the most pervasively used solution-based approaches to study the conformational dynamics of membrane proteins is electron paramagnetic resonance spectroscopy (EPR).[4] However, EPR requires generating multiple site-directed mutations and, apart from the possibility of disrupting a protein's native structure, is rather low throughput.[4]

HX has been greatly coupled with NMR for measurement. H-to-H exchange can be measured by a common NMR method named "CLEANEX-PM", which selectively magnetizes protons from water and measures the appearance of protons associated with nitrogen over time. HX/NMR can usually provide single residue resolution but is only applicable for small proteins. For proteins with more than 250 amino acids, mass spectrometry (MS) is used for measurement and one needs to transfer the protein into a D_2O solvent so that the H-to-D exchange can be measured by MS as a mass increase by one Dalton. This experiment is what we call HDX-MS and is the main method I aim to develop and apply throughout my doctoral training.

For a folded protein, the amide protons engage in the hydrogen-bonding network as proton donors to form the secondary structures of the protein. Protons involved in hydrogen bonds do not exchange with solvent protons. However, backbone hydrogen bonds can transiently break due to native thermal fluctuations of a protein, exposing the amide protons for exchange with deuteriums in the solvent before the hydrogen bonds reform (Figure 1.1). Therefore, HDX measures the

stability of the amide hydrogen bonds, rather than the solvent accessibility of the protein, although it can affect the stability. Since the observed HDX rate is a product of the fraction of time when hydrogen bonds are broken and k_{chem}, the intrinsic exchange rates when there is no formed hydrogen bond,[5,6] one can measure the free energy of unfolding for the protein through HDX studies. The free energy of unfolding, importantly, underlies the energetic landscape of a protein and its motions necessary for biological functions.

The general concept and workflow of HDX-MS are provided in Figure 1.1 with example data. HDX reaction is initiated by diluting a protein in an aqueous solvent to a buffer made with D_2O. After a defined amount of exchange time, the reaction is quenched with low temperature and low pH (pH=2.5), under which the exchange rate is greatly reduced. The protein is then digested into peptides by aspartic proteases. The resulting peptides are separated by liquid chromatography and their mass is measured by the MS. The common method for calculating the deuteration levels is to first fit the isotopic envelope with a binomial distribution, and compare the centroid of the peptides before and after deuterium uptake. After correcting for the back-exchange and in-exchange levels, which are deuterium loss and gain during and after the quench step, respectively, one can quantitatively measure the exchange rates and the free energy of unfolding either at the resting state or at various excited states.

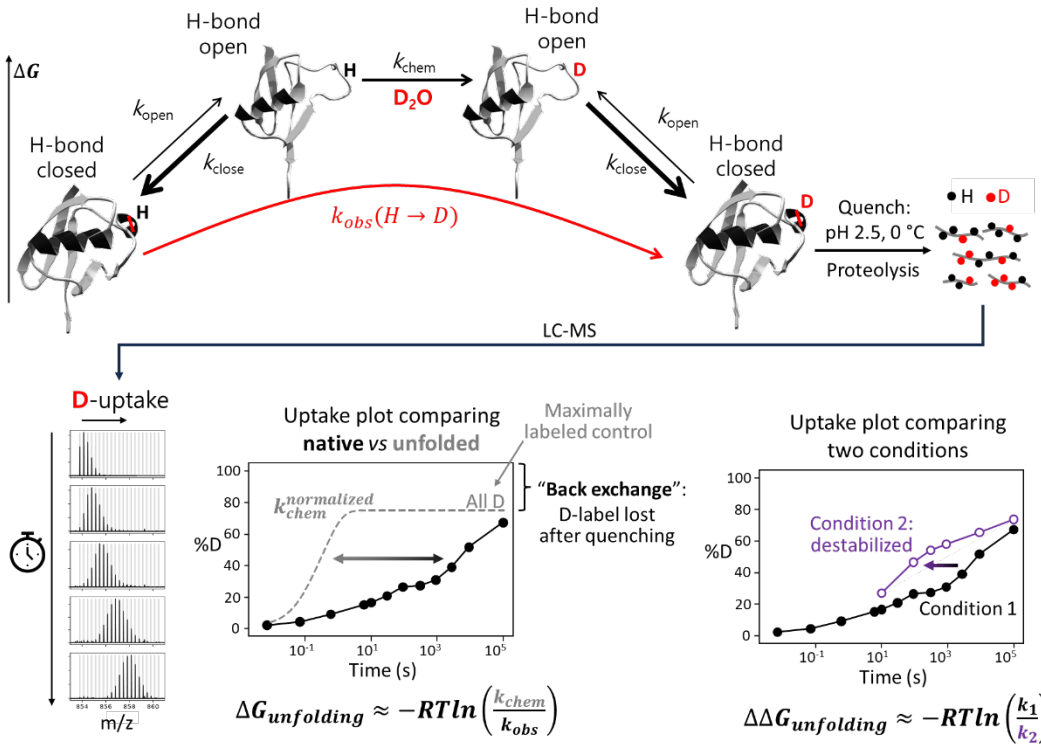

Figure 1.1 General concept, workflow, and example data for HDX-MS.

1.2 Current challenges of conducting HDX-MS on complex biological systems

HDX-MS has been mostly used to study folding and dynamics of soluble proteins[7] and aggregation-prone intrinsic disordered proteins.[8,9] In the past decade, HDX-MS has been increasingly applied to complex biological systems, including antibody-antigen interactions, biomolecular condensates,[10] and membrane proteins.[11,12]

Distinct challenges have been presented to researchers in various fields trying to expand the application of HDX-MS. Among the various difficulties, enzymatic digestion is the major issue that hinders the progression of HDX-MS studies, as peptides covering the region of interest may not be detected or have low redundancy. As a result, information regarding changes in hydrogen

bonding patterns in certain residues is lost or suffers from low confidence. Poor digestion can originate from multiple reasons, including post-translational modifications, poor solubility of protein condensates and membrane proteins, and protection of membrane mimetic molecules such as detergents and lipids preventing the access of proteases to proteins. Since my dissertation is focused on HDX-MS on integral membrane proteins and HDX-MS in vivo, below I extend the discussion of the current challenges in these two areas.

Firstly, the main challenge of HDX-MS on integral membrane proteins revolves around the poor solubility of the biological system in aqueous solvents. Integral membrane proteins have a large lipophilic surface area that greatly favors interactions with nonpolar over polar solvents. This necessitates the employment of highly hydrophobic molecules, usually detergents or lipids, to assist the proper folding and function of a membrane protein. To achieve efficient enzymatic digestion for a high sequence coverage and redundancy, one needs to unfold a membrane protein after or during quenching to provide sufficient access of the protease to the protein backbone. However, the folding and unfolding processes of membrane proteins are poorly understood especially for alpha-helical membrane proteins. Methods to unfold soluble proteins, including temperature denaturation and chemical denaturation using chaotropes, often induce severe aggregation of alpha-helical membrane proteins.

Additionally, the presence of detergents or lipids, which are required to solvate membrane proteins, presents great challenges to the liquid chromatography (LC) system and the MS. For HDX-MS studies, bottom-up MS is usually employed in which peptides are separated by LC and analyzed by the MS. Most often reverse phase (RP) chromatography which involves a gradient of an apolar solvent from a polar solvent, commonly from water to acetonitrile (ACN), is used for

the separation of peptides. Detergents and lipids, however, bind strongly to RP columns, especially C8 and C18 columns that are commonly used to separate peptides, due to their long alkyl chains and elute very slowly under the flow of high ACN concentrations. The tight binding and the broad elution profile of detergents and lipids cause a variety of problems to the LC-MS, including column fouling, signal suppression to peptides, and MS contamination.

More discussion regarding the technical challenges of membrane proteins on LC-MS and my attempts to resolve them are provided in Chapter 4 "Pushing the technique of HDX-MS to membrane proteins in nanodiscs and liposomes".

Another challenge in the current application of HDX-MS involves the attempt to push the technique in vivo. Note that the in vivo here means HDX conducted on live cells, instead of live animals. Due to the reversible nature of HDX labels, all HDX experiments suffer from the issue of back exchange. For a standard HDX-MS study, proteins in quenched HDX reactions are immediately proteolyzed and subject to LC-MS analysis. For HDX in live cells, since D_2O is permeable to cell membranes with a time constant of ~100 ms, initiation of the HDX reaction is as simple as diluting cells into a D_2O-based solution. However, one cannot immediately proteolyze nor analyze the deuteration levels without lysing the cells and isolating the protein(s) of interest to some degree. The purification process therefore now has to be performed after quenching, under a low pH and a low temperature, and as fast as possible to minimize back exchange. Although back exchange only affects the magnitudes of deuteration levels, not the rates of exchange, small but significant changes in the exchange rates induced by condition changes will become less detectable. In Chapter 3 "Development and applications of in vivo HDX-MS", I present the first in vivo HDX-MS study on a membrane protein with a protocol that reduces back exchange to a manageable

level under which we can detect unfolding events induced by ligand binding.

2 HDX-MS ON A PIEZOELECTRIC MOTOR PRESTIN AND OUTER HAIR CELL ELECTROMOTILITY

This chapter is the publication by Lin, Xiaoxuan, Patrick R Haller, Navid Bavi, Nabil Faruk, Eduardo Perozo, and Tobin R Sosnick. “Folding of Prestin’s Anion-Binding Site and the Mechanism of Outer Hair Cell Electromotility.” Edited by Stephan A Pless and Merritt Maduke. *eLife* 12 (December 6, 2023): RP89635. https://doi.org/10.7554/eLife.89635**.**

2.1 Folding of Prestin's Anion-Binding Site and the Mechanism of Outer Hair Cell Electromotility

Xiaoxuan Lin[1,2], Patrick Haller[1,2], Navid Bavi[1,2], Nabil Faruk[1], Eduardo Perozo[1,2,3,4,*], Tobin R. Sosnick[1,2,4,5,*]

[1]Department of Biochemistry and Molecular Biology, [2]Center for Mechanical Excitability, [3]Institute for Neuroscience, [4]Institute for Biophysical Dynamics, [5]Pritzker School for Molecular Engineering, The University of Chicago, Chicago, Illinois, USA

*Corresponding authors: trsosnic@uchicago.edu; eperozo@uchicago.edu.

Author Contributions: X.L., E.P., and T.R.S. designed research; X.L., P.H., N.B., and N.F. performed research; X.L., E.P., and T.R.S. analyzed data; and X.L., E.P., and T.R.S. wrote the paper.

Competing Interest Statement: The authors declare no competing interest.

Keywords: Mass spectrometry, hydrogen exchange, cochlear amplification, electromotility

2.1.1 Abstract

Prestin responds to transmembrane voltage fluctuations by changing its cross-sectional area, a process underlying the electromotility of outer hair cells and cochlear amplification. Prestin belongs to the SLC26 family of anion transporters yet is the only member capable of displaying electromotility. Prestin's voltage-dependent conformational changes are driven by the putative displacement of residue R399 and a set of sparse charged residues within the transmembrane domain, following the binding of a Cl^- anion at a conserved binding site formed by amino termini of the TM3 and TM10 helices. However, a major conundrum arises as to how an anion that binds in proximity to a positive charge (R399), can promote the voltage sensitivity of prestin. Using hydrogen-deuterium exchange mass spectrometry, we find that prestin displays an unstable anion-binding site, where folding of the amino termini of TM3 and TM10 is coupled to Cl^- binding. This event shortens the TM3-TM10 electrostatic gap, thereby connecting the two helices, resulting in reduced cross-sectional area. These folding events upon anion-binding are absent in SLC26A9, a non-electromotile transporter closely related to prestin. Dynamics of prestin embedded in a lipid bilayer closely match that in detergent micelle, except for a destabilized lipid-facing helix TM6 that is critical to prestin's mechanical expansion. We observe helix fraying at prestin's anion-binding site but cooperative unfolding of multiple lipid-facing helices, features that may promote prestin's fast electromechanical rearrangements. These results highlight a novel role of the folding equilibrium of the anion-binding site and helps define prestin's unique voltage-sensing mechanism and electromotility.

2.1.2 Introduction

Hearing sensitivity in mammals is sharply tuned by a cochlear amplifier associated with electromotile length changes in outer hair cells.[13] These changes are driven by prestin (SLC26A5), a member of the SLC26 anion transporter family, which converts voltage-dependent conformational transitions into cross-sectional area changes, affecting its footprint in the lipid bilayer.[14] This process plays a major role in mammalian cochlear amplification and frequency selectivity, with prestin knockout producing a 40-60 dB signal loss in live cochleae.[15] Unlike most molecular motors, where force is exerted from chemical energy transduction, prestin behaves as a putative piezoelectric device, where mechanical and electrical transduction are coupled.[16] As a result, prestin functions as a direct voltage-to-force transducer. Prestin's piezoelectric properties are unique among members of the SLC26 family, where most function as anion transporters.

Recent structures determined by cryo-electron microscopy (cryo-EM) have sampled prestin's conformational space under various anionic environments and located the anion-binding site at the electrostatic gap between the amino termini of TM3 and TM10 helices.[17–19] This anion-binding pocket is highly conserved, and is influenced by surrounding hydrophobic residues in TM1 and by a fixed positive charge from residue R399 on TM10. Movements of this binding site are coupled to the complex reorientation of the core domain relative to the gate domain,[17,18] reminiscent of the conformational transitions in transporters displaying an elevator-like mechanism.[20] Prestin exhibits minimal transporter ability yet is structurally similar to the non-electromotive anion transporter SLC26A9 (sequence identity = 34%; Cα RMSD = 3.4 Å for the transmembrane domain (TMD), PDB: 7S8X and 6RTC).[19,21,22] Questions remain as to the molecular basis underlying the distinct functions of the two proteins. Importantly, the role of bound

anions, which is required for prestin electromotility,[23] is still elusive.

Prestin's voltage dependence is tightly regulated by intracellular anions of varying valence and structure,[24,25] whereas anion affinity is also regulated by voltage and tension.[26] These phenomena suggest that anions, rather than behaving as explicit gating charges, may serve as allosteric modulators.[26] Incorporating a fixed charge alternative to a bound anion through an S398E mutation preserves prestin's nonlinear capacitance (NLC) but results in insensitivity to salicylate, a strong competing anionic binder.[19] Except for residue R399, charged residues located in the TMD distribute towards the membrane-water interface[17–19] and display minimal contributions to the total gating charge estimated from NLCs.[27] Electrostatic calculations show that R399 has a strong contribution to the local electrostatics at the anion-binding site, by providing ~40% of the positive charge at the bilayer mid-plane.[17] However, the existing structural and functional data cannot explain why prestin's voltage dependence requires close proximity of both a negative charge (the bound anion or S398E)[23] and a positive charge (R399[17,28]). The resolution of this conundrum will define an essential step towards our understanding of prestin's unique voltage-sensing mechanism.

Here we studied the influence of anion-binding on the dynamics and structural changes of prestin as a function of anions (Cl^-, SO_4^{2-}, salicylate, and HEPES) via hydrogen-deuterium exchange mass spectrometry (HDX-MS). The HEPES condition was achieved by Cl^- removal (dialysis), which inhibits prestin's NLC.[23] In a HEPES-based buffer, prestin's NLC shifts to depolarized potentials, associated to a more expanded state at 0 mV that is coupled to low anion affinity.[24,25] Based on the above studies and the large size of HEPES anions, we assumed minimal binding of HEPES anions to prestin and hence associated HEPES condition to a putative apo state in this study. By comparing the dynamics of prestin with its close non-piezoelectric relative, the

anion transporter SLC26A9, we identified distinct features unique to prestin, including a relatively unstable anion-binding site that folds upon binding, thereby allosterically modulating the dynamics of the TMD. In contrast, the stability and hydrogen-bond pattern of SLC26A9's anion-binding site were minimally affected by anion binding, albeit displaying high similarities to prestin in both structure and sequence. Prestin reconstituted in nanodisc exhibited indistinguishable dynamics compared to detergent-solubilized prestin, except for a destabilized TM6 which mediates prestin's mechanical expansion.[17] We observed fraying of the helices involved in the binding site whereas cooperative unfolding of multiple lipid-facing helices including TM6, which may explain prestin's fast and large-scale motions. These results highlight the significance of the anion-binding site's folding equilibrium in defining the unique properties of prestin's voltage dependence and electromotility.

2.1.3 Results

We carried out HDX measurements on dolphin prestin and mouse SLC26A9 solubilized in glyco-diosgenin (GDN) at either pD_{read} 7.1, 25 °C or pD_{read} 6.1, 0 °C (Table 1). The observed HDX rates reported on the stability, as exchange occurred mostly via EX2 kinetics (**Supporting Information Text 1**). Employment of the two conditions increased the effective dynamic range of the HDX measurement to span seven log units, allowing us to determine the stability of both the highly and minimally stable regions within the protein.[29] To properly combine the two datasets, the stability of the protein should be the same under the two conditions, and this was supported by the exchange rates scaling with k_{chem} (intrinsic exchange rates) (Figure 2.13).[5,6]

The HDX data were presented in terms of the relevant region with the specific sequence

and peptides noted in parentheses (**Materials and Methods**), e.g., the N-terminus of prestin's TM10 ($Region_{394–397}$: $Peptide_{392–397}$). Although we mostly focused on the anion-binding site, we also obtained comparative thermodynamic information throughout the two proteins (**Supporting Information Text 2**).

2.1.3.1 Prestin's anion-binding site is less stable than SLC26A9's.

To examine the effect of anion binding to the dynamics of prestin and SLC26A9, we dialyzed the proteins purified in Cl^- into a HEPES buffer lacking other anions. Cl^- removal resulted in distinct stability changes for prestin and SLC26A9, manifested by significant HDX acceleration for prestin while mild HDX slowing for SLC26A9 (Figure 2.1 & Figure 2.7). These HDX effects indicate that anion binding induced global stabilization for prestin while slight destabilization for SLC26A9 (Figure 2.1).

Among the observed HDX responses for prestin, the HDX acceleration at the anion-binding pocket appeared to be the most pronounced and indicates local stabilization induced by anion binding (Figure 2.2 A). In detail, HDX accelerated by 20-fold for the N-termini of both TM3 ($Region_{136-142}$: $Peptide_{134-142}$ + 9 other peptides) and TM10 ($Region_{394–397}$: $Peptide_{392–397}$) (Figure 2.2 & Figure 2.15 S9.22-9.31). This HDX change translates to a difference in free energy of unfolding (ΔΔG) by at least 1.8 kcal/mol; $\Delta\Delta G^{\text{binding site}}_{\text{Cl binding}} = 1.8$ kcal/mol. At least four residues in the middle of TM1 exhibited faster HDX ($Region_{90-101}$: $Peptide_{88-101}$ + 10 other peptides), collectively by 350-fold; $\Delta\Delta G^{\text{TM1}}_{\text{Cl binding}} = 3.5$ kcal/mol (Figure 2.1 A & Figure 2.15 S9.6-9.16). The TM1 region with accelerated HDX included L93, Q97, and F101, residues that are known to participate in the binding pocket.[17,18,30]

SLC26A9 exhibited similar stability as prestin in Cl^- for the majority of the TMD, except for the N-terminal TM3 ($Region_{131-134}$: $Peptide_{129-134}$) which exchanged at least 100-fold slower than that of prestin's ($Region_{136-142}$: $Peptide_{134-142}$) (Figure 2.2). This difference in HDX points to a relatively unstable anion-binding site of prestin as compared to SLC26A9; $\Delta\Delta G^{\text{N-terminal TM3}}_{\text{SLC26A9-prestin}} > 2.8$ kcal/mol , and was also seen in the site-resolved PFs that were obtained by deconvoluting the HDX-MS data using PyHDX (Figure 2.8).[31]

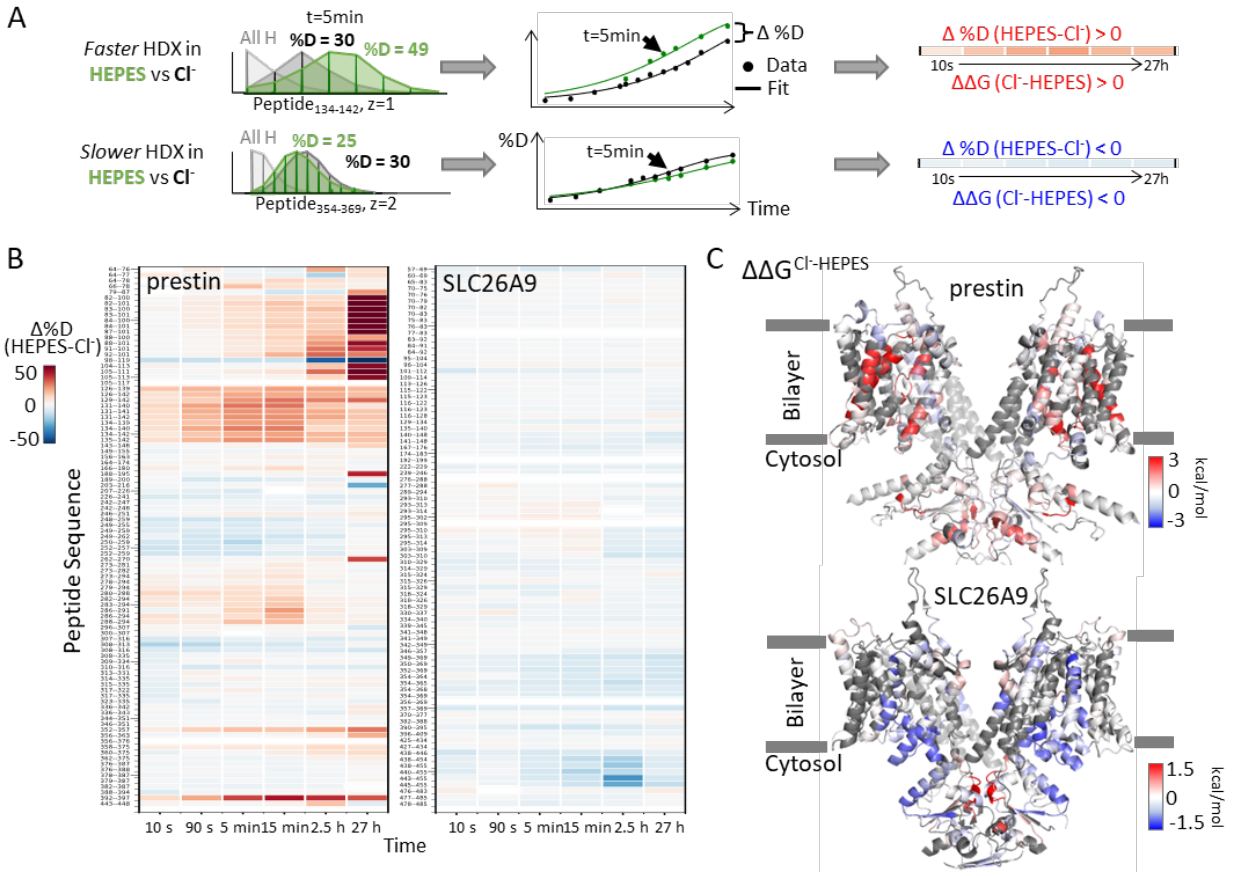

Figure 2.1: Distinct HDX response of prestin and SLC26A9 to Cl- binding.
(A) HDX data analysis to obtain **(B)** and **(C)**. One example peptide is shown in cases where HDX becomes faster or slower in HEPES (the putative apo state) compared to in Cl^-. Deuteration levels are obtained from the mass spectra. Here spectra for the undeuterated peptide (grey) and after 5 min HDX labeling in Cl^- (black) and HEPES (green) are shown as an example. The resulting deuterium uptake plots are used to generate the differential deuteration heatmaps in **(B)**. Changes

in free energy of unfolding (ΔΔG) in **(C)** are calculated after fitting the data with a stretched exponential (**Materials and Methods**).[29] **(B)** Heatmaps showing the difference in deuteration levels at each labeling time for all TMD peptides of prestin and SLC26A9 measured in HEPES compared to Cl^-. Peptide sequences are displayed on the y-scale and legible through the high resolution image. **(C)** The ΔΔGs in HEPES compared to Cl^- for full-length prestin and SLC26A9 mapped onto the structure (PDB 7S8X and 6RTC). Red and blue indicate increased and decreased stability upon Cl^- binding, respectively. Following regions of the left subunits are shown as low transparency to highlight the binding site – prestin: TM5 and TM12-14; SLC26A9: TM5 and TM13-14. Regions with no fitting results are in grey.

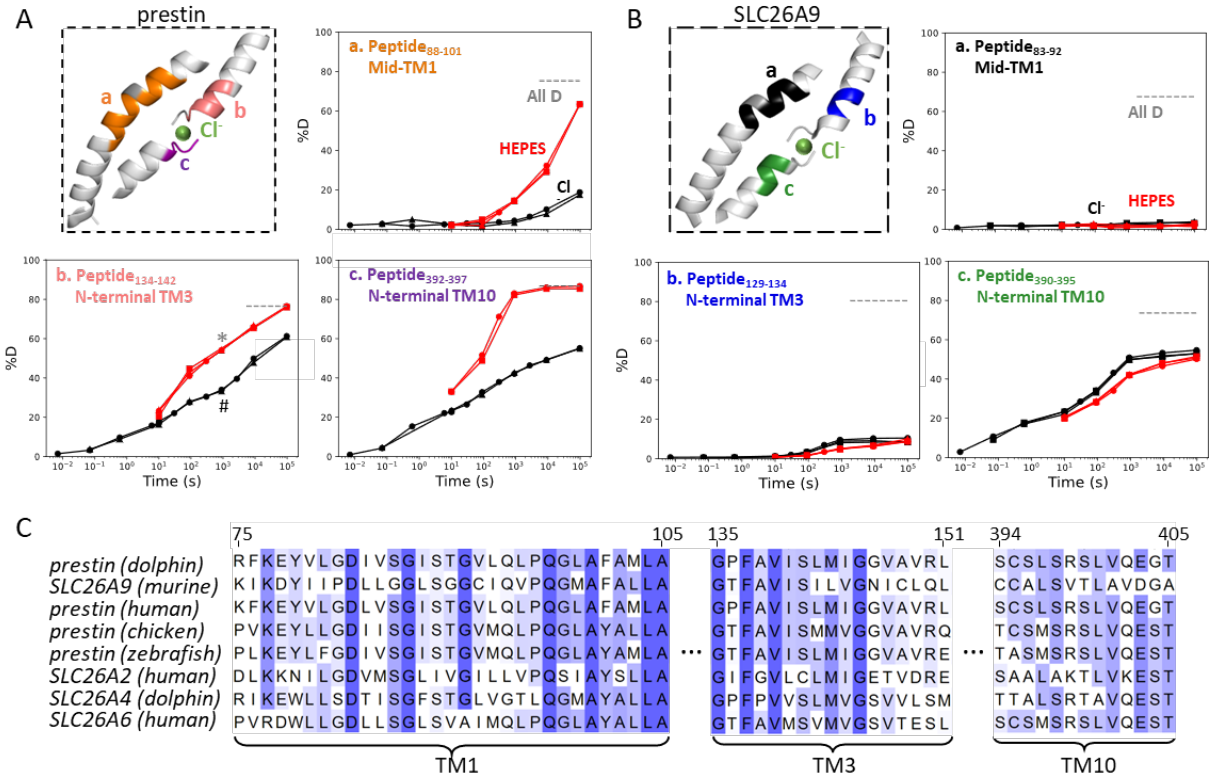

Figure 2.2: The anion-binding pockets for prestin and SLC26A9 exhibit distinct stability changes upon Cl- binding, albeit highly conserved.

(A-B) Cl^- binding stabilizes prestin's anion-binding pocket **(A)** but mildly affects SLC26A9's **(B)**. The structure shows the anion-binding pocket (TM1, TM3, and TM10) with the putative position of the bound Cl^-. Colored regions correspond to peptides whose deuterium uptake plots are shown when the protein is in Cl^- (black) and in HEPES (red). Prolines are colored in grey. Grey dashed lines indicate deuteration levels in the full-D control. Data from two and three biological replicates are shown for prestin in Cl^- and HEPES, respectively. Data from three technical replicates are shown for SLC26A9. Replicates are shown as circles, triangles, and squares. Some replicates are superimposable and hence not observable. The symbols (* and #) in **(A.b)** denote data points used

in **Fig. 3B**. **(C)** Sequence alignment using Clustal Omega of prestin and close SLC26 transporters across species for the anion-binding pocket. Shades of blue indicate degree of conservation.

Compared to the 20~350-fold HDX acceleration observed at prestin's binding site upon Cl^- removal, HDX of SLC26A9's binding pocket was only affected mildly (Figure 2.2 B). These included a slight slowing in HDX for the N-termini of TM3 ($Region_{131-134}$: $Peptide_{129-134}$) and TM10 ($Region_{392-395}$: $Peptide_{390-395}$) (Figure 2.2 B). The TM1 ($Region_{72-92}$: $Peptide_{83-92}$ + 10 other peptides) continued to remain undeuterated even after 27 h (Figure 2.2 B & Figure 2.16 S10.4-10.14), emphasizing the intrinsic high stability of SLC26A9's anion-binding pocket.

Although the anion-binding pocket is highly conserved and structurally similar across members of the SLC26 family and SLC26A5 families (Figure 2.2 C), mammalian prestin is the only member capable of displaying eletromotility.[32] Hence, the distinct stability responses we observe for dolphin prestin and mouse SLC26A9 point to a prestin's unique adaptation as a motor protein.

In addition to the binding pocket, we observed stability changes in various regions of the TMDs for prestin and SLC26A9 that may explain their distinct functions. For prestin, anion binding resulted in stabilization for the intracellular cavity but destabilization for regions facing the extracellular milieu (Figure 2.1 C & Figure 2.7 A). The stabilizing effects for the cytosol-facing regions were manifested by HDX acceleration upon Cl^- removal at the linker between TM2 and TM3, and the intracellular portions of TM7, TM8, & TM9 ($Region_{128-135}$, $Region_{284-294}$, & $Region_{354-375}$) (Figure 2.15 S9.22-9.27, S9.58-9.64, S9.82-9.87). In contrast, HDX slowed for the regions facing the extracellular environment, namely the extracellular ends of TM5b, TM6, and TM7 ($Region_{250-262}$ & $Region_{309-316}$) (Figure 2.15 S9.45-9.51, S9.66-9.68, S9.71). However, for SLC26A9, anion binding destabilized the cytosol-facing regions, as HDX slowed by ~5-fold upon Cl^- removal for the intracellular ends of TM8, TM9, and TM12 ($Region_{351-369}$ & $Region_{440-455}$) (Figure 2.1 C, Figure 2.7 B, & Figure 2.16 S10.62-10.63, S10.77-10.82). The distinct thermodynamic consequences of anion binding for prestin and SLC26A9 point to a distinct molecular basis underlying their different functions as a motor and a transporter, respectively.

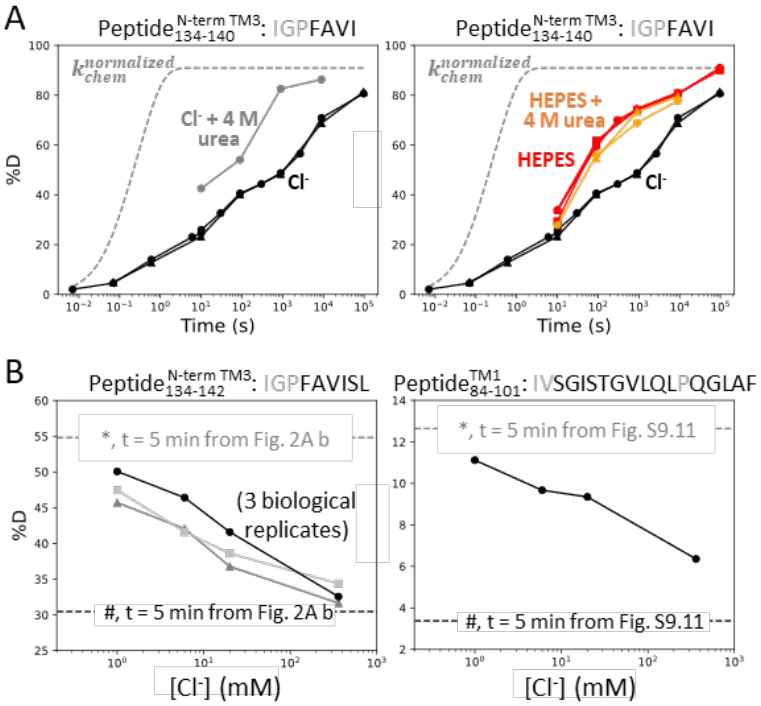

Figure 2.3: Anion binding folds and stabilizes prestin's binding site.

(A) Deuterium uptake plots for the N-terminus of TM3 (Peptide$_{134\text{-}140}$) measured in the absence and presence of 4 M urea, in a background of (**Left**) Cl^- and (**Right**) HEPES. Replicates (circles, triangles, and squares): 2 in Cl^-, 3 in HEPES, 2 in HEPES with urea, biological. Grey dashed curves represent deuterium uptake with k_{chem}, normalized with the back-exchange level. **(B)** Deuteration levels for (**Left**) the N-terminus of TM3 (Peptide$_{134\text{-}142}$) in three biological replicates and for (**Right**) TM1 (Peptide$_{84\text{-}101}$) after 5 min labeling upon titrating Cl^- to apo state of prestin. Dashed lines indicate deuteration levels at t = 5 min (* and # for apo and Cl^--bound states, respectively) taken from **Fig. 2A.b** and **Fig. S9.11**. Residues in grey denoted in the peptide sequence do not contribute to the deuterium uptake curve.

2.1.3.2 Anion binding drives the folding of prestin's binding site.

For prestin in HEPES, which adopted the putative apo state, the 20-fold HDX acceleration for the binding site (Figure 2.2 A) is consistent with a process of local destabilization, even unfolding, or increased solvent accessibility as the region becomes exposed to the intracellular water cavity.[17] To investigate these possibilities, we measured prestin's HDX in response to a chaotrope, urea, which destabilizes proteins by interacting with backbone amides.[33] In a background of 360 mM

Cl^-, the addition of 4 M urea accelerated HDX for the N-terminus of TM3 ($Region_{137\text{-}140}$: $Peptide_{134\text{-}140}$) by 20-fold (Figure 2.3 A), suggesting that this region was destabilized and accessible to urea in its exchange-competent state. In apo prestin, however, the PF at the N-terminus of TM3 was unaffected by urea (after accounting for the known ~50% slowing of the k_{chem}) (Figure 2.3 A), arguing that this region was already unfolded prior to the addition of urea.[33,34]

We note that in apparent contradiction to our inference that the N-terminus of TM3 was unfolded in the apo state, its HDX was ~100-fold slower than k_{chem}. Such apparent PF for an unfolded region has been reported when it is located inside an outer membrane beta-barrel, rationalized by the region having a lower effective local concentration of the HDX catalyst, [OD^-], than in bulk solvent.[35,36] For prestin, we propose that detergent molecules in the micelle can restrict the access of OD^- to amide protons, leading to a local effective pD lower than the bulk solvent and hence producing the apparent PF for the unfolded N-terminus of TM3.

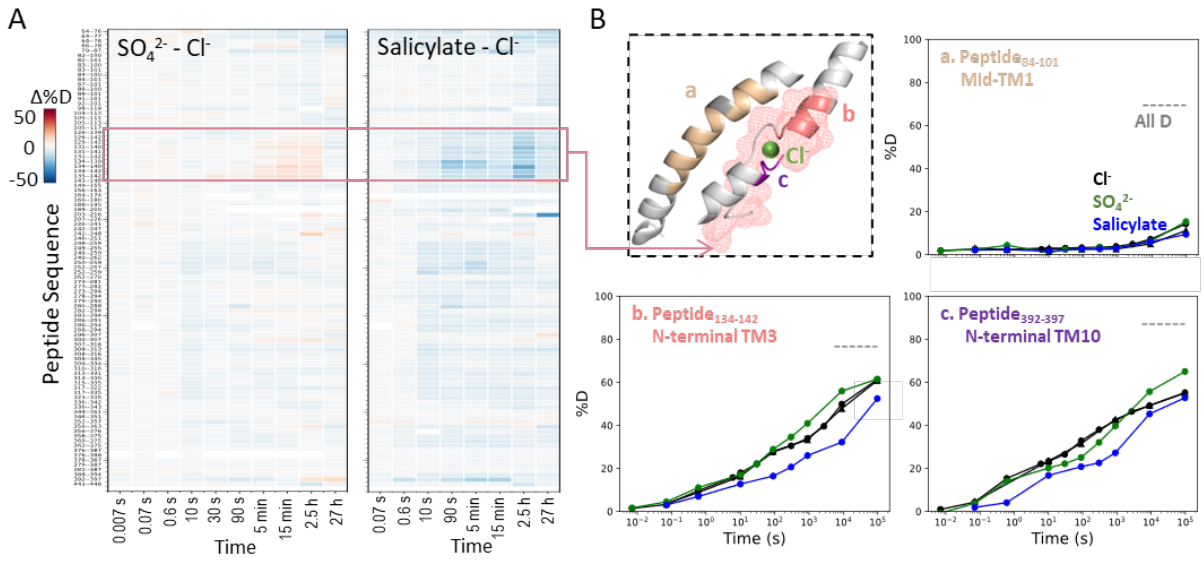

Figure 2.4: Prestin's dynamics are regulated by anions of varying identities.
(A) Heatmaps showing the difference in deuteration levels at each labeling time for all TMD peptides measured in SO_4^{2-} or salicylate compared to Cl^-. Peptide sequences are displayed on the y-scale and legible through the high resolution image. **(B)** The structure shows the anion-binding pocket with the putative position of the bound Cl^-. The pink mesh highlights the region with the greatest HDX response to binding to various anions. Colored regions correspond to peptides whose deuterium uptake plots are shown when the protein is in Cl^- (black, two biological replicates shown in circles and triangles), SO_4^{2-} (green), and salicylate (blue). Prolines are colored in grey. Grey dashed lines indicate deuteration levels in the full-D control.

The folding reversibility of the anion-binding site was evaluated by tracking the HDX for 5 min after titrating in Cl^- to apo prestin. Deuteration levels for the N-terminus of TM3 ($Region_{137-140}$) decreased with increasing Cl^- concentration (Figure 2.3 B), suggesting reversible folding upon Cl^- binding. Similar behavior was seen in the middle of TM1 ($Region_{86-101}$: $Peptide_{84-101}$) as Cl^- binding stabilized the binding pocket (Figure 2.3 B).

We also examined prestin's stability in its intermediate states, obtained by replacing Cl^- anions with SO_4^{2-} and salicylate.[17,18] When SO_4^{2-} is the major anion, prestin's HDX was nearly identical as in Cl^-, except for a slightly faster HDX at the anion-binding site ($Region_{128-142}$ and

Region$_{394–397}$) at labeling times longer than 10^3 s (Figure 2.4). This mild HDX response suggested a slightly destabilized binding site while the remaining regions retained normal dynamics as in Cl^-. In the presence of salicylate, HDX slowed across the TMD, with the greatest effect seen at the anion-binding site (10-fold; $\Delta\Delta G^{\text{binding site}}_{\text{salicylate-Cl-}}$ = 1.4 kcal/mol) (Figure 2.4), indicating that salicylate binding to prestin globally stabilized the TMD, primarily at the anion-binding site. These stability changes provide a thermodynamic context to the cryo-EM structures.[17]

2.1.3.3 Prestin in a lipid bilayer exhibits a highly dynamic TM6.

We chose to measure the HDX of prestin in GDN micelle to match the cryo-EM conditions.[17–19] Structures of GDN-solubilized prestin in Cl^- obtained by three research groups are indistinguishable (RMSD < 1 Å), demonstrating the reproducibility and robustness of the system.

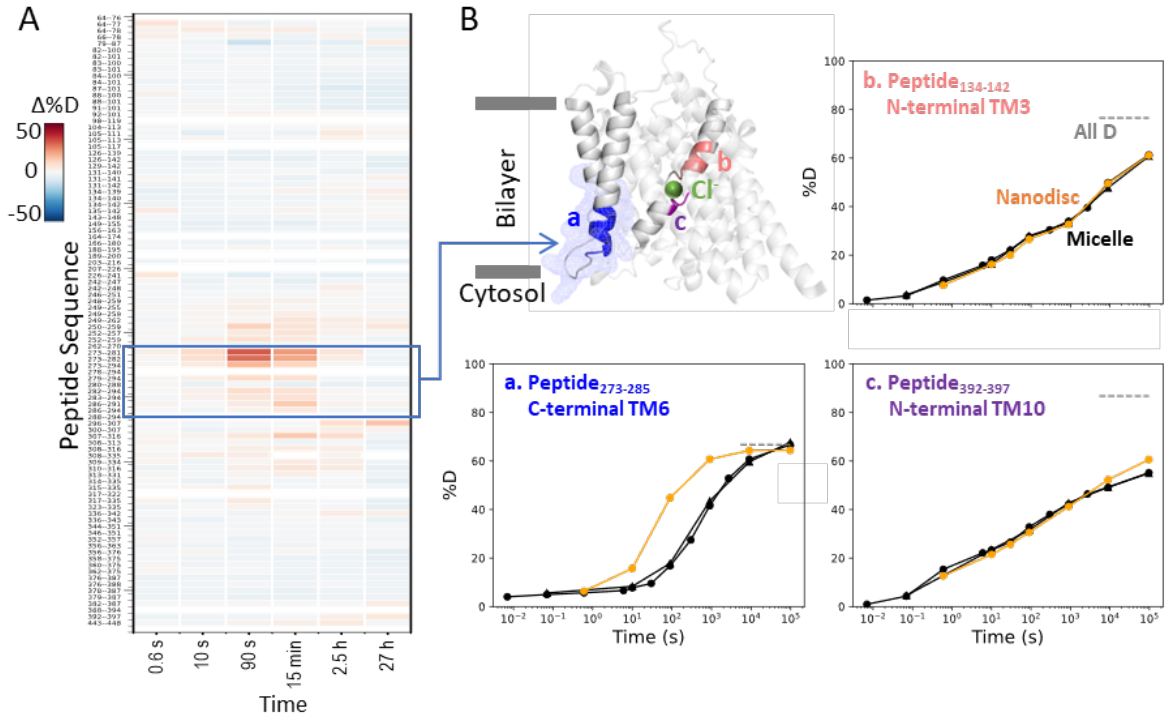

Figure 2.5: Prestin in nanodisc displays similar folding stability to prestin in micelle, except for a more dynamic TM6.
(A) Heatmaps showing the difference in deuteration levels at each labeling time for all available TMD peptides measured for prestin in nanodisc (porcine brain total lipid extract) compared to prestin in detergent micelle (GDN), both in Cl^-. Peptide sequences are displayed on the y-scale and legible through the high resolution image. **(B)** The structure shows the TMD for one subunit of prestin with the putative position of the bound Cl^-. The blue mesh highlights the region where the greatest HDX difference was seen for prestin in nanodisc compared to micelle. Colored regions correspond to peptides whose deuterium uptake plots are shown when the protein is in micelle (black, biological duplicates shown in circles and triangles) and in nanodisc (orange). Grey dashed lines indicate deuteration levels in the full-D control.

To evaluate the dynamics in a more native membrane environment, we measured HDX of prestin reconstituted in nanodisc (porcine brain total lipid extract). Except for TM6, HDX for prestin in nanodisc highly resembled that in micelles including the anion-binding pocket (Figure 2.5). Such high agreement between the folding stability in these two membrane mimetics suggest that our findings on prestin's anion-binding site and its folding equilibrium are pertinent to prestin

residing in a lipid bilayer. This is not surprising because structures for human prestin in GDN and nanodisc are shown to be nearly identical (Cα RMSD = 0.2 Å).[18]

Interestingly, nanodisc-embedded prestin displayed a less stable TM6 for the intracellular portion than prestin in micelles, manifested by the 10-fold HDX increase ($Region_{275-282}$: $Peptide_{273-282}$ + 2 peptides) (Figure 2.5 & Figure 2.15 S9.53-9.55). TM6 defines the interface between prestin and the lipid bilayer, and has been proposed to mediate area expansion through helical bending.[17] The exact role of TM6 in regulating prestin's conformational cycle is currently under investigation.

2.1.3.4 Incremental unfolding of prestin's binding site versus cooperative unfolding of the lipid-facing helices.

Our broad HDX time range and dense sampling allowed us to observe effects at the residue level. In particular, the binding site of prestin ($Region_{128-140}$ and $Region_{394–397}$) exhibited a broad deuterium uptake curve in Cl^-, indicative of helix fraying where exchange of deuterium occurs from multiple states that differ by one hydrogen bond (Figure 2.6 A). Such HDX pattern is consistent with the associated residues undergoing sequential unfolding with distinct PFs (i.e., stability). Site-resolved PFs obtained using PyHDX[31] support that the stability increased residue-by-residue for TM3 for amide protons located further away from the substrate (Figure 2.9 A). This gradual increase in residue stability along the helices is indicative of helix fraying starting from prestin's binding site.

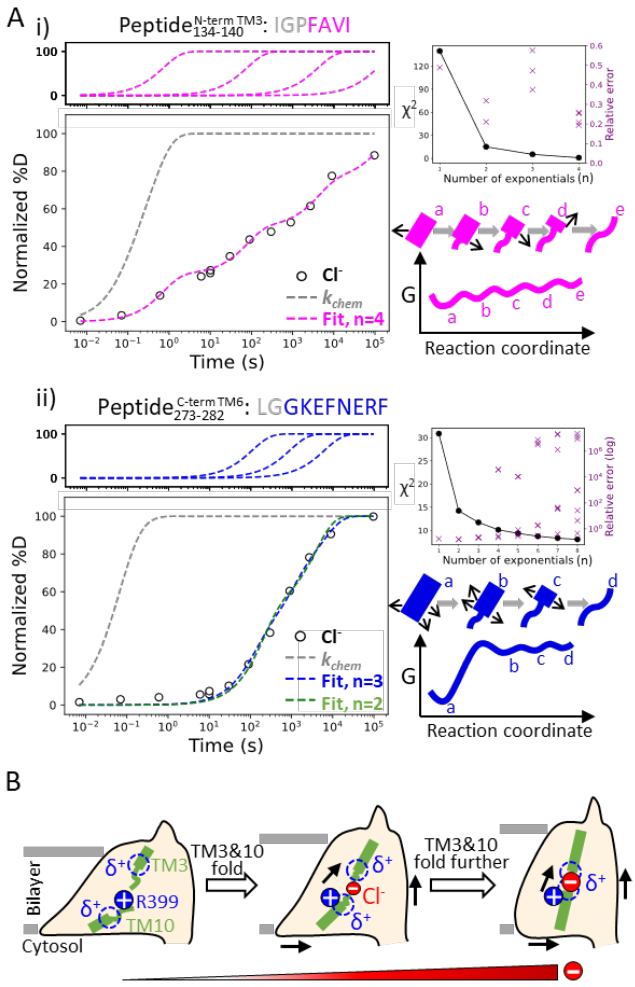

Figure 2.6: Helix folding cooperativity and the proposed mechanism for prestin's electromotility. **(A) Left:** Deuterium buildup curves for **(i)** the N-terminal TM3 ($Peptide_{134-140}$) and **(ii)** the intracellular portion of TM6 ($Peptide_{273-282}$) in Cl^- depicting helix fraying and mild cooperativity, respectively. Circles: experimental deuteration levels, normalized with in- and back-exchange levels. Grey dashed curves: hypothetical intrinsic uptake curves (PF = 1). On the top shows individual exponentials whose sum is fitted to the experimental values and plotted on the main buildup curves. Residues in grey denoted in the peptide sequence do not contribute to the deuterium uptake curve. **Upper right:** χ^2 and the relative error as the number of fit exponentials increases, used to assess the quality of fit. **Lower right:** Models and free energy surface of unfolding illustrating the difference between **(i)** fraying and **(ii)** mild cooperativity. **(B)** Mechanism for prestin's conformational transition from the expanded to the contracted state regulated by the anion concentration. Green rectangles and curved lines: folded and unfolded fractions, respectively, of TM3 and TM10. Blue filled circle: R399. Blue dashed circle: partial positive charges from TM3 and TM10 helical dipoles. Red filled circle: anions, with the size of the circle depicting anion concentrations. Black arrows: prestin's conformational change.

In contrast, we observed much more cooperative unfolding in prestin's lipid-facing helices, with exchange occurring from one or a few high energy states where a set of hydrogen bonds are broken concertedly. Cooperatively exchanging residues have similar PFs and a characteristic sigmoidal deuterium uptake curve for the associated peptide, as seen in prestin's intracellular portion of TM6 ($Region_{275\text{-}282}$: $Peptide_{273\text{-}282}$ + 4 peptides) (Figure 2.6 A & Figure 2.15 S9.53-9.57).

To characterize the degree of cooperativity for the HDX at the N-terminus of TM3 ($Peptide_{134\text{-}140}$) and the intracellular portion of TM6 ($Peptide_{273\text{-}282}$), we fit the deuterium uptake curves as a sum of exponentials[29], $D(t) = \sum_{i=1}^{n}(1 - e^{-k_i t})$, where k_i is the exchange rate and n is the number of exponentials, ranging from one to the number of exchange-competent residues. The value of n was determined by the quality of the fit, evaluated by χ^2 and having a relative error smaller than one (i.e., standard deviation for k_i less than k_i itself). HDX data for the N-terminus of prestin's TM3 ($Peptide_{134\text{-}140}$) was fit with four well-separated exponentials with rates spanning five log units for the four residues (Figure 2.6 A). The need to individually fit each site indicates a lack of cooperativity and helix fraying. In contrast, the peptide representing the intracellular portion of TM6 ($Peptide_{273\text{-}282}$) has eight residues yet it could be fitted with only three rates spanning less than two log units (Figure 2.6 A). This rather concerted deuterium uptake was independent of the anion substrate identity and also observed for TM1, TM5b, the intracellular portion of TM7, and the N-terminus of TM8 (Figure 2.15 S9.6-9.16, S9.42-9.43, S9.45-9.51, S9.58-9.63, S9.78-9.79).

We define a parameter $\sigma_{\Delta G}$ to quantify the degree of folding cooperativity. The value of $\sigma_{\Delta G}$ is calculated as the standard deviation for the free energies of unfolding (ΔGs) for exchange-competent residues comprising the peptide. When a region folds 100% cooperatively, $\sigma_{\Delta G}$ is zero

as all residues have the same ΔG. As the diversity increases (lower cooperativity), the $\sigma_{\Delta G}$ value becomes larger. The accuracy of the ΔG determination at residue level can be increased by comparing uptake curves for overlapping peptides and/or deconvoluting isotope envelopes.[29] Here we assigned exchange rates (k_i), obtained from the fitting method mentioned above, to residues based on the directionality of helix fraying, with residues closer to the end of a helix having faster rates. When there is ambiguity on which rate to assign to a given residue, the geometric mean of the rates was used (**Materials and Methods**). We found that prestin's intracellular portion of TM6 ($Peptide_{273-282}$) has $\sigma_{\Delta G}$ = 1.1, indicating mild cooperativity, whereas the non-cooperative N-terminal TM3 ($Peptide_{134-140}$) has a $\sigma_{\Delta G}$ = 2.9. This significant decrease in folding cooperativity for helices directly involved in the Cl^- binding site likely has functional consequences related to prestin's electromotility, as discussed below.

2.1.4 Discussion

Using HDX-MS, we provide novel information on the structural dynamics of prestin in its apo state, for which there isn't an associated cryo-EM structure. We demonstrate that prestin displays very similar dynamics in nanodisc as in micelles, except for a destabilized lipid-facing helix TM6 that is critical for mechanical expansion. We have explored the energetic and conformational differences between prestin, a voltage-dependent motor, and its mammlian relative SLC26A9, a representative member of the SLC26 family of anion transporters for which a cryo-EM structure is available. Our data point to major differences in the energetics at the anion-binding site of prestin and SLC26A9 despite their structural similarities. This comparison addresses underlying mechanistic questions related to the unique properties of prestin, the origin of its voltage

dependence, and the potential mechanisms that couple charge movements to electromotility.

We showed that prestin displays an unstable binding site, regardless of being in nanodisc or micelles (Figure 2.5). Upon Cl^- unbinding, the binding site unfolds by one helical turn at the electrostatic gap formed by the abutting (antiparallel) short helices TM3 and TM10 (Figure 2.2 A & Figure 2.3). We measured an increase in local $\Delta\Delta G = 1.8\sim3.5$ kcal/mol upon anion binding. This energy difference is within the range of the $\Delta\Delta G = 2.4$ kcal/mol estimated from having a 60-fold excess of Cl^- above the EC_{50} (6 mM).[23] Similar folding events upon anion binding are absent in SLC26A9 (Figure 2.2 B), pointing to a key role of the bound anion as a structural element in prestin, stabilizing the natural repulsion between TM3-TM10 positive helical macrodipoles. This phenomenon rationalizes the conundrum that prestin's voltage dependence requires the proximity of a bound anion to R399.

We find that anion binding to prestin mainly stabilizes the interface between the scaffold and the elevator domains (Figure 2.1 C & Figure 2.7 A). This phenomenon is consistent with an elevator-like mechanism during prestin's conformational transition from the expanded to the contracted state.[17] Anion binding stabilizes prestin's intracellular cavity and slightly destabilizes regions facing the extracellular matrix. This effect can result from changes in solvent exposure, as the intracellular water cavity may shrink as prestin contracts. For SLC26A9, the destabilization upon anion binding at the intracellular cavity likely results from a shift from the outward-facing state to the inward-facing state (Figure 2.1 C & Figure 2.7 B), supporting the alternate-access mechanism for this fast transporter.[21,22] Similar HDX changes, i.e., increased HDX on the intracellular side while decreased HDX on the extracellular side, have been observed in other transporters during their transition from outward-facing to inward-facing states.[37,38] Prestin's

distinct HDX response compared to a canonical transporter is consistent with it being an incomplete anion transporter.[23,39]

The HDX data for prestin in Cl^-, SO_4^{2-}, and salicylate support an allosteric role for the anion binding at the TM3-TM10 electrostatic gap (Figure 2.4).[24–26] SO_4^{2-} binding leads to shifts in the NLC towards positive potentials, thus stabilizing multiple conformations that are on average more expanded than prestin in Cl^-.[17,25,40] Since the binding of SO_4^{2-} to prestin is weaker than that of Cl^-,[18] the slight increase in HDX at the binding site likely reflects more prestin molecules adopting the apo state. Salicylate binding inhibits prestin's NLC and yet the molecular basis of such inhibition remains obscure.[17,28] Bavi *et al*[17] showed that binding of salicylate occludes prestin's binding pocket from solvent and inhibits the movement of TM3 and TM10. This is fully consistent with the 10-fold HDX slowing found for the N-termini of TM3 and TM10 upon salicylate binding as compared to the rest of the protein. Our HDX data, together with results from Bavi *et al.* suggest that salicylate likely inhibits prestin's NLC by restricting the dynamics of the anion-binding site.[17]

We identified helix fraying at the anion-binding site of prestin based on its broad deuterium uptake curve in the presence of Cl^-, consistent with a multi-state landscape (Figure 2.6 A). This fraying suggests that an increase in the anion concentration would promote helical propensity at TM3 and TM10, and is inconsistent with a cooperative (two-state) model involving an equilibrium between an apo state and a single bound state (Figure 2.6 A). Therefore, we suggest that a two-state model of prestin's conformational changes with a high energy barrier would be insufficient to explain its fast kinetics, whereas charge movement is facilitated by crossing multiple shallow

barriers.[25,41]

We propose that having a Cl^- binding site that frays can promote prestin's fast motor response which is thought to have evolved independently of its voltage sensing ability.[42,43] While the stability for TM10 is similar for prestin and SLC26A9, the latter protein exhibits a more stable, non-fraying TM3 (Figure 2.2). Notably, the normally highly conserved Pro136 in mammalian prestin is replaced with a Threonine in SLC26A9 and other vertebrates that express non-electromotile prestin (Figure 2.10 A). This Pro136Thr substitution, based on our *Upside* MD simulations, results in a hyper-stabilized TM3 that would otherwise have similar folding stability as TM10 (Figure 2.10 B). A Pro136Thr mutation in rat prestin also leads to a shift of NLC towards depolarized potentials.[30] These thermodynamic and functional consequences of having a destabilized TM3 with Pro136, which now has similar stability as TM10, lead us to hypothesize that prestin's fast mechanical activity may be promoted by having simultaneous fraying of the TM3 and TM10 helices.

Helices that exhibit cooperative unfolding all appear to be lipid-facing helices, including TM6-TM7, TM1, TM5b, and TM8. The region with the most pronounced cooperativity, the intracellular portion of TM6, has a series of glycines including the consecutive G274-G275 pair that underlies the "electromotility elbow", a helical bending contributing to the largest cross-sectional area (expanded conformation) and the thin notch in the micelle.[17] Importantly, HDX for prestin in nanodisc reveals a significant stability decrease at TM6 while the remaining regions retained similar dynamics as in micelles. This high sensitivity of TM6 stability to membrane environment, together with the structural consequences of cooperativity, speak to the its significance in prestin's area expansion. We propose that cooperativity allows for long-range

allostery[44] so that the lipid-facing helices, particularly TM6, can adopt large-scale structural rearrangements as induced by voltage sensor movements, thereby achieving rapid electromechanical conversions of prestin. The exact mechanism through which cooperativity contributes to prestin's electromotility remains a key question.

Based on the structural and allosteric role of Cl^- binding at the TM3-TM10 electrostatic gap, we propose a model in which prestin's conformational changes and electromotility are regulated by the folding equilibrium of the anion-binding site (Figure 2.6 B). In our model, anion binding participates in a local electrostatic balance that includes the positively charged R399 and the positive TM3-TM10 helical macrodipoles. In the apo state, the anion-binding site unfolds due to the electrostatic repulsion between these positively charged groups. Being a buried charge, R399 may exit from the electric field concentrated in the lower dielectric environment of the protein, and move into the solvent region as it lacks a neutralizing anion. This event is coupled to the allosteric expansion of prestin's membrane footprint.[17] Anion binding partially neutralizes the positive electric field at the binding site, an event that is coupled to the residue-by-residue folding for the N-termini of TM3 and TM10 as well as the shortening of the electrostatic gap. This folding event results in a more focused electric field and consequent contraction of prestin's intermembrane cross-sectional area. At physiologically-relevant low Cl^- concentration (1.5-4 mM),[45] prestin's binding site is likely to be only partially folded. Complete folding may be achieved by membrane potential acting on the TM3-TM10 helical dipoles, which leads to the movement of the voltage sensor across the electric field and the rapid areal expansion for the TMDs (i.e., electromotility).

2.1.4.1 Structure of prestin in HEPES and low Cl^- levels

We associate the HEPES solvent condition to an apo state as the HEPES anion is too big to fit into the chloride site and prestin has a right-shifted NLC.[25] To investigate further whether HEPES anion binds, we determined the structure of prestin in the HEPES-based buffer using cryo-EM. Our initial attempt to solve the structure in the complete absence of Cl^- was unsuccessful due to sample aggregation under cryogenic conditions. Aggregated particles were greatly reduced in the presence of 1 mM Cl^-, and we were able to solve the structure of GDN-solubilized prestin in 1 mM Cl^-, containing 190 mM HEPES, at a nominal resolution of 3.4 Å (**Supporting Information Text 3,** Figure 2.17 & Figure 2.18). Surprisingly, under these conditions prestin adopted a "compact" conformation, virtually identical to the previously reported Cl^--bound "Up" state,[17] displaying a clear density at the anion binding site (Figure 2.17 C). This density is incompatible with the placing of a HEPES molecule, and we reason it to be a small population of Cl^--bound prestin resulting from a weak Cl^- affinity (e.g., EC_{50}=6 mM[23] implies 17% bound). This result is consistent with the fundamental role of bound anions in the conformational stability of prestin and supports a new role for the folding equilibrium of the anion-binding site in the mechanism of voltage sensing. Ultimately, however, understanding the underlying mechanism for prestin's electromotility necessitates consideration of physiological elements such as membrane potential, kHz frequency,

and protein-lipid interactions.

2.1.5 Conclusions

We applied HDX-MS to the study of prestin's electromotility and identified folding events that are likely critical for function but had escaped detection by cryo-EM. The folding equilibrium of the Cl^- binding site and its dependence on Cl^- concentration appears to rationalize the conundrum of how an anion that binds in proximity to a positive charge (R399), can enable the NLC of prestin. We directly compared the dynamics of prestin in nanodisc to in micelles and identified TM6 as a potential mechano-sensing helix. We observed fraying of the helices forming the anion-binding site, which contrasts with cooperative unfolding of the lipid-facing helices. We believe that the non-cooperative fraying of the helices involved in voltage sensing may allow for fast charge movements within the electric field. This heightened sensitivity of the voltage sensor then induces large-scale motions of the lipid-facing helices, enabled by their cooperativity (or allostery), thereby altering the cross-sectional area of prestin. These principles warrant further investigation.

2.1.6 Materials and Methods

Sample preparation for prestin and SLC26A9. Generation of the dolphin prestin and mouse SLC26A9 constructs, protein overexpression, and purification were conducted using the same protocol as previously described. Following the cleavage of the GFP tag, the protein was purified by size-exclusion chromatography (SEC) on a Superose 6, 10/300 GE column (GE Healthcare), with the running buffer being either the "Cl^-/H_2O Buffer" or the "SO_4^{2-}/H_2O Buffer", including 1

μg/mL aprotinin and 1 μg/mL pepstatin.[17] The "Cl^-/H_2O Buffer" contained 360 mM NaCl, 20 mM Tris, 3 mM dithiothreitol, 1 mM EDTA, and 0.02% GDN at pH 7.5. The "SO_4^{2-}/H_2O Buffer" contained 140 mM Na_2SO_4, 5 mM $MgSO_4$, 20 mM Tris, 0.02% GDN, and 10-15 mM methanesulfonic acid to adjust the pH to 7.5. Peak fractions containing the sample were concentrated on a 100K MWCO centrifugal filter (Millipore) to 2-3 mg/mL, flash-frozen in liquid nitrogen, and kept at −80 °C until use.

For prestin reconstitution into nanodiscs, porcine brain lipid extract (Avanti) was first solubilized in "Cl^-/H2O Buffer" supplemented with 3% GDN to a 10 mg/mL concentration through successive rounds of sonication and freeze-thaw cycles. MSP1E3D1 was purified as previously described.[46,37] Reconstitution was performed using the "on-column" method[47] using a 1:5:600 (prestin:MSP:lipid) molar ratio, with the final buffer consisting of 20 mM Tris-HCl and 150 mM NaCl at pH 7.5.

For structure determination by cryo-EM, prestin purification was performed in buffers containing 360 mM NaCl as previously described,[17] except that the SEC running buffer now consisted of 190 mM HEPES, ~95 mM Tris-base (used to adjust the pH to 7.5), 1 mM NaCl, 3 mM DTT, 0.02% GDN, 1 μg/mL aprotinin, and 1 μg/mL pepstatin. Peak fractions containing the sample were concentrated to 3 mg/ml and used immediately for grid preparation.

Hydrogen-deuterium exchange. Table 1provides biochemical and statistical details for HDX in this study per recommendations by Masson *et al.*[48] HDX reactions, quench, and injection were all performed manually. Prior to HDX, proteins purified in Cl^- and SO_4^{2-} were buffer exchanged to the same H_2O buffer without protease inhibitor using 7K MWCO Zeba spin desalting columns

(Thermo 89882). For HDX conducted in HEPES, proteins purified in Cl^- were dialyzed against the "HEPES/H_2O Buffer" (150 mM HEPES, 0.02% GDN, pH adjusted to 7.5 by HEPES acid or base) using a 10K MWCO dialysis device (Thermo Slide-A-Lyzer MINI 69570) with three times of buffer exchange for near-complete Cl^- removal. HDX in a solution of 93% deuterium (D) content was initiated by diluting 2 μL of 25 μM prestin or SLC26A9 stock in an H_2O buffer into 28 μL of the corresponding buffer made with D_2O (99.9% D, Sigma-Aldrich 151882). HDX was conducted in one of the two conditions: 1) pD_{read} 7.1, 25 °C; 2) pD_{read} 6.1, 0 °C. The D_2O buffers contained the same compositions as the corresponding H_2O buffers, except that Tris was replaced with Phosphate for the "SO_4^{2-}/D_2O Buffer" for both HDX conditions, and the "Cl^-/D_2O Buffer" for HDX performed at pD_{read} 6.1, 0 °C. The pD_{read} was adjusted to 7.1 or 6.1 by DCl for the "Cl^-/D_2O Buffers" and by NaOD for other D_2O buffers. For HDX in the presence of salicylate, 50 mM salicylate acid was added to the "SO_4^{2-}/D_2O Buffer" and the pD_{read} was adjusted by NaOD. For HDX in the presence of urea, 4 M urea was added to the "Cl^-/D_2O Buffer" or the "HEPES/D_2O Buffer", with accurate urea concentration determined to be 4.16 M and 4.54 M, respectively, by refractive index using a refractometer (WAY Abbe).[49]

HDX was quenched at various times, ranging from 1 s to 27 h, by the addition of 30 μL of ice-chilled quench buffer containing 600 mM Glycine, 8 M urea, pH 2.5. For HDX in the presence of urea, urea concentration in the quench buffer was adjusted to reach a 4 M final concentration. For HDX on prestin in nanodisc, the quench buffer also included 3 μL of 0.8% GDN and 3 μL of 300 mg/ml aqueous suspension of ZrO2-coated silica (Sigma-Aldrich, reference no. 55261-U). The resulting mixture was incubated on ice for 1 min to remove lipids and solubilize prestin in GDN before being filtered through a cellulose acetate spin cup (Thermo Pierce, Waltham,

Massachusetts, reference no. 69702) by centrifugation for 30 s at 13,000 g, 2 °C. Quenched reactions were immediately injected into a valve system maintained at 5 °C (Trajan LEAP). Non-deuterated controls and MS/MS runs for peptide assignment were performed with the same protocol as above except D_2O buffers were replaced by H_2O buffers, followed by the immediate addition of the quench buffer and injection.

HDX reactions were performed in random order. No peptide carryover was observed as accessed by following sample runs with injections of quench buffer containing 4 M urea and 0.01% GDN. In-exchange controls accounting for forward deuteration towards 41.5% D in the quenched reaction were performed by mixing D_2O buffer and ice-chilled quench buffer prior to the addition of the protein. Maximally labeled controls ("All D") accounting for back-exchange were performed by a 48-h incubation with the "Cl^-/D_2O Buffer" at 37 °C, followed by a 30-min incubation with 8 M of deuterated urea at 25 °C.

Protease digestion and LC-MS. Upon injection, the protein was digested online by a pepsin/FPXIII (Sigma-Aldrich P6887/P2143) mixed protease column maintained at 20 °C. Protease columns were prepared in-house by coupling the protease to a resin (Thermo Scientific POROS 20 Al aldehyde activated resin 1602906) and hand-packing into a column (2 mm ID × 2 cm, IDEX C-130B). After digestion, peptides were desalted by flowing across a hand-packed trap column (Thermo Scientific POROS R2 reversed-phase resin 1112906, 1 mm ID × 2 cm, IDEX C-128) at 5 °C. The total time for digestion and desalting was 2.5 min at 100 μL/min of 0.1% formic acid at pH 2.5. Peptides were then separated on a C18 analytical column (TARGA, Higgins Analytical, TS-05M5-C183, 50 x 0.5 mm, 3 μm particle size) via a 14-min, 10–60% (vol/vol) acetonitrile (0.1%

formic acid) gradient applied by a Dionex UltiMate-3000 pump. Eluted peptides were analyzed by a Thermo Q Exactive mass spectrometer. MS data collection, peptide assignments by SearchGUI version 4.0.25, and HDX data processing by HDExaminer 3.1 (Sierra Analytics) were performed as previously described.[35,36]

HDX data presentation, quantification, and statistics. In our labeling convention, we name capitalized regions according to the third residue of each peptide since the first two residues have much faster k_{chem}[5,6] and hence, exhibit complete back-exchange. Labeling times for HDX performed in pD_{read} 6.1, 0 °C were corrected to those in pD_{read} 7.1, 25 °C by a factor of 140, determined by the ratio of the k_{chem} for full-length proteins in the two conditions – prestin: $\tau_{chem}^{\text{pDread 6.1,0 °C}}$ = 10 sec, $\tau_{chem}^{\text{pDread 7.1,25 °C}}$ = 74 msec; SLC26A9: $\tau_{chem}^{\text{pDread 6.1,0 °C}}$ = 9 sec, $\tau_{chem}^{\text{pDread 7.1,25 °C}}$ = 65 msec. Deuteration levels were adjusted with the 93% D content but not with back-exchange levels except for Figure 2.6 A. For HDX in the presence of urea (Figure 2.3 A), D contents of 76% and 74% were used to account for the volumes of 4.16 M and 4.54 M urea in the "Cl^-/D_2O Buffer" and the "HEPES/D_2O Buffer", respectively.

HDX rates, protection factors (PFs), and changes of free energy of unfolding (ΔΔG's) in the Results section were estimated by fitting uptake curves of each peptide, after correcting for back-exchange levels, with a stretched exponential as described by Hamuro 2021,[29] except for discussion relevant to Figure 2.6 A. Peptides with less than 10% D at the longest labeling time (~10^5 s) were not used for fitting. The residue-level ΔΔG values presented in the full-length proteins in Figure 2.1 C were estimated by averaging ΔΔG values for peptides containing the residue. We note that this stretched exponential method is only a rough approximation to extract

ΔΔG's and our major conclusions are not dependent on this fitting method.

For fitting HDX data and extracting rates relevant to Figure 2.6 A, HDX data were first normalized to in- and back-exchange levels. Given the helices are likely to exchange by fraying, the exchange rate for each residue was assigned based on their distance from the end of the helix. When a residue could not be assigned to a single rate, the geometric mean of the possible rates was used, e.g., the HDX data for the 8-residue $Peptide_{273\text{-}282}$ were well fit with 3 exponentials, and the three associated rates, k_1, k_2, & k_3, were assigned to the 8 residues according to k_1, k_1, $(k_1k_1k_2)^{1/3}$, k_2, k_2, $(k_2k_2k_3)^{1/3}$, k_3, & k_3. These rates were used to calculate folding stability according to $\Delta G = -\mathrm{RTln}(k_{chem}/k_i - 1)$.

A hybrid statistical analysis used to generate Figure 2.7 was performed as described by Hageman & Weis, 2019,[50] with significance limits defined at $\alpha = 0.05$.

MD simulations. Simulations were conducted in our Upside molecular dynamics package[51,52] using a membrane thickness of 38 Å. Missing residues for prestin (PDB 7S8X) were built using MODELLER[53] and the placement within the bilayers was accomplished using Positioning of Proteins in Membranes webserver.[54] Local restraints in the form of small springs between nearby residues were used to maintain the native structure of cytosolic domains, as well as to the TM13-TM14 helices. Also, the distance between the two TMDs was held fixed. We ran 28 temperature replicas between 318 and 360K.

Cryo-EM sample preparation and data collection. The cryo-EM data was collected from three separate samples and microscope sessions. For dataset 1, 3.5 μL of prestin sample was applied to Quantifoil 200-mesh 1.2/1.3 Cu grids (Quantifoil) that were plasma cleaned for 30s at 20W. For datasets 2 and 3, 3.5 μL of prestin sample was applied to UltrAuFoil 300-mesh 1.2/1.3 grids (Quantifoil UltrAuFoil) that were plasma cleaned for 40s at 20W. The remaining sample preparation and imaging conditions were kept constant for all three samples. Grids were blotted at 22 °C and 100% humidity with a blot time of 3.5 s and a blot force of 1, and flash-frozen into liquid ethane using a Vitrobot Mark IV (Thermo Fisher). Grids were imaged at The University of Chicago Advanced Electron Microscopy Facility on a 300 kV Titan Krios G3i electron microscope equipped with a Gatan K3 camera in CDS mode, a GIF energy filter (set to 20 eV) and with magnification set to 81,000x, corresponding to a physical pixel size of 1.068 Å. Movies were acquired at a dose of 1.2 $e^-/Å^2$ for 50 frames (corresponding to a total dose of 60 $e^-/Å^2$) and a defocus range of -0.7 to -2.1 μm. 2,153 movies were collected for dataset 1, 1,928 movies for dataset 2, and 6,665 movies for dataset 3.

Cryo-EM Image Processing. Cryo-EM data processing was performed using Relion-4.0[55] and cryoSPARC v4.1.[56] Movies from the different datasets were motion-corrected independently in Relion with a bin-1 pixel size of 1.068 Å. The motion-corrected micrographs were then combined and imported into cryoSPARC for Patch CTF Estimation. Unless otherwise mentioned, the following steps were performed in cryoSPARC. Particles were picked using template-based particle picking. The initial picks were curated using Inspect Picks and extracted at a box size of 256. Two rounds of 2D Classification were performed to filter out additional “junk” particles,

resulting in a set of 328,033 particles. Two consecutive rounds of ab initio reconstruction, followed by heterogeneous refinement with C1 symmetry were performed to obtain a stack of 170,313 particles. These particles were used as input for an initial round of non-uniform and local CTF refinement using C2 symmetry and exported to Relion for Bayesian Polishing. Additional 3D Classification was performed in Relion to remove additional "junk" particles, resulting in a set of 170,313 particles. However, no additional classes were found. The final set of polished particles was then imported back into cryoSPARC and subjected to a final round of non-uniform and CTF refinement, resulting in a map with a nominal resolution of 3.4 Å, according to the gold-standard 0.143 FSC criterion.[57] Local resolution was estimated using local resolution estimation in cryoSPARC.

Model building and refinement. A previous model of dolphin prestin (PDB 7S8X) was roughly fit into the density map and used as a template for model building. Initially, only a monomer was considered for model building, and the fitting was improved by running Phenix real space refinement[58] with secondary structure restraints, morphing, and simulated annealing enabled. Subsequently, the monomer model was iteratively refined by manual inspection in Coot[59] and real space refinement without morphing and simulated annealing in Phenix. After several rounds of refinement, the second monomer was added using the apply_ncs tool in Phenix with C2 symmetry, and the resulting dimer model was subjected to an additional round of manual inspection in Coot. A chloride ion was manually added into the density observed in the anion binding pocket in Coot. All figures related to the cryo-EM structure were prepared using UCSF ChimeraX.[60]

2.1.7 Acknowledgments

This work was supported by grants to T.R.S. from the NSF (MCB 2023077) and the NIH (GM55694, 1R35GM148233), and to E.P. from R01 DC019833. We would like to thank the Advanced Electron Microscopy Facility at The University of Chicago for providing cryo-EM training and help with data collection.

2.1.8 Data availability

The raw mass spectrometry proteomics data have been deposited to the ProteomeXchange Consortium via the PRIDE partner repository with the dataset identifier PXD046965. The atomic structure coordinates have been deposited at the RCSB PDB under accession number 8UC1; and the EM maps have been deposited in the Electron Microscopy Data Bank under accession number EMD-42112. All materials generated during the current study are available from the corresponding author under a materials transfer agreement with The University of Chicago.

2.1.9 Supporting information

2.1.9.1 Supporting Information Text 1: Heterogeneity and HDX kinetics.

HDX in our study occurred mostly via EX2 kinetics where the observed exchange rate (k_{ex}) reports on the equilibrium (i.e., stability) rather than the opening rates of the exchange-competent states. The identification of EX2 behavior is supported by 1) k_{ex} of prestin in the two HDX conditions differed by 140-fold, which can be attributed solely to the effect of pH and temperature on k_{chem}

for residues across the entire protein (Figure 2.13 A); 2) the continuous shifts in the single isotopic envelopes towards higher m/z with exchange time (Figure 2.13 B); 3) the envelopes had the binomial distribution expected when each site exchanges independently, supported by HDExaminer (v3.3) fits. The tracking of k_{ex} with k_{chem} also argues that prestin exhibits similar dynamics under the two HDX conditions, allowing us to combine the experiments after correcting for the difference in k_{chem}.

We observed bimodal isotopic envelopes for peptides in TM1 ($Region_{84-101}$: 9 peptides), with both envelopes increasing in mass over time, one exchanging slower than the other (Figure 2.14 A). Bimodality can result from HDX occurring via EX1 kinetics where every opening event results in exchange; this occurs when the rate of reforming the hydrogen bond, k_{close}, is much slower than k_{chem}. The signature of EX1 kinetics is a decrease in the amplitude of the lighter envelope and a commensurate increase in the heavier amplitude over time.[61] This EX1 behavior is observed in TM9 ($Region_{378-387}$) (Figure 2.14 B). Alternatively, bimodality can reflect the presence of two non- or slowly-interconverting, structurally distinct populations, each having its own exchange behavior. Peptides in TM1 retained a 1:3 ratio of relative intensity for the heavy-to-light envelopes regardless of biological replicates or anionic conditions, pointing to kinetically distinct populations. In addition, both populations in TM1 exchanged via EX2 kinetics (Figure 2.14 A). Therefore, conformational heterogeneity best explains the exchange behavior of TM1 with an interconversion time between the two populations being longer than our longest labeling time (27 h). We associate the slow population with the natively folded TM1, as observed in cryo-EM studies,[17] and focus on this population in the present study.

As just noted, the presenting data for TM1 point to conformational heterogeneity with two populations having distinct HDX behavior. We believe that the fast population has TM1 unfolded despite it having a PF of ~100. We attribute this residual protection to detergent molecules hindering solvent access to the backbone and hence slowing exchange. This is the same explanation we provided for the heightened protection observed for the N-terminal TM3 ($Region_{137\text{-}140}$) in apo prestin (Figure 2.3 A). Generally, intrinsic HDX rates for unfolded regions of a soluble protein (i.e., k_{chem}) may not always serve as an appropriate reference rate for membrane-associated regions in the presence of detergents or lipids.

2.1.9.2 Supporting Information Text 2: Combining HDX-MS and cryo-EM in structural biology.

HDX-MS can provide information on dynamics and thermodynamics that generally is unavailable with cryo-EM alone. Accordingly, the synergetic use of HDX-MS and cryo-EM can validate each other and provide new insights.[62] We obtained a peptide coverage of 83% and 81% for prestin and SLC26A9, respectively, with a total of 266 and 338 peptides, allowing us to interrogate the protein-wide dynamics (Figure 2.11 A & Table 1). The main difference for the two proteins' sequence coverage is that only prestin has coverage at TM6 while only SLC26A9 has coverage at TM12. The different cleavage preferences at these two helices likely result from different flexiblity and/or exposure, which can be related to the different functions of the two proteins.

In 360 mM Cl^-, the majority of the TMDs for prestin and SLC26A9 had similar stability, with peptide-level protection factors (PFs) ranging from 10^3 to 10^{6+}; ΔG = 4.2 to 8.4+ kcal/mol

(Figure 2.8 & Figure 2.11 B). Both proteins had highly stable regions with negligible exchange after 27 h, our longest labeling time. We obtained near-residue level resolution at regions unresolved in the cryo-EM structures, including the intervening sequence of the STAS domain (sulfate transporter and anti-sigma factor antagonist) and the C-termini.[17–19,21,22] Regions$_{583\text{-}613,\ 734\text{-}764}$ for prestin and Regions$_{570\text{-}653,\ 741\text{-}770}$ for SLC26A9 had a PF of unity under all conditions examined (Figure 2.12), indicating these regions are unfolded and independent of anion binding. This finding supports the proposal that the disordered regions of prestin may play a role in its interactions with other proteins for reasons of regulation rather than electromotility.[63,64]

HDX is a solution-based method that probes the hydrogen bond network, and hence, any discrepancies with cryo-EM structures could reflect structural perturbations resulting from the sub-millisecond freezing process.[65] According to differences in cryo-EM and HDX, 2-3 residues form additional hydrogen bonds at the termini of two helices upon freezing. These sites included residues 565-566 and 720-722 for prestin and residues 225-226 and 738-740 for SLC26A9. Helical propagation can occur within 10 nsec[66] while the cooling time for cryo-EM can be as slow as 200 μsec,[65] which provides ample time for helix extension as the helices equilibrate to the lower temperature.[67] Although we anticipate that such small-scale folding events are common during the freezing process, overall, the HDX data do not provide evidence for significant changes in hydrogen bonding patterns for either prestin or SLC26A9. We anticipate that both the barriers for larger-scale folding events and solvent viscosity increase significantly as the temperature drops, effectively trapping the protein in its pre-frozen conformation. Nevertheless, we note that motions that do not result in changes in the hydrogen bond network, such as rigid-body motions of helices, would not be identified by HDX.

2.1.9.3 Supporting Information Text 3: Structure of prestin in HEPES and low Cl^- levels.

Using single-particle cryo-EM, we set out to determine the structure of prestin in the HEPES-based buffer with the goal of visualizing a putative apo state. Prestin was initially screened in 190 mM HEPES in a nominal absence of Cl^-. This condition, however, led to widespread particle aggregation under cryogenic conditions. We reasoned that this aggregation may be linked to the already destabilized prestin without a bound Cl^-, as evidenced by HDX-MS data, as well as the low ionic strength of our buffer. Indeed, 1 mM Cl^- sharply reduced particle aggregates, allowing us to solve the structure of prestin solubilized in GDN at a nominal resolution of 3.4 Å from particles, which corresponds to about 10% of the total particles in the sample. Surprisingly, under these conditions prestin adopted a "compact" conformation, virtually identical to the previously reported Cl^--bound "Up" state (Figure 2.17). Moreover, the anion-binding site is structurally indistinguishable from previous Cl^--bound structures (Figure 2.17 B). Furthermore, when focusing on the anion-binding pocket in our cryo-EM map, we see clear evidence for an additional density, indicating that the pocket is occupied by a substrate (Figure 2.17 C). However, we were unable to model a HEPES anion into the binding pocket without substantial steric clashes. We therefore suggest that the resolved density represents instead a Cl^- anion, given that a small population of Cl^--bound prestin will be present from a weak Cl^- affinity (e.g., EC_{50}=6 mM[23] implies 17% bound). Although we cannot confirm this notion with absolute certainty, it is clear that our cryo-EM structure does not represent a true apo state of prestin and is consistent with the notion that unbound, apo prestin is conformationally unstable.

2.1.10 Supplementary figures

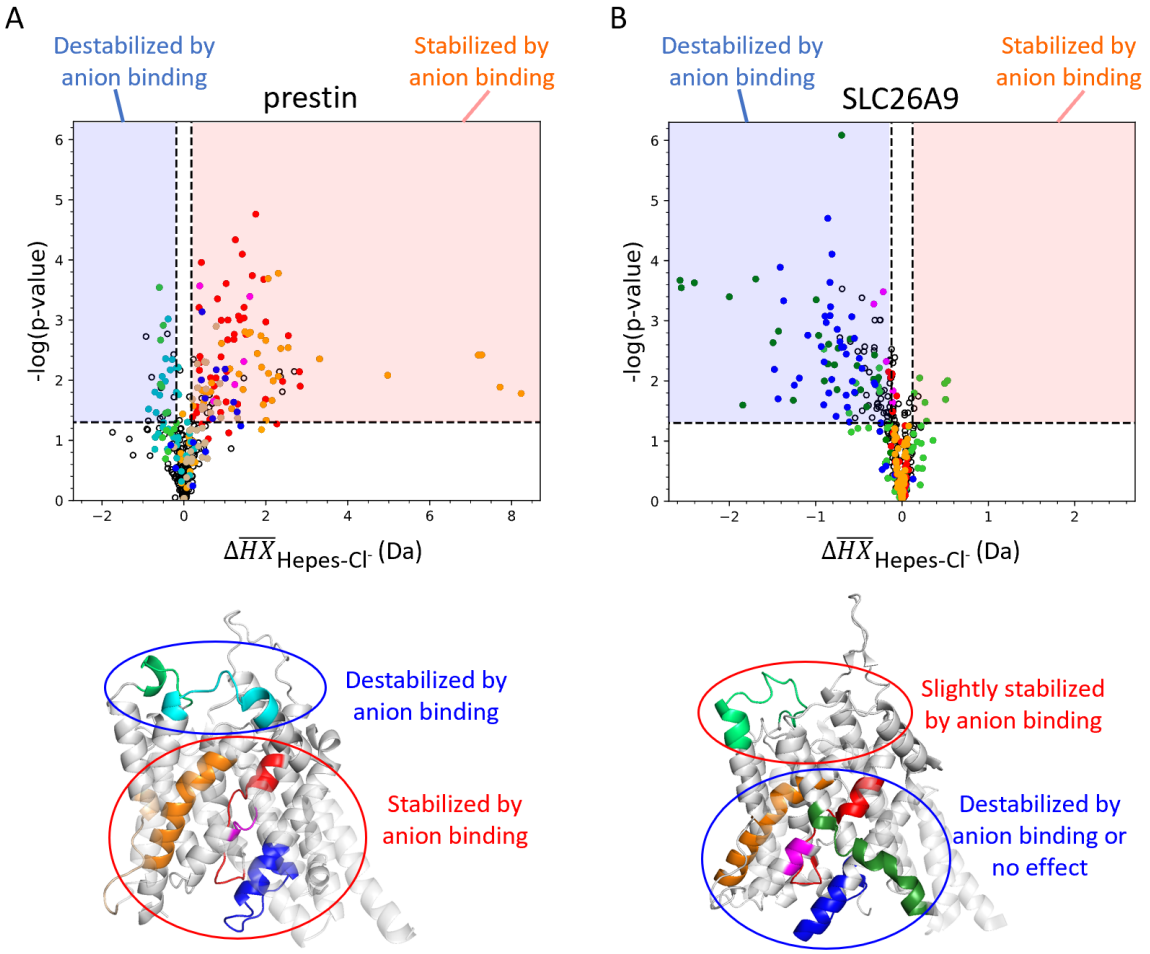

Figure 2.7: Volcano plot analysis of HDX for prestin (A) and SLC26A9 (B) in response to Cl- binding.
$\Delta\overline{HX}\Delta\overline{HX}$A hybrid statistical analysis is employed.[50] Each data point represents one time point of a peptide. The horizontal axis shows the difference between the observed mean peptide masses () for the protein in HEPES and in Cl^-. The vertical axis shows Welch's t-test p-values. The dashed horizontal lines denote p-value significance limits defined at $\alpha = 0.05$. The dashed vertical lines denote the significance threshold corresponding to $\alpha = 0.05$, calculated to be ±0.17 Da and ±0.11 Da for **(A)** prestin and **(B)** SLC26A9, respectively. Data points in the red and blue area (i.e., exceeding significance limits in both dimensions) represent peptides that show statistical significance and are stabilized and destabilized upon Cl^- binding, respectively. Colored data points correspond to colored regions in the corresponding TMD structure below.

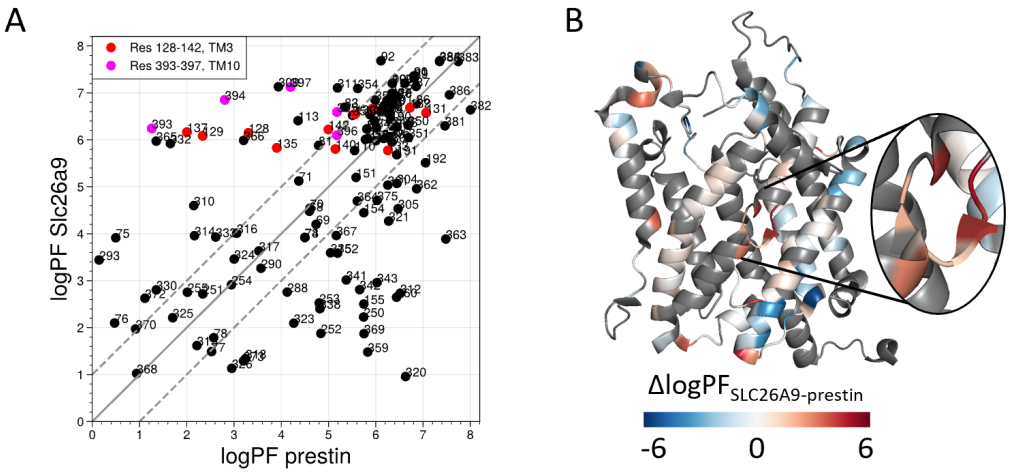

Figure 2.8: Site-resolved protection factors for prestin and SLC26A9 obtained using PyHDX. **(A)** Site-resolved protection factors in a log scale (logPF) for the TMDs of prestin and SLC26A9 with residue numbers denoted. **(B)** The difference in logPF (ΔlogPF) mapped onto the prestin structure. Grey represents regions with no fitting data available. TM5 and TM12-14 do not have fitting data and are not shown to highlight the anion-binding site. Fitting was done using PyHDX[31] on HDX-MS data measured for both proteins in Cl^-.

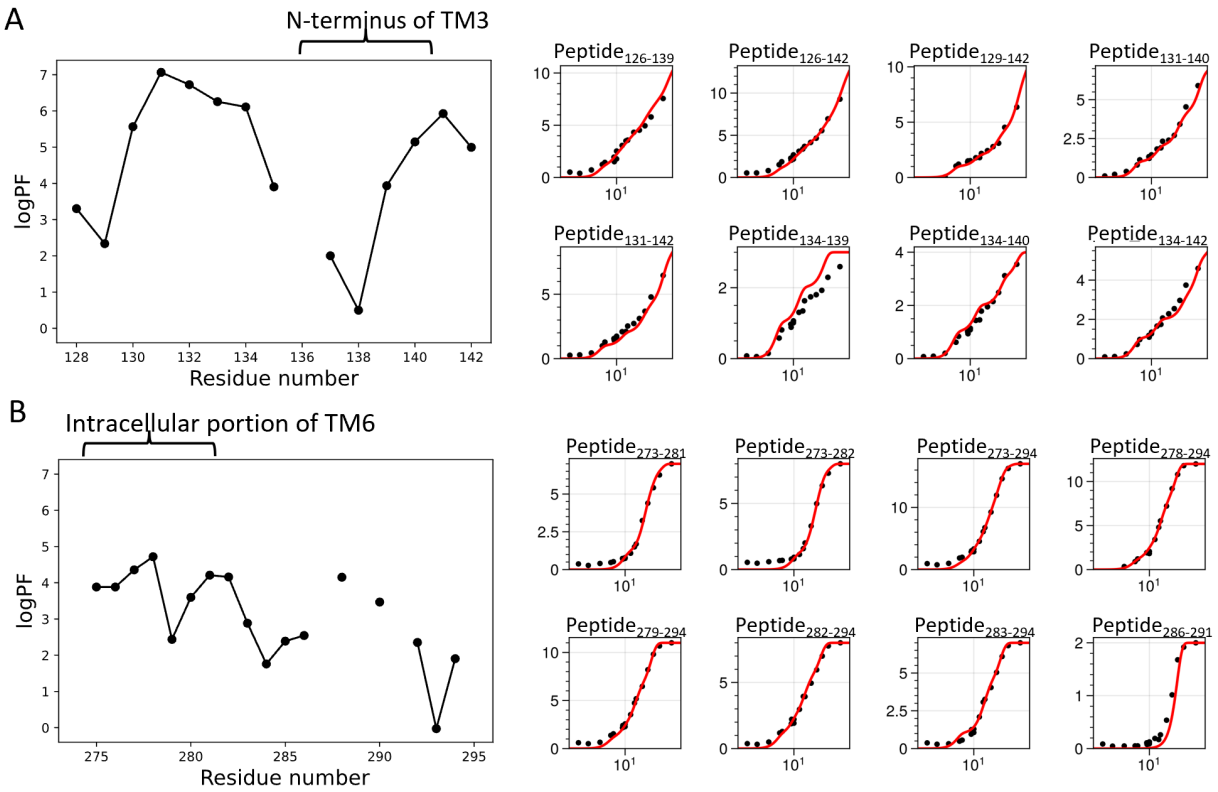

Figure 2.9: PyHDX fitting supports that prestin exhibits helix fraying at the N-terminus of TM3 and mild cooperativity at the intracellular portion of TM6.
Left: Site-resolved protection factor values in a log scale (logPF) obtained by deconvoluting HDX-MS data using PyHDX[31] for regions covering **(A)** the N-terminus of TM3 and **(B)** the intracellular portion of TM6. **Right:** PyHDX fittings for the corresponding peptides – black circles: experimental deuteration levels; red curves: fittings.

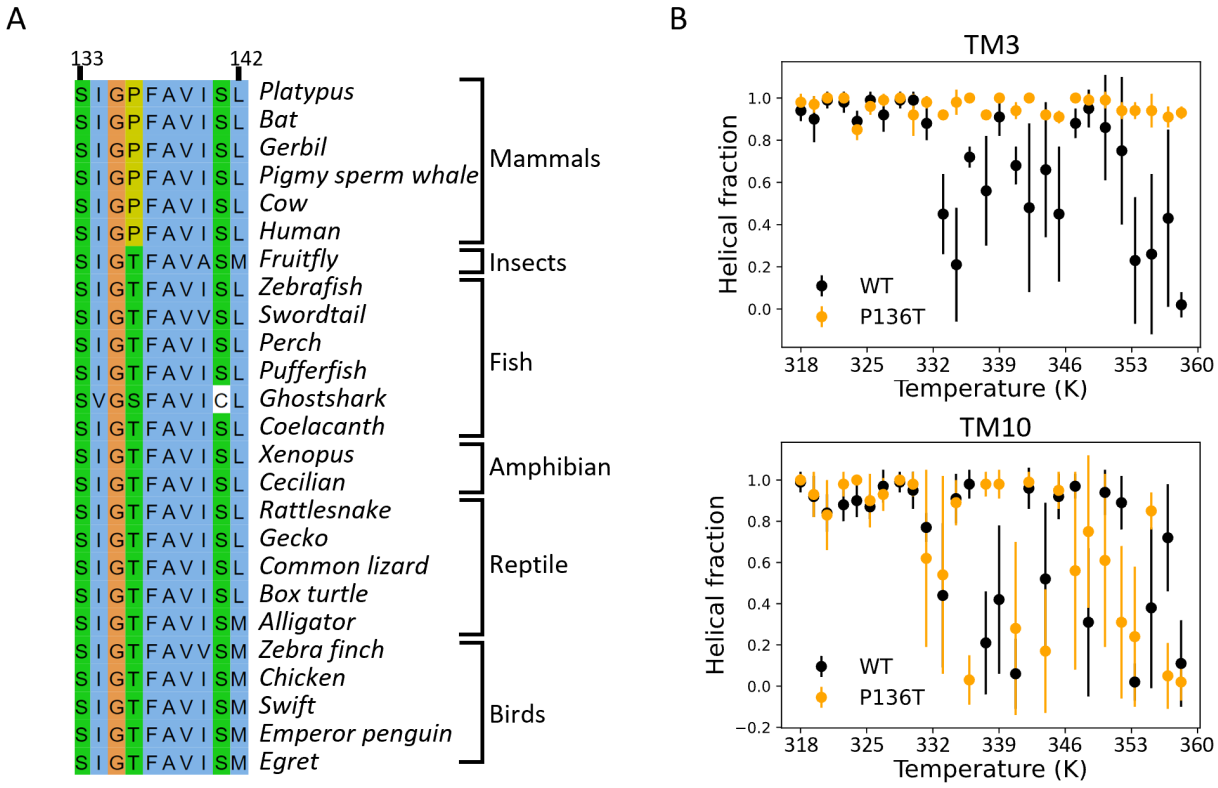

Figure 2.10: Mammalian prestin has a conserved and helix-destabilizing proline 136 on TM3. **(A)** Sequence alignment for the N-terminus of TM3 for prestin across species. A conserved threonine at residue 136 in prestin from other vertebrates is replaced with a proline in mammalian prestin. **(B)** Molecular simulations of thermo-denaturation of prestin conducted with Upside (**Materials and Methods**).[51,52] A P136T mutation largely increases the stability of TM3 but mildly decreases TM10 stability, as compared to wild-type prestin.

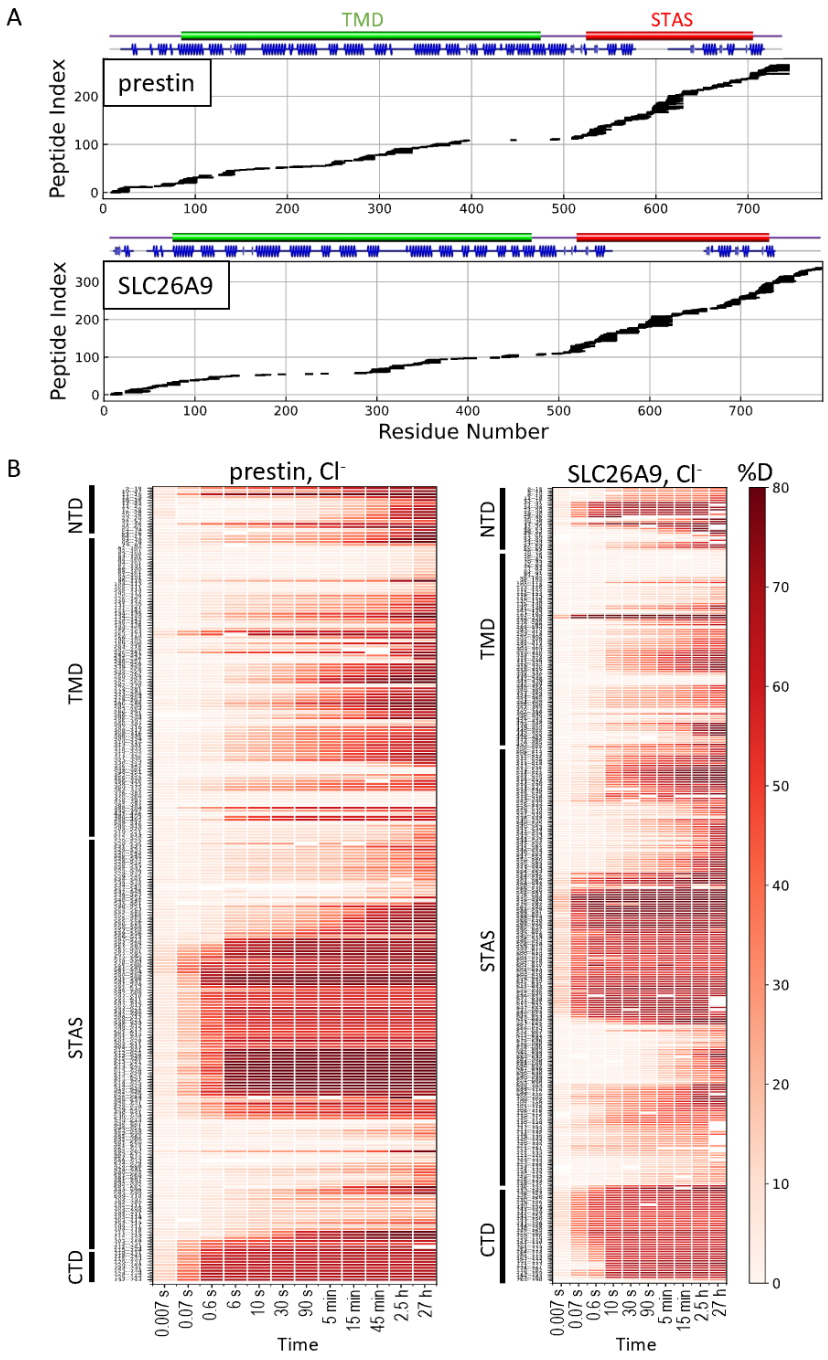

Figure 2.11: HDX-MS sequence coverage and measurements for prestin and SLC26A9 in Cl-. **(A)** Peptide sequence coverage for prestin and SLC26A9 suitable for HDX-MS analysis. On the top indicates the sequence boundary for domains and secondary structures. **(B)** Heatmaps showing deuteration levels of all the peptides at each labeling time for prestin and SLC26A9 measured in Cl^-. Peptide sequences are displayed on the y-axis and legible through high resolution images.

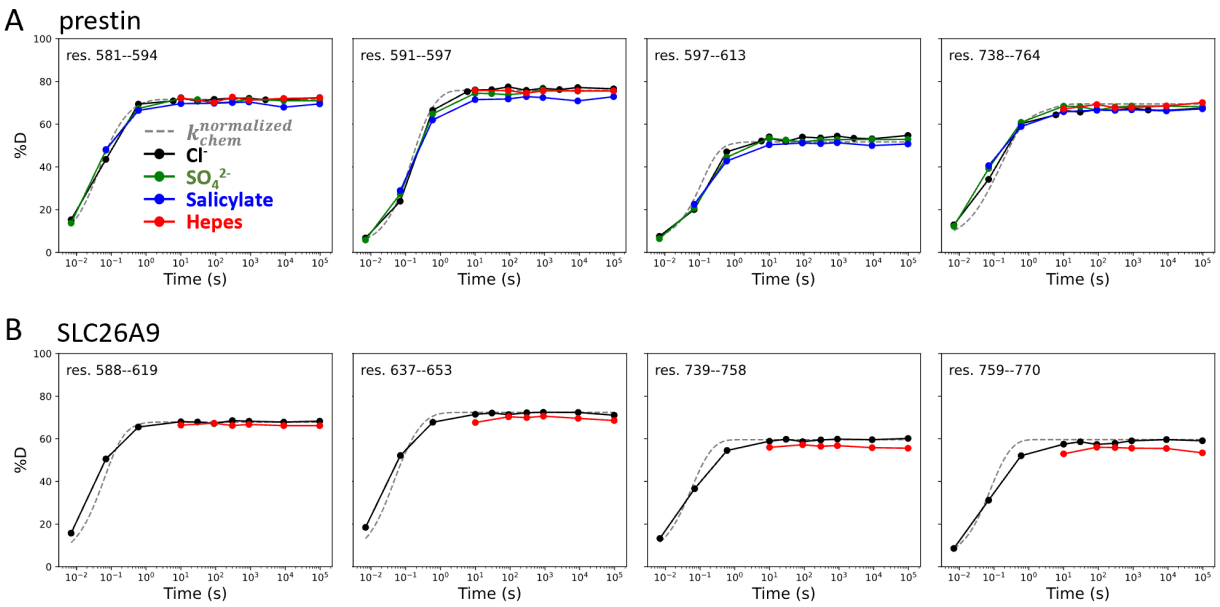

Figure 2.12: Regions unresolved in cryo-EM structures are unfolded in all conditions examined. Deuterium uptake plots for example peptides covering regions unresolved in cryo-EM structures for **(A)** prestin and **(B)** SLC26A9: black, Cl^-; green: SO_4^{2-}; blue: salicylate; red: HEPES. Grey dashed curves represent deuterium uptake with k_{chem}, normalized with the in- and back-exchange levels. Only one replicate for Cl^- and HEPES are shown for clarity.

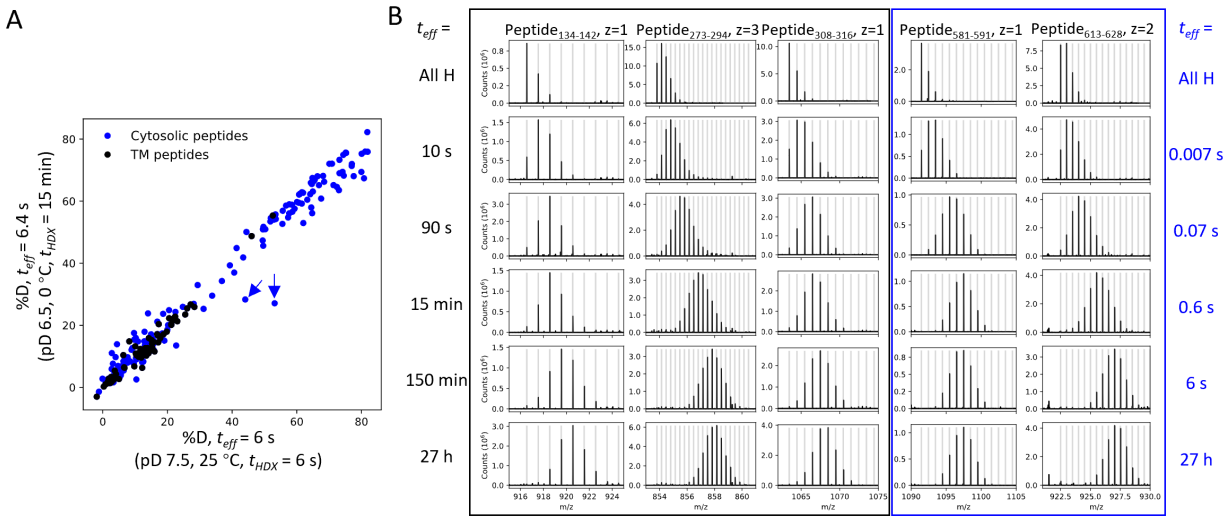

Figure 2.13: HDX for prestin occurs via EX2 mechanism.
(A) Comparison of deuteration levels of all prestin peptides labeled under two HDX conditions: 1) pD_{read} 7.1, 25 °C, t_{HDX} = 6 s; 2) pD_{read} 6.1, 0 °C, t_{HDX} = 15 min, t_{eff} = 6.4 s, where t_{eff} represents effective HDX labeling time in pD_{read} 7.1, 25 °C (**Materials and Methods**). Black: transmembrane (TM) peptides, blue: cytosolic peptides. The two outliers denoted by the blue arrows represent peptides covering the Cα2 helix in the STAS domain, whose large apparent %D difference between the two conditions results from pH-/temperature-dependent dynamics (data not shown). **(B)** Mass spectra of a representative set of peptides showing progressive unimodal isotope envelopes towards high m/z over time. Grey horizontal bars indicate theoretical m/z values for the corresponding isotopes.

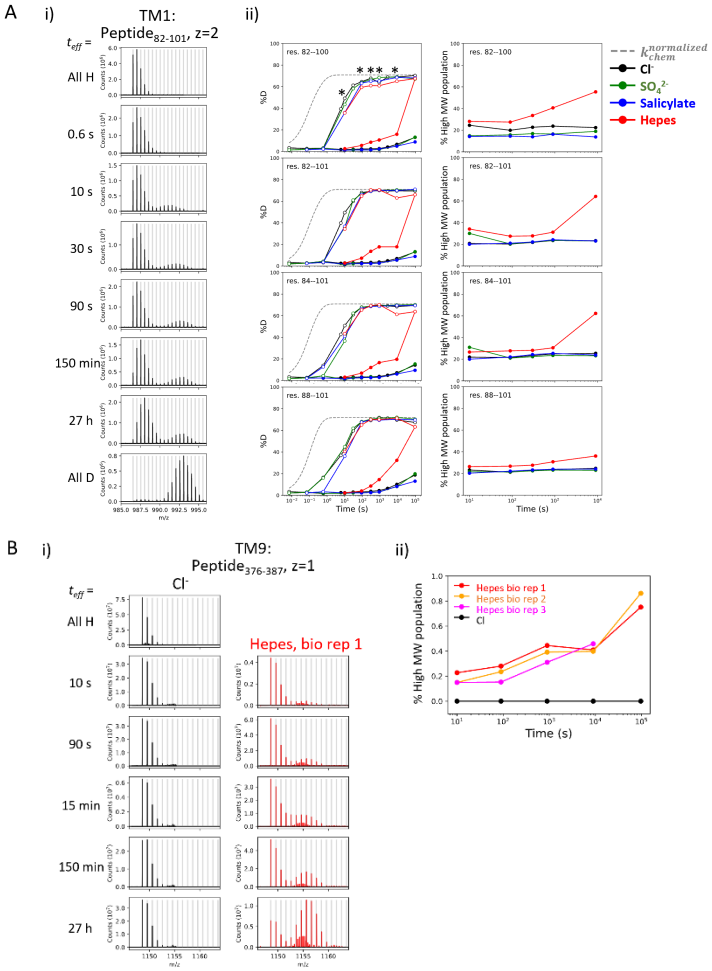

Figure 2.14: Heterogeneity and HDX kinetics in TM1 and TM9.
(A) Conformational heterogeneity at TM1. **(i)** Example mass spectra for a TM1 peptide showing bimodal isotope envelopes, with both isotope distributions increasing in mass over time and exchanging via EX2 kinetics. **(ii) Left:** Deuterium uptake curves of example TM1 peptides plotting both the left (filled markers) and the right (empty markers) isotope envelopes under different anion conditions. Grey dashed curves represent deuterium uptake with k_{chem}, normalized with the in- and back-exchange levels. Only one replicate is shown for clarity. Asterisks represent time points used for the **(Right)** population fraction analysis, chosen as two isotope envelopes are well separated. Fractions of the heavier envelope (i.e., % High MW population) in HEPES are higher than those in other conditions as the left envelope merges into the right envelope, resulting in less distinct separation between the two envelopes. **(B)** HDX for prestin's TM9 exhibits EX1 kinetics in the apo state. **(i)** Example mass spectra for a TM9 peptide measured for prestin in Cl^- (black) and HEPES (red). Identification of EX1 kinetics in HEPES is supported by the presence of two distinct mass envelopes, with the amplitude of the lighter envelope decreasing with a commensurate increase in the heavier envelope over time.[61] **(ii)** The fraction of the heavier envelope over time for prestin in Cl^- (black) and HEPES (3 biological replicates are shown).

Figure 2.15: Deuterium uptake curves for all peptides covering prestin's transmembrane domain. Two deuterium uptake plots are shown for each peptide – left plot: Cl^- (black) and HEPES (red); right plot: Cl^- (black), SO_4^{2-} (green), salicylate (blue), and prestin in nanodisc in Cl^- (orange). Except for the orange curves, all other HDX data were collected on GDN-solublized prestin. Replicates (circles, triangles, and squares): 2 in Cl^-, 3 in HEPES, biological. Peptides covering TM9 (S9.88-S9.91) exhibited EX1 behavior in HEPES (**Fig. S8B**).

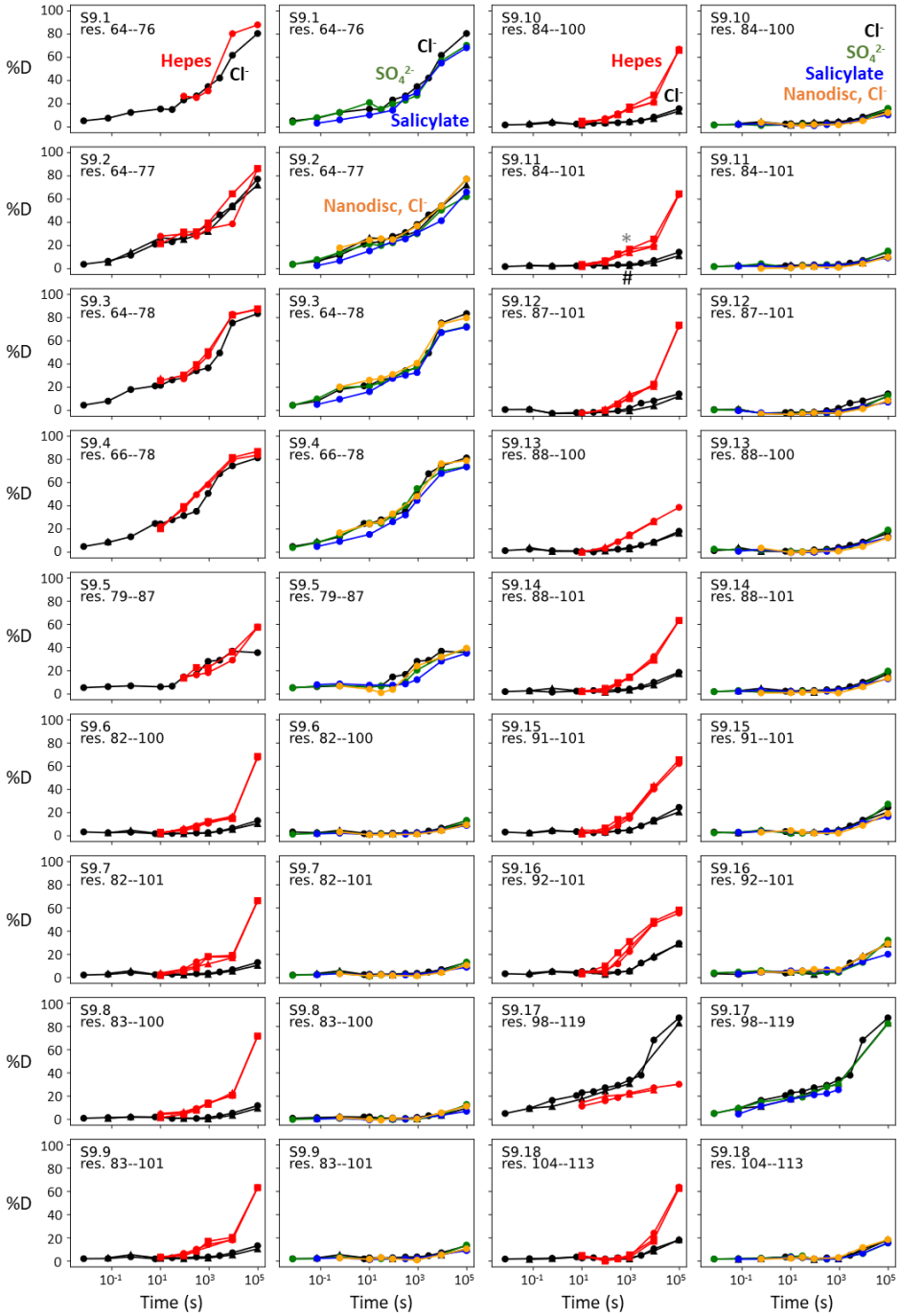

Figure 2.15 (continued)

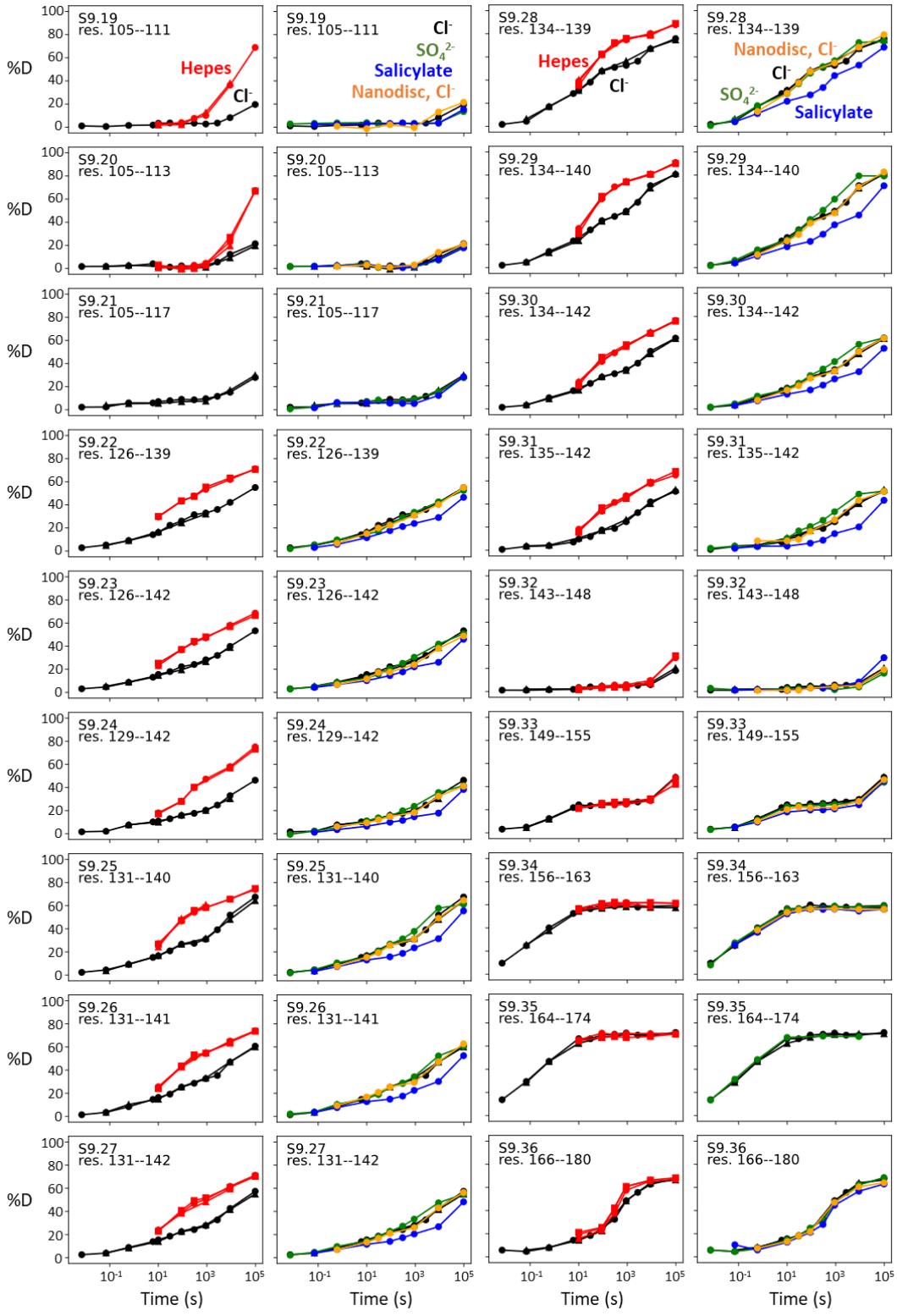

Figure 2.15 (continued)

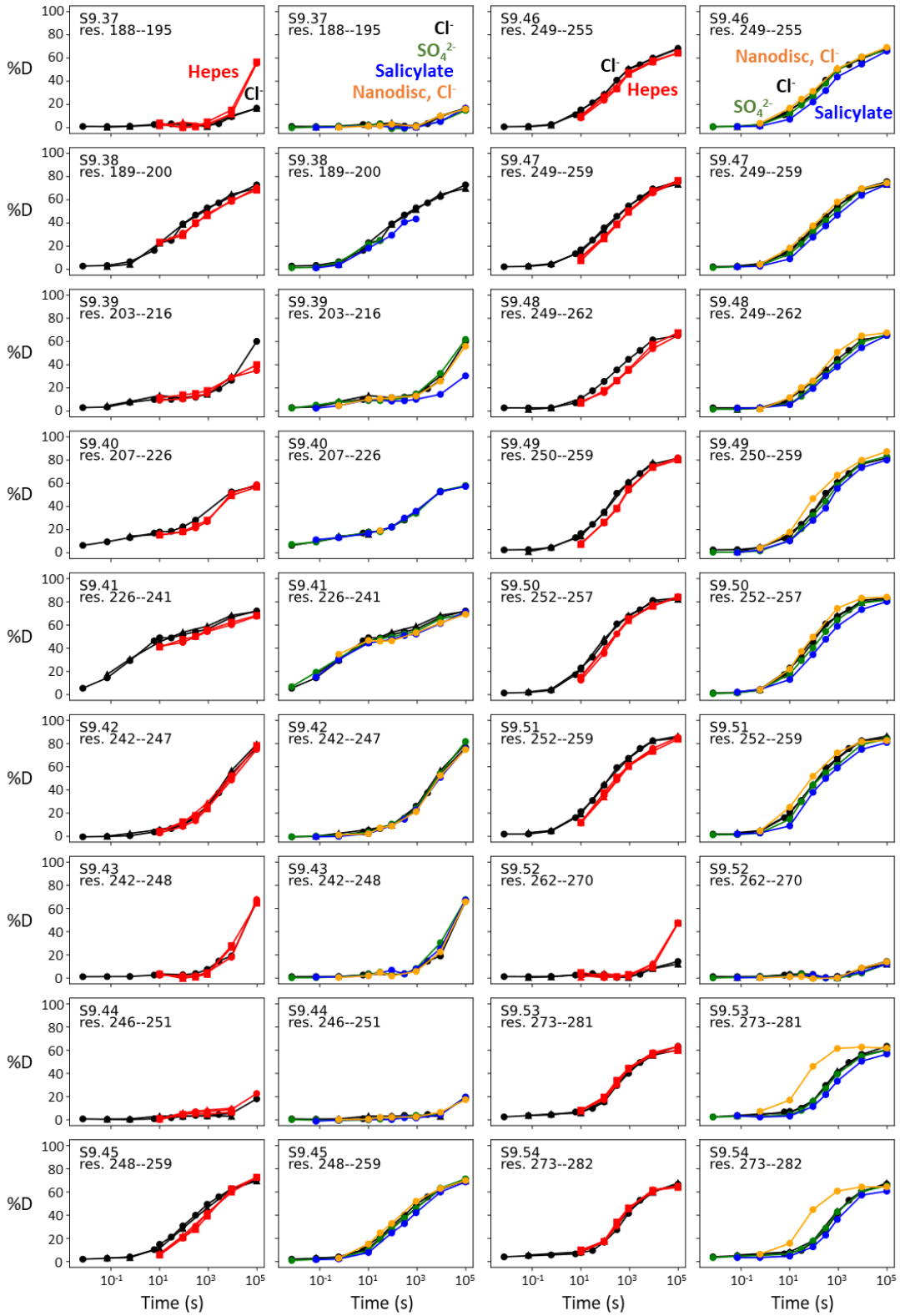

Figure 2.15 (continued)

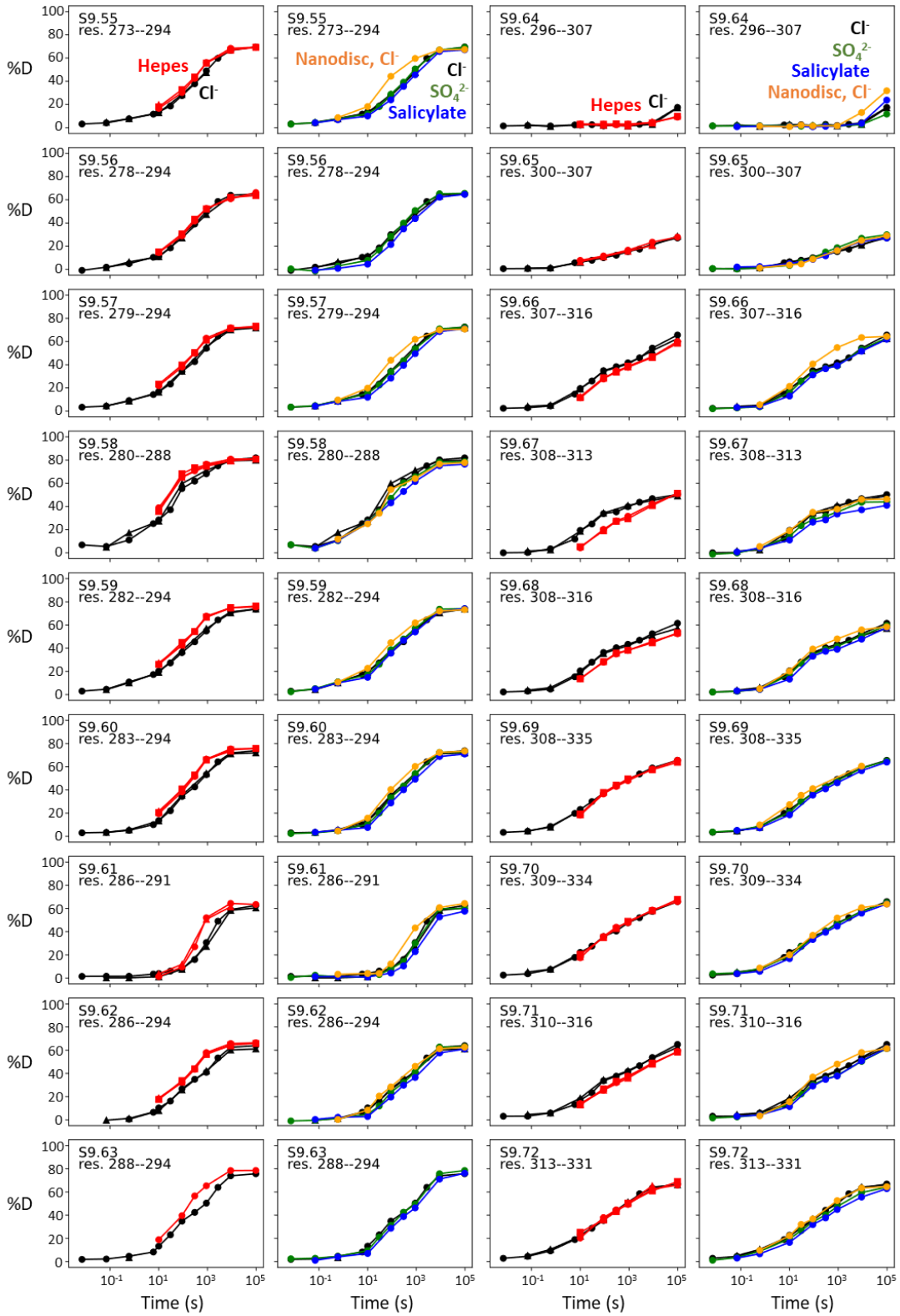

Figure 2.15 (continued)

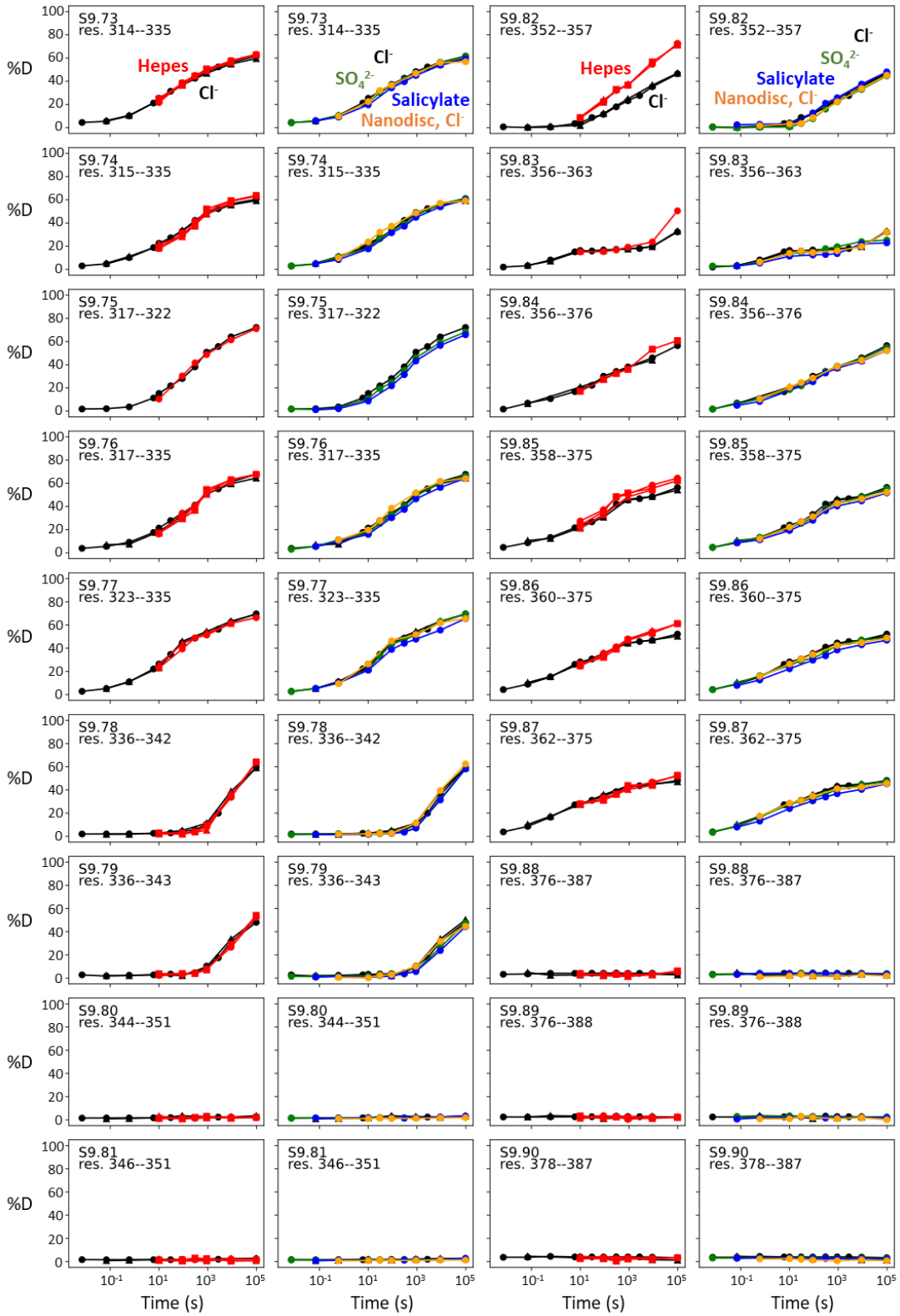

Figure 2.15 (continued)

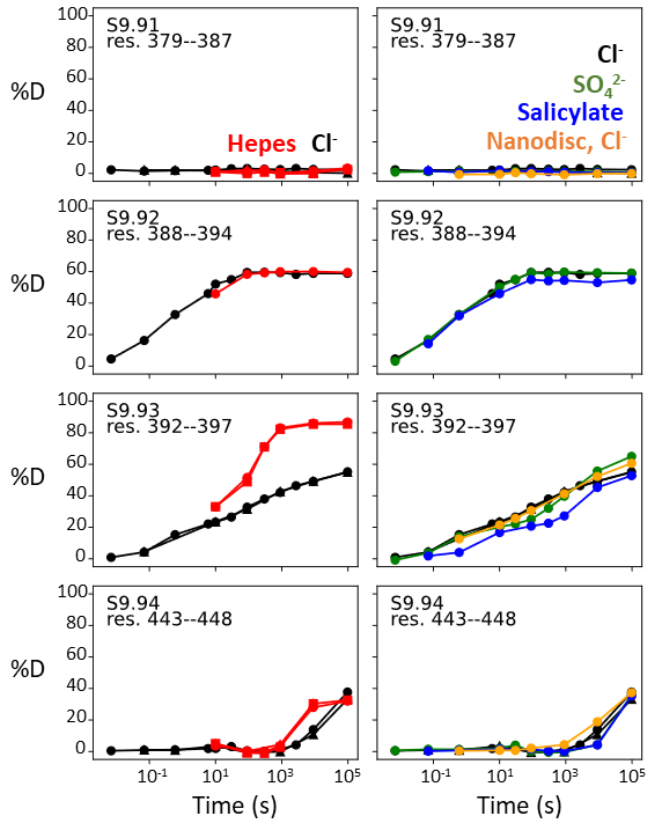

Figure 2.16: Deuterium uptake curves for all peptides covering SLC26A9's transmembrane domain.
One deuterium uptake plot is shown for each peptide – Cl^- (black) and HEPES (red). Three technical replicates are shown as circles, triangles, and squares. All HDX data were collected on GDN-solubilized SLC26A9.

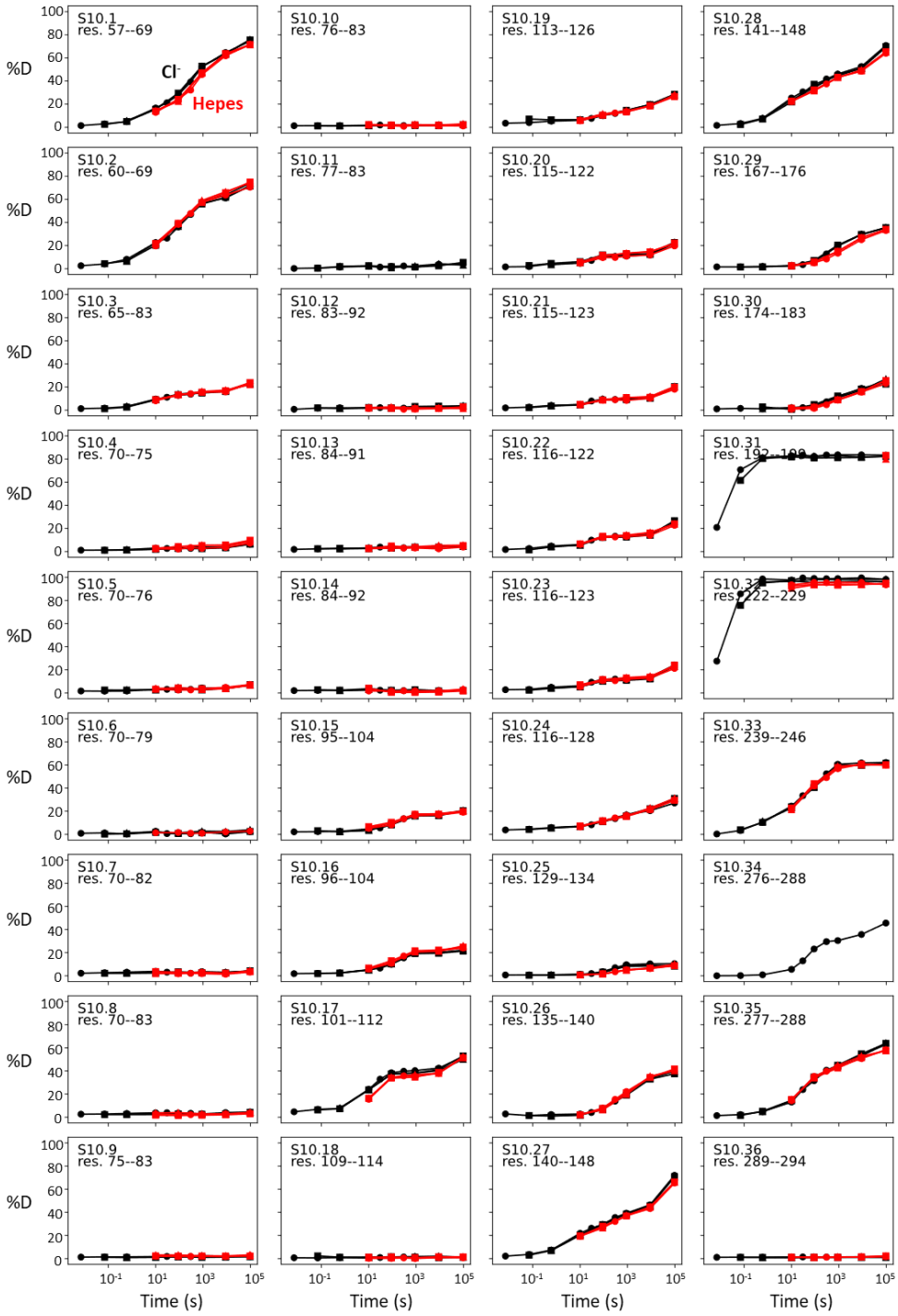

Figure 2.16 (continued)

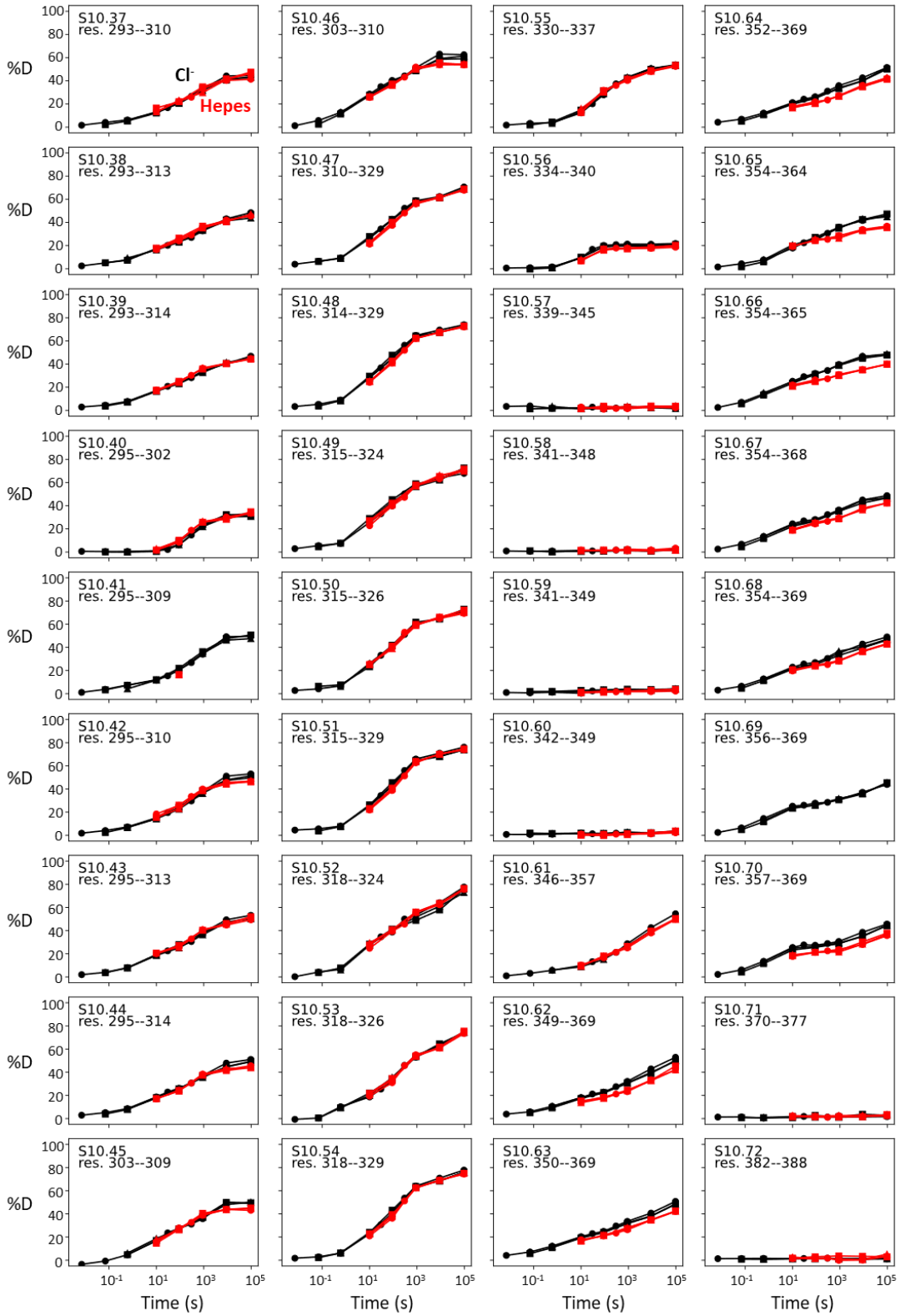

Figure 2.16 (continued)

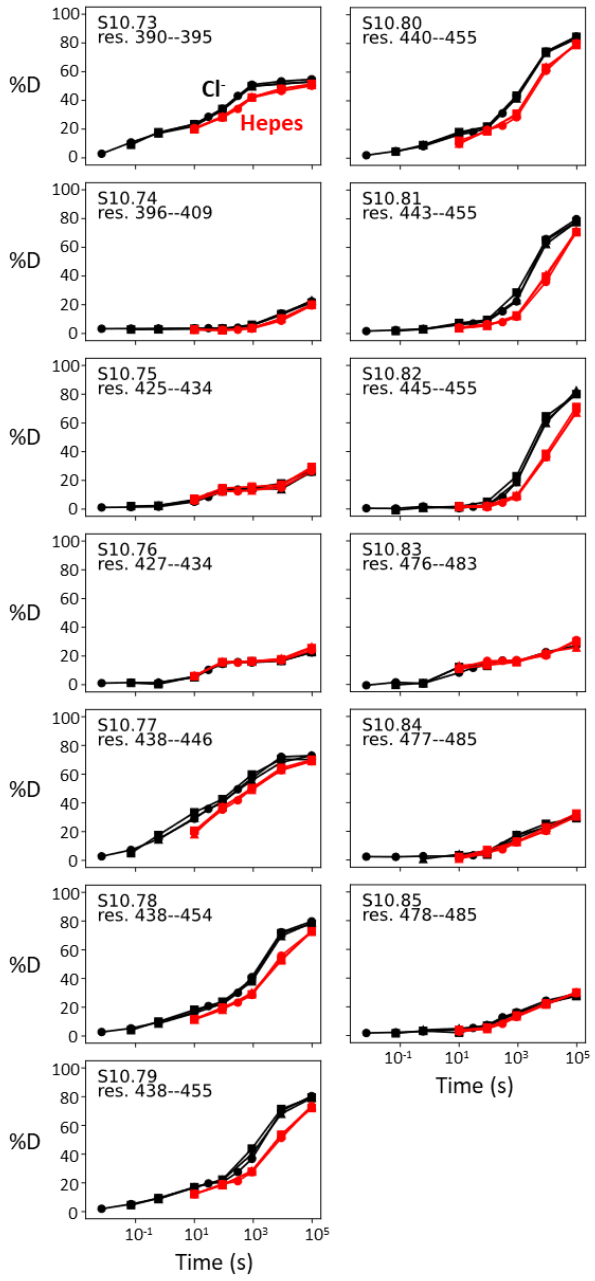

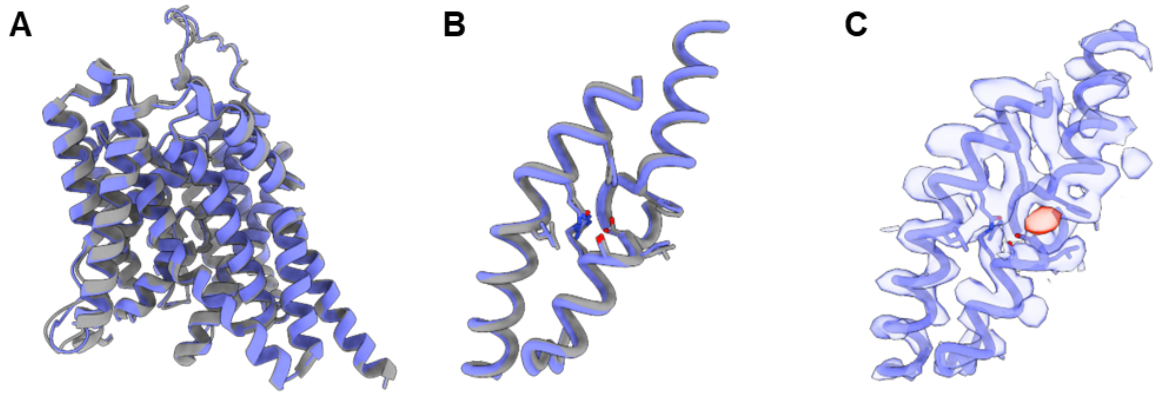

Figure 2.17: The cryo-EM structure for prestin in a HEPES-based buffer containing 1 mM Cl- (blue; PDB 8UC1) highly resembles the structure in the reported Cl--bound state.
(A) Overlay of prestin's TMD with that solved in a high-chloride buffer (grey; PDB 7S8X). **(B)** Overlay of TM1, TM3, and TM10, with key residues that make up the anion-binding site. **(C)** Cryo-EM density forming the anion-binding site (blue). Additional density (red) that is incompatible with the placing of a HEPES molecule was resolved at the anion-binding site.

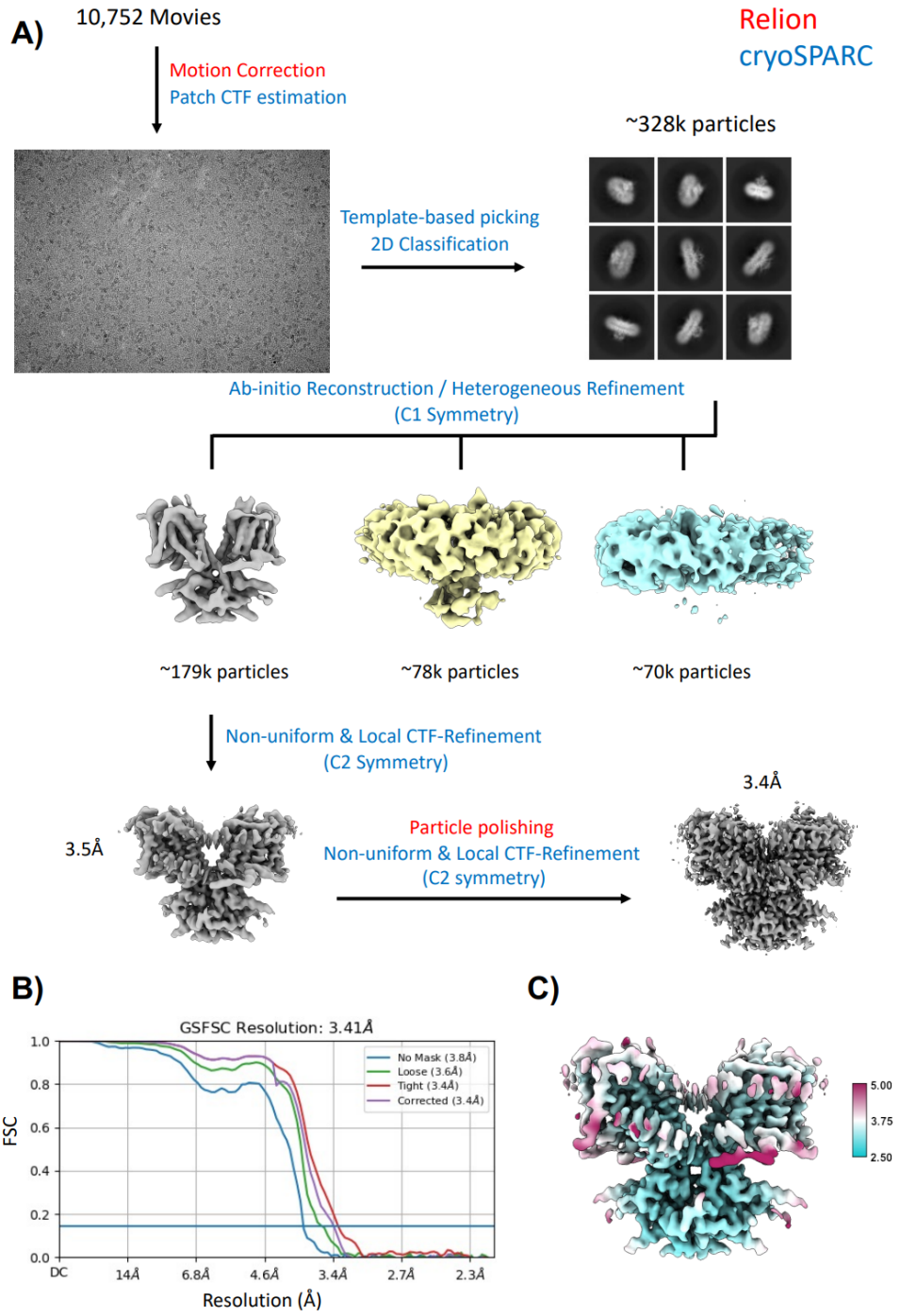

Figure 2.18: Workflow for the processing of the cryo-EM data.
(A) Steps indicated in red font were performed in Relion, steps indicated in blue were performed in cryoSPARC. **(B)** FSC curve showing that the final reconstruction reached a nominal resolution of 3.4 Å (at FSC=0.143). **(C)** Local resolution estimation of the final reconstruction.

Table 1: Biochemical and statistical details for HDX

Dataset	Prestin, Cl^-	Prestin, HEPES (apo)	prestin, SO_4^{2-}	prestin, salicylate	prestin, nanodisc, Cl^-	Slc26a9, Cl^-	Slc26a9, HEPES (apo)
HDX reaction details	360 mM NaCl, 20 mM Tris (NaPi for pD_{read} 6.1, 0 °C), 3 mM DTT, 1 mM EDTA, 0.02% GDN. pD_{read} 7.1, 25 °C or pD 6.5, 0 °C	150 mM HEPES, 0.02% GDN. pD_{read} 7.1, 25 °C	140 mM Na_2SO_4, 5 mM $MgSO_4$, 20 mM NaPi, 0.02% GDN. pD_{read} 7.1, 25 °C or pD_{read} 6.1, 0 °C	140 mM Na_2SO_4, 5 mM $MgSO_4$, 50 mM salicylate, 20 mM NaPi, 0.02% GDN. pD_{read} 7.1, 25 °C or pD_{read} 6.1, 0 °C	20 mM Tris (NaPi for pD_{read} 6.1, 0 °C), 150 mM NaCl. pD_{read} 7.1, 25 °C or pD 6.5, 0 °C	360 mM NaCl, 20 mM Tris (NaPi for pD 6.5, 0 °C), 3 mM DTT, 1 mM EDTA, 0.02% GDN. pD_{read} 7.1, 25 °C or pD_{read} 6.1, 0 °C	150 mM HEPES, 0.02% GDN. pD_{read} 7.1, 25 °C
HDX time course (*: replicated. Times in parenthesis: times in pD_{read} 7.1, 25 °C after correcting for the k_{chem} difference)	pD_{read} 6.1, 0 °C: 1s (0.007s), 10s (0.07s)*, 90s (0.6s)*; pD_{read} 7.1, 25 °C: 6s, 10s*, 30s, 90s*, 5min, 15min*, 45min, 150min*, 27h*	pD_{read} 7.1, 25 °C: 10s*, 90s*, 5min*, 15min*, 150min*, 27h*	pD_{read} 6.1, 0 °C: 1s (0.007s), 10s (0.07s), 90s (0.6s); pD_{read} 7.1, 25 °C: 10s, 30s, 90s, 5min, 15min, 150min, 27h	pD_{read} 6.1, 0 °C: 1s (0.007s), 90s (0.6s); pD_{read} 7.1, 25 °C: 10s, 90s, 5min, 15min, 150min, 27h	pD_{read} 6.1, 0 °C: 90s (0.6s); pD_{read} 7.1, 25 °C: 10s, 90s, 15min, 150min, 27h	pD_{read} 6.1, 0 °C: 1s (0.007s), 10s (0.07s)*, 90s (0.6s)*; pD_{read} 7.1, 25 °C: 10s*, 30s, 90s*, 5min, 15min*, 150min*, 27h*	pD_{read} 7.1, 25 °C: 10s*, 90s*, 15min*, 150min*, 27h*
HDX control samples	Non-deuterated control; in-exchange control; maximally labeled control					Non-deuterated control; in-exchange control; maximally labeled control	

Table 1: Biochemical and statistical details for HDX (continued)

In- and back-exchange, mean/IQR	In-exchange: 3.1% / 2.0%; back-exchange: 27% / 14%					In-exchange: 2.5% / 1.9%; back-exchange: 29% / 17%	
No. of peptides	266 (TMD: 95; cytosolic: 171)	265 (TMD: 94; cytosolic: 171)	266 (TMD: 95; cytosolic: 171)	265 (TMD: 94; cytosolic: 171)	256 (TMD: 85; cytosolic: 171)	338 (TMD: 85; cytosolic: 253)	335 (TMD: 82; cytosolic: 253)
Sequence coverage	83% (TMD: 75%; cytosolic: 95%)	83% (TMD: 75%; cytosolic: 95%)	83% (TMD: 75%; cytosolic: 95%)	83% (TMD: 74%; cytosolic: 95%)	79% (TMD: 67%; cytosolic: 95%)	81% (TMD: 68%; cytosolic: 96%)	81% (TMD: 68%; cytosolic: 96%)
Average peptide length/redundancy	12.2/4.3	12.2/4.3	12.2/4.3	12.2/4.3	12.2/4.1	12.5/5.3	12.5/5.3
Replicates	2 (Biological)	3 (Biological)	1	1	1	3 (Technical)	3 (Technical)
Repeatability (TM peptides only)	0.69%/0.06 Da (average SD of the Δ%D/Δ#D between the duplicates)	0.93%/0.09 Da (average SD)	N/A	N/A	N/A	0.64%/0.06 Da (average SD)	0.60%/0.05 Da (average SD)
Significant differences in HDX (ΔHDX > X Da, TM peptides only)	N/A	0.22 Da (95% CI)	N/A	N/A	N/A	0.14 Da (95% CI)	0.13 Da (95% CI)
	0.17 Da (95% CI)		N/A	N/A	N/A	0.11 Da (95% CI)	

3 DEVELOPMENT AND APPLICATIONS OF IN VIVO HDX-MS

This chapter is the publication by Lin, Xiaoxuan, Adam M. Zmyslowski, Isabelle A. Gagnon, Robert K. Nakamoto, and Tobin R. Sosnick. “Development of in Vivo HDX-MS with Applications to a TonB-Dependent Transporter and Other Proteins.” *Protein Science* 31, no. 9 (2022): e4402. https://doi.org/10.1002/pro.4402**.**

3.1 Development of *in vivo* HDX-MS with applications to a TonB-dependent transporter and other proteins.

Xiaoxuan Lin[1], Adam M. Zmyslowski[1*], Isabelle A. Gagnon[1], Robert K. Nakamoto[4], Tobin R. Sosnick[1-3ł]

[1]Department of Biochemistry and Molecular Biology, [2]Pritzker School for Molecular Engineering, [3]Institute for Biophysical Dynamics, The University of Chicago, Chicago, IL, 60637, USA.

[4]Department of Molecular Physiology and Biological Physics, University of Virginia, Charlottesville, VA, 22908, USA.

*Current address: Evozyne LLC., 2430 N Halsted St, Chicago, IL, 60614, USA.

trsosnic@uchicago.edu[ł]Corresponding author:

3.1.1 Abstract

Hydrogen-deuterium exchange mass spectrometry (HDX-MS) is a powerful tool that monitors protein dynamics in solution. However, the reversible nature of HDX labels has largely limited the application to *in vitro* systems. Here we describe a protocol for measuring HDX-MS in living *E. coli* cells applied to BtuB, a TonB-dependent transporter found in outer membranes (OMs). BtuB is a convenient and biologically interesting system for testing *in vivo* HDX-MS due to its controllable HDX behavior and large structural rearrangements that occur during the B12 transport cycle. Our previous HDX-MS study in native OMs provided evidence for B12 binding and breaking of a salt bridge termed the *Ionic Lock*, an event that leads to the unfolding of the amino terminus. Although purified OMs provide a more native-like environment than reconstituted systems, disruption of the cell envelope during lysis perturbs the linkage between BtuB and the TonB complex that drives B12 transport. The *in vivo* HDX response of BtuB's plug domain (BtuBp) to B12 binding corroborates our previous *in vitro* findings that B12 alone is sufficient to break the *Ionic Lock*. In addition, we still find no evidence of B12 binding-induced unfolding in other regions of BtuBp that could enable B12 passage. Our protocol was successful in reporting on the HDX of several endogenous *E. coli* proteins measured in the same measurement. Our success in performing HDX in live cells opens the possibility for future HDX studies in a native cellular environment.

3.1.2 Importance

We present a protocol for performing *in vivo* HDX-MS, focusing on BtuB, a protein whose native membrane environment is believed to be mechanistically important for B12 transport. The *in vivo*

HDX-MS data corroborates the conclusions from our previous *in vitro* HDX-MS study of the allostery initiated by B12 binding. Our success with BtuB and other proteins opens the possibility for performing additional HDX studies in a native cellular environment.

3.1.3 Introduction

Hydrogen-deuterium exchange (HDX) is a powerful biophysical technique that monitors protein dynamics. Information on solvent accessibility and conformational fluctuations of backbone amide protons is obtained without the need for mutations or synthetic labels.[1–3] In combination with mass spectrometry (MS), the HDX-MS technique has been applied to a variety of soluble and membrane proteins. Notably, the method allows one to study a protein's dynamics and thermodynamics, information potentially with residue-level resolution.[4–8] However, the reversible nature of the deuterium label demands rapid sample work-up under conditions carefully selected to limit the loss of the label prior to MS analysis, a process termed "back exchange". This process has limited the application of HDX-MS to *in vitro* systems. Here, we report an *in vivo* application of HDX-MS and demonstrate the potential of the technique to probe complex biological systems whose function may depend on being in a native cellular environment.

BtuB, the *E. coli* outer membrane (OM) vitamin B12 transporter, is a well-studied member of the TonB-dependent transporter family.[9–11] BtuB is a convenient and biologically interesting protein for testing *in vivo* HDX-MS due to its controllable HDX behavior and the enigmatic conformational rearrangements involved in pore formation during the B12 transport cycle. Despite intense study, key aspects of the transport mechanism remain unknown, most notably the

conformational changes involved in pore formation and the coupling to the TonB complex.[9,12] Recent studies have found evidence that BtuB undergoes different rearrangements in living cells compared to reconstituted systems, especially those employing detergents.[13,14]

Our previous HDX-MS study of BtuB, conducted in a partially purified OM, provided evidence for B12 binding-induced allostery in the luminal domain related to the unfolding of the amino-terminal region.[15] While studying outer membrane proteins (OMPs) in native OMs is a considerable advance over reconstituted systems, OMs still lack important features that are only present in an intact cellular context. The transport function of BtuB may rely on lipopolysaccharide, an energized inner membrane (IM), or peptidoglycan,[13,14,16–18] yet all of these are disrupted upon cell lysis. Additionally, the sarkosyl treatment employed to remove the IM from our previous OM preparations[15] may have introduced additional perturbations to the BtuB dynamics.[14,15,19]

Here we conducted HDX-MS on BtuB in live *E. coli*. HDX labeling was initiated by transferring *E. coli* overexpressing BtuB into deuterated growth media. Our post-HDX lysis and purification conducted under HDX quench conditions (e.g., 2 °C, pH 2.5) limited back exchange to manageable levels. The *in vivo* HDX data for BtuB's plug domain (BtuBp) are similar to our prior data obtained in OMs, particularly the B12 binding-induced unfolding of the amino terminus.[15] Finally, we discuss the conditions necessary for performing HDX-MS *in vivo* on other proteins and provide examples of endogenous *E. coli* proteins whose HDX was observed in the same measurements.

3.1.4 Results

The primary challenge in conducting HDX-MS *in vivo* is obtaining peptides from a live sample while minimizing loss of the deuterium label to back exchange. Sample purification, which had occurred during the period between cell harvesting and initiation of HDX, is now conducted post-HDX labeling and under quench conditions. This necessitates optimization of the protocol to strike a compromise between sample quantity, purity, and back exchange. Our *in vivo* HDX-MS protocol provides a solution to this challenge for the OMP BtuB (Figure 3.1 A).

HDX was initiated by transferring a culture of *E. coli* overexpressing BtuB into a deuterated growth medium (22 °C, pD_{read} 6.8). A carbon source was included during HDX labeling to prevent starvation, although HDX was insensitive to the addition of LB medium, most likely because of our short, sub-10 min labeling time (Figure 3.5). After labeling, HDX was quenched, cells were lysed by cryogenic disruption, and the lysate was resuspended in the quench buffer and ultracentrifuged at 100,000 x g, 2°C for 20 min. This centrifugation time is shorter than typically used for membrane proteins but it was sufficient to obtain BtuB samples suitable for MS analysis. Our protocol generated peptides with a sequence coverage comparable to that obtained *in vitro* (Figure 3.1 B; Table 2). Although the presence of endogenous *E. coli* proteins increased the level of background signals, we were able to obtain nearly full coverage of BtuBp, including the overlapping series of amino-terminal peptides that exhibited the greatest changes in HDX upon B12 binding *in vitro*. Mass spectra representative of our signal-to-noise levels are displayed in Figure 3.6.

As expected, back exchange levels for HDX *in vivo* were systematically higher than those *in vitro*, mostly due to an increase in post-quench sample handling time. Nevertheless, the HDX

response of BtuBp to B12 binding was still confidently measured and consistent with our previous findings *in vitro*. In this paper we continue the use of our prior nomenclature for describing peptides and regions;[15] regions are capitalized while the sequence endpoints are denoted in the subscript, with corresponding peptides in parentheses, e.g., BtuB's amino terminus is covered by $Region_{3\text{-}8}$ ($Peptide_{1\text{-}8}$).

3.1.4.1 *The in vivo allosteric response of BtuBp to B12 binding.*

The B12 binding-induced stability changes seen throughout BtuBp qualitatively agreed with previous *in vitro* observations, exhibiting similar trends in HDX acceleration or slowing (Figure 2). The similarity included our primary finding related to the *Ionic Lock (IL)*, a conserved salt bridge between Arg14 and Asp316.[14,20] We[15] and others[14] found that the binding of B12 results in breakage of the *IL*, unfolding of the *IL* region, and exposure of the Ton box, thereby allowing the Ton box to bind TonB. *In vivo*, we continued to find that the peptides covering the *IL* region ($Peptides_{9\text{-}23,\ 9\text{-}27,\ and\ 9\text{-}30}$) exhibited the greatest response to B12 binding, a ~1000-fold acceleration in HDX, agreeing with our *in vitro* HDX-MS measurements (Figure 3.3 A & Figure 3.9 S5.3-5.4).

B12 binding also caused a slight destabilization of the amino terminus of the Ton box and the substrate binding loop 3 (SB3), as indicated by the acceleration of HDX for $Region_{3\text{-}8}$ ($Peptide_{1\text{-}8}$) and $Region_{82\text{-}87}$ ($Peptides_{80\text{-}85\ and\ 80\text{-}87}$), respectively (Figure 3.2 & Figure 3.9 S5.19). Again, this behavior matched our *in vitro* HDX findings. Furthermore, we observed B12 binding-induced stabilization of SB2, as indicated by a slight slowing of HDX for $Region_{68\text{-}79}$ ($Peptide_{6\text{-}79,\ 67\text{-}69,\ and\ 68\text{-}79}$) (Figure 3.2 & Figure 3.9 S5.16-5.18). BtuBp's amino-terminal helices were unaffected by

B12 binding, as indicated by the unchanged HDX levels for Region$_{26\text{-}46}$ (Peptides$_{24\text{-}43,\ 24\text{-}44,\ 24\text{-}46,\ 24\text{-}53,\ \text{and}\ 28\text{-}46}$) (Figure 3.2 & Figure 3.9 S5.5-5.9). In summary, the *in vivo* measurements recapitulated all of the major B12 binding-induced changes in HDX observed *in vitro*.

Because endogenous TonB-ExbB-ExbD complexes were still present in our *in vivo* measurements, one may consider that the HDX reflected the time and ensemble average for BtuBp in a functional B12 transport cycle. Catching BtuB during the transport cycle, however, is unlikely due to the high molar excess of overexpressed BtuB molecules relative to naturally abundant TonB-ExbB-ExbD complexes.[21,22] Under our B12 concentration of 16 μM, we expect that most BtuB molecules were in the B12-bound state, as endogenous levels of TonB complex were likely insufficient to drive the transport cycle for a detectable fraction of the BtuB molecules.[21]

Additionally, TonB action during the BtuB transport cycle is thought to depend on cellular proton motive force (pmf).[17,23] We conducted *in vivo* HDX-MS on BtuB in the presence of CCCP, a pmf dissipator. BtuBp's HDX was insensitive to CCCP in the presence of B12 (Figure 3.7), arguing against a significant population fraction of BtuB being in the actively transporting state. Hence, we think that the dominant state of BtuB during our experiments was the B12-bound state. To further study the effect of pmf on BtuB's transport mechanism, it may be necessary to overexpress TonB, ExbB, and ExbD[18,24] to similar levels as BtuB.

All important HDX features observed *in vivo* matched the *in vitro* study in spite of the increased back exchange levels. This increase was determined from the maximum final deuteration levels of fully deuterated peptides ($\%D_{max}$), e.g., the $\%D_{max}$ decreased from 78% (*in vitro*) to 28% (*in vivo*) for Peptide$_{9\text{-}23}$. To examine which steps were responsible for the additional loss of deuterium, we increased the ultracentrifugation time from 20 to 40 min. For Peptide$_{9\text{-}23,}$ this

increase led to the $\%D_{max}$ falling from 28% to 22% (Figure 3.8), a level that is consistent with BtuBp being unfolded under quench conditions during ultracentrifugation, and having an intrinsic exchange rate of 77 min^{-1} at pH 2.5, 2 °C. Similar results were observed in the peptides that became fully deuterated, indicating that the 20-min ultracentrifugation step was a significant source of back exchange in our experiments.

3.1.4.2 In vivo HDX of endogenous proteins co-measured with BtuB.

During our experiments targeting BtuB, we fortuitously identified peptides comprising 8% of the *E. coli* strain K12 proteome (346/4438 proteins, Table 3). As a result, we were able to obtain HDX data for several endogenous proteins, including GroEL, Histone-like DNA binding proteins (HU-α and HU-β), and Elongation factor Tu 2 (EF-Tu2) (Figure 3.4 & Table 3). HDX for these four proteins exhibited high reproducibility and was insensitive to B12 addition, as expected (Figure 3.4).

3.1.5 Discussion

HDX-MS has become a widely used tool for both soluble and membrane proteins.[4–8] The method, however, has been limited to *in vitro* studies using purified components. Here we present a protocol for performing HDX-MS on an OMP in live *E. coli* cells.

A potential concern for conducting HDX on live cells is that D_2O may not permeate across the membrane bilayers and only the outward-facing components would be labeled. However, several studies have demonstrated that D_2O permeation across the bilayer[25] occurs within 1 msec

at 23 °C for 90% PC/10% cholesterol liposomes[26] and equilibrates within 200 msec at 22 °C with DPPC[27]. Furthermore, HDX-NMR studies on Tom40 embedded in DMPC liposomes observed labeling of both inward- and outward-facing residues.[28]

BtuB provides a convenient system for testing *in vivo* HDX-MS for two main reasons. First, as an OMP, BtuB can be highly overexpressed[15] and effectively separated from cytosolic proteins via ultracentrifugation. Together with preferential proteolytic cleavage, these three effects enrich MS signals from BtuBp above those from other proteins (Table 3). Secondly, the B12-induced changes in HDX with BtuBp are readily controllable and large enough to be observed even with high back exchange levels.

Despite the smaller differences in absolute deuteration levels due to increased back exchange, we continued to observe the ~1000-fold HDX acceleration at the *IL* region as a result of B12 binding (Figure 3.3 A). Such quantitative agreement of B12-binding effects *in vivo* and *in vitro* corroborates our previous finding that the binding of B12 alone is sufficient to unfold the *IL* region and enable the binding of TonB to the Ton box (Figure 3.3 B). Furthermore, our *in vivo* HDX-MS data on BtuBp provide no evidence for the formation of a pore large enough for B12 passage, as we see no additional B12 binding-induced unfolding at other regions of BtuBp (Figure 3.2 & Figure 3.9 S5.5-5.25).

3.1.5.1 *HDX Protocol considerations.*

To provide sufficient material for MS, initiating HDX in concentrated cells is desirable. Caution should be taken to minimize cell death during HDX labeling. We recommend that HDX be

conducted on slowly dividing cells in the presence of a carbon source to avoid starvation. A short HDX labeling period is recommended to avoid issues such as cell division and deoxygenation. In our experiments, 10 min is sufficient to fully label peptides covering the *IL* region, although we present time points going out to 150 min. We expect minimal cell death despite the high cell density due to our short label time and inclusion of a carbon source.[29]

The main challenge for conducting *in vivo* HDX-MS is maintaining a low level of back exchange, occurring mainly during the purification of the quenched protein. To reduce back exchange, the post-label steps should be as short as needed to avoid subsequent column fouling and spectral crowding, i.e., one should purify to the minimum level necessary for a system of interest. Sample isolation should be conducted under quench conditions (pH 2.5, 0°C) to reduce intrinsic exchange rates. Specialized LC operating at sub-zero temperatures may also be employed to improve separation.[30,31] Ideally, *in vivo* HDX-MS should be performed without overexpression to preserve the relative protein concentrations, which may be possible with future optimization of the back exchange levels. To facilitate rapid isolation under quench conditions, we are in the process of developing a purification tag that functions at low pH.

Given our success in performing *in vivo* HDX-MS on BtuB, we expect that a similar protocol could be applied to other OMPs as they generally can be highly overexpressed[32] and rapidly separated from cytosolic proteins via ultracentrifugation. However, OMPs are not the only viable target for *in vivo* HDX-MS. During our experiments targeting BtuB, we measured HDX for highly expressed cytosolic proteins (Figure 3.4 & Table 3). These proteins appear to share the qualities of being abundant, easily digestible, and pelletable due to their large sizes or association

with large complexes. Therefore, we expect that our *in vivo* HDX-MS protocol can be applied to a variety of other proteins.

3.1.6 Conclusion

We describe a new protocol conducting HDX-MS on the OMP BtuB in live *E. coli* cells. Critically, the protocol maintained a manageable level of back exchange while providing adequate signals. Our *in vivo* HDX-MS data corroborated previous findings that 1) B12 alone is sufficient to initiate *IL* breakage in BtuB and the unfolding of its amino terminus; 2) B12 binding alone does not create a channel sufficient for B12 transport. Overall, our success with BtuB and other proteins *in vivo* opens the way for future HDX studies of protein function and dynamics in a native cellular environment.

3.1.7 Materials and methods

Chemicals were purchased from Sigma-Aldrich (St Louis, MO) unless otherwise noted.

Bacteria culture and protein expression. BtuB in the pAG1 vector was transformed into BL21-CodonPlus (DE3) *E. coli* competent cells. A single colony was used to inoculate 50 mL of LB media supplemented with 100 μg/mL Ampicillin (LB_{Amp}) and the culture was grown at 37 °C overnight with agitation (225 rpm). The next day, 5 mL of the starting culture was inoculated into 500 mL of LB_{Amp} in a baffled 2.8 L Fernbach flask. The culture was grown at 37 °C until the OD_{600} reached 0.6 and then induced at 37 °C for 4 hours with 1 mM IPTG. Cells were harvested by centrifugation for 10 minutes at 3625 x g at 20 °C. Cells were washed and pelleted twice, each

time with 50 mL of H_2O/LB buffer containing 50 mM NaPi, 150 mM NaCl, 1x LB, pH 7.2, to equilibrate cells in a pH-controlled environment for HDX labeling while providing enough carbon source to maintain cellular metabolism. Washed cells were resuspended in H_2O/LB buffer for a total volume of 5 mL and were immediately used for HDX labeling.

Hydrogen-deuterium exchange. HDX was initiated by diluting 200 μL of the dense cell suspension into 800 μL of 1x LB medium made with D_2O (99.9% D, Sigma-Aldrich ref# 151882), resulting in 80% D in the label reaction. The D_2O/LB buffers were at pD_{read} 6.8 and contained 50 mM NaPi, 150 mM NaCl, 1x LB, and were supplemented with 1) Apo: 1% DMSO; 2) B12: 1% DMSO, 20 μM B12, and 2 mM $CaCl_2$; 3) B12/CCCP: 1% DMSO, 5 μM CCCP, 20 μM B12, and 2 mM $CaCl_2$. For HDX experiments with B12 and CCCP, cells were incubated with 5 μM CCCP for 1 min at 22 °C before labeling was initiated. HDX labeling was performed for 6 sec to 150 min at 22 °C and quenched via the addition of 500 μL of ice-chilled quench buffer (600 mM Glycine, pH 2.5). Quenched cell suspensions were immediately pelleted by centrifugation for 1 min at 6000 x g at 2 °C, re-suspended in 80 μL of ice-chilled quench buffer, and then flash-frozen into cell beads by slow drip into an LN_2-filled 2 mL Eppendorf Safe-Lock Tube (Eppendorf Catalog No. 022363379) containing one 7-mm milling ball. After pouring out the excess LN_2, frozen cell beads were stored at -80 °C until lysis.

Rapid separation of BtuB and LC-MS. Frozen cell beads from each quenched HDX reaction were cryogenically pulverized with a mixer mill (Retsch, MM 400) over 10 cycles, with each cycle consisting of 90-s grinding at 30 Hz followed by 3-min cooling in LN_2. Pulverized lysates were

stored at -80 °C until thawing by repeated trituration in ice-chilled quench buffer. The cell lysate was clarified by centrifugation for 4 min at 13,000 x g, 2 °C. OM-embedded BtuB was separated by ultracentrifugation for 20 min at 100,000 x g, 2 °C. The resulting pellet containing BtuB was re-suspended in 67 μL of an ice-chilled quench mixture consisting of 60 μL of 600mM glycine, 2 M urea, pH 2.5, 2 μL of thrice-desalted 5 mg/mL porcine pepsin (Sigma-Aldrich, ref# P6887) in 100 mM sodium citrate, 2.5 μL of 2.5 mM DDM, and 2.5 μL of a 300 mg/mL aqueous suspension of ZrO_2 coated silica (Sigma-Aldrich, ref# 55261- U). Digestion with pepsin was carried out by 3 min incubation at 0 °C. Solubilized peptides were obtained by filtering the resulting mixture through a cellulose acetate spin cup (Thermo Pierce, Waltham, MA ref# 69702) by centrifugation for 30 sec at 13,000 x g, 2 °C. The filtrate was flash-frozen in a dry ice/EtOH bath and stored at -80 °C until injection onto the LC-MS system. The LC-MS system used and data analysis performed were described previously.[15] Data points that could not be fit by HDExaminer 3.1 were excluded.

3.1.8 Author Contributions

Xiaoxuan Lin: Conceptualization (equal); data curation (lead); formal analysis (lead); investigation (lead); methodology (equal); validation (lead); visualization (lead); writing – original draft preparation (lead); writing – review & editing (equal). **Adam M. Zmyslowski:** Conceptualization (equal); data curation (supporting); investigation (supporting); methodology (equal); validation (supporting); writing – review & editing (supporting). **Isabelle A. Gagnon:** Investigation (supporting). **Robert K. Nakamoto:** Validation (supporting); writing – review & editing (supporting). **Tobin R. Sosnick:** Conceptualization (supporting); funding acquisition

(lead); project administration (lead); resources (lead); supervision (lead); validation (supporting); visualization (supporting); writing – review & editing (equal).

3.1.9 Acknowledgments

We thank J. Shangguan for assistance in experiments, A. Drummond for providing the mixer mill, and M. Baxa for input and maintenance of the mass spectrometer. This work was supported by NIH Research Grant R01 GM055694.

3.1.10 Figures and Tables

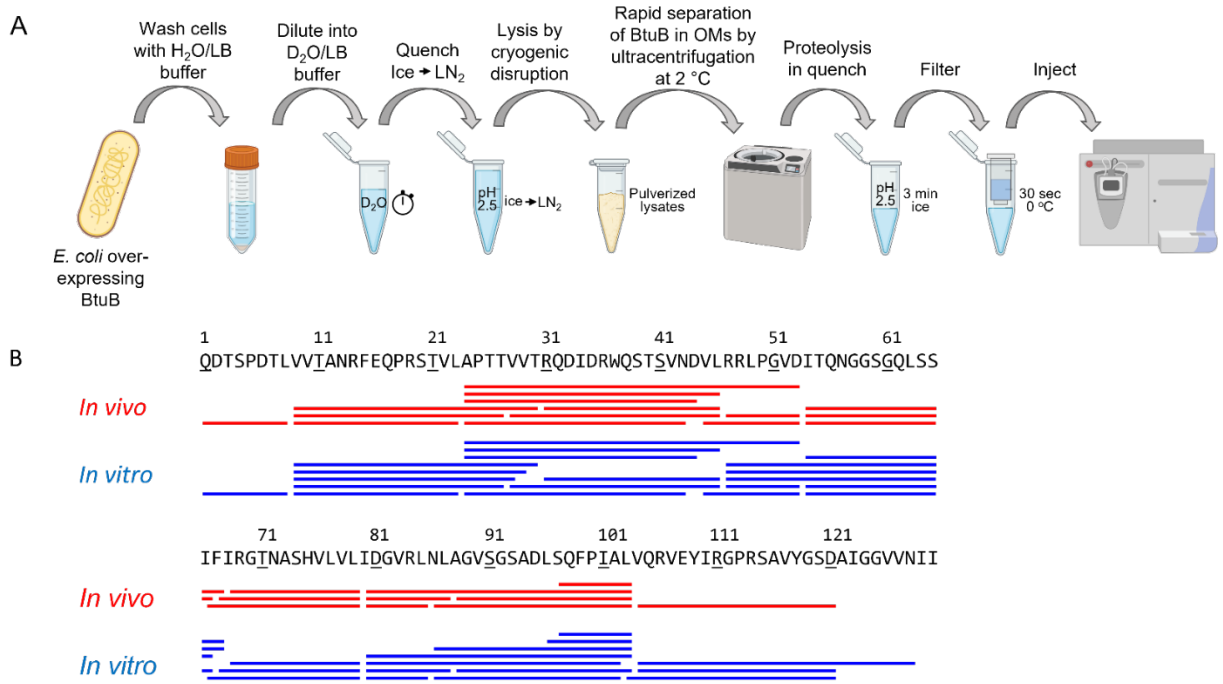

Figure 3.1: Experimental workflow and sequence coverage for in vivo HDX-MS on BtuB. (A) In the *in vivo* HDX-MS protocol, living *E. coli* cells overexpressing BtuB are diluted in a D_2O buffer supplemented with a carbon source. After quenching, cells are lysed using cryogenic disruption, and OMs containing BtuB are separated by ultracentrifugation at pH 2.5, 2 °C. Figure created with BioRender. (B) *In vivo* measurements observe 25 peptides (red) with 93% coverage of BtuBp, while previous *in vitro* measurements observe 35 (blue) with 98% coverage of BtuBp.[15]

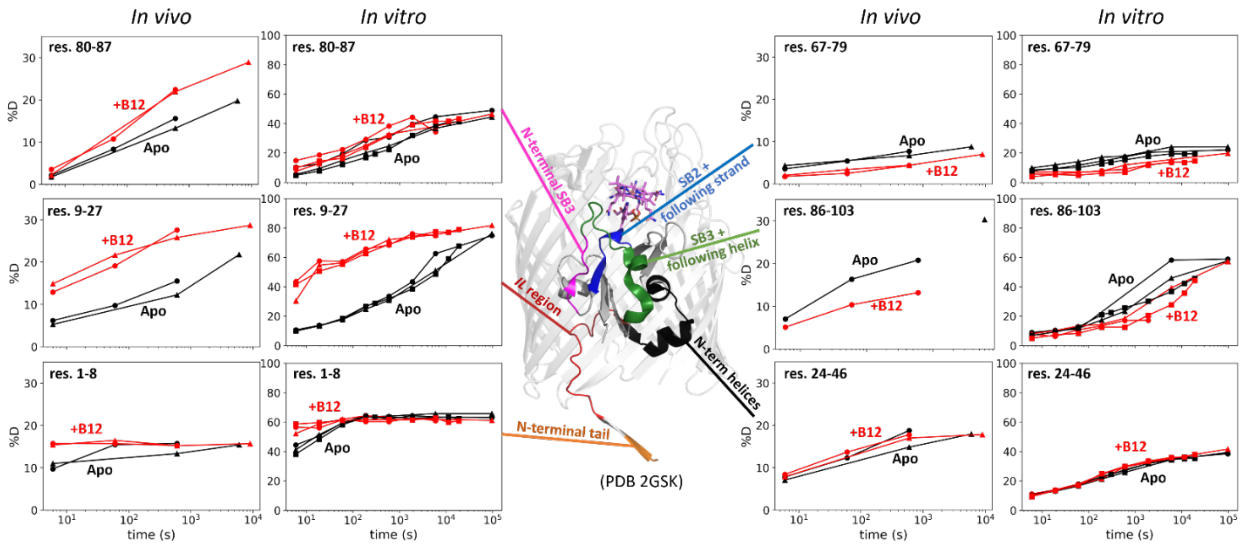

Figure 3.2: Effects of B12 binding on BtuBp's HDX measured in vivo and in vitro.
Sides: Uptake plots showing comparisons between biologically duplicated *in vivo* data (circles and triangles) and previously reported triplicated *in vitro* data (circles, triangles, and squares).[15] Center: Each peptide is associated with a colored region on the BtuB structure. Incomplete uptake curves are shown in cases where not every time point within a biological replicate was confidently measured.

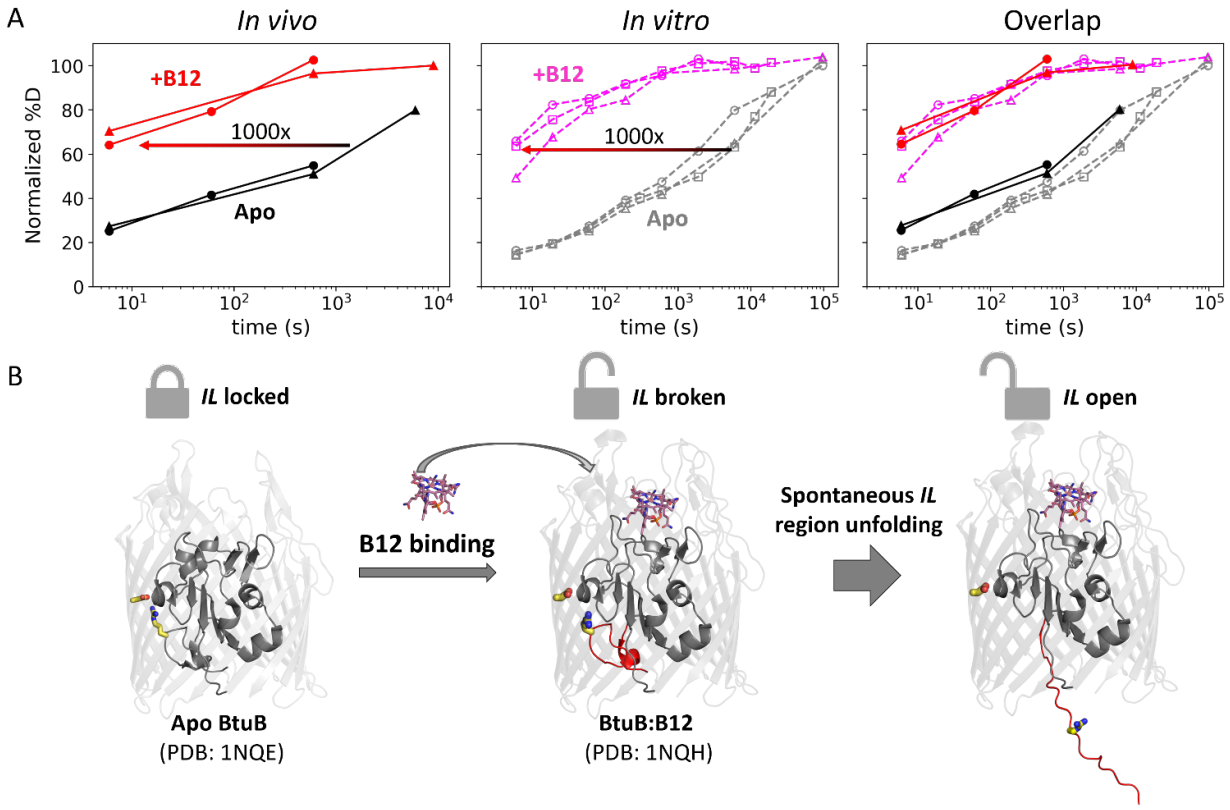

Figure 3.3: B12 binding induces unfolding of the Ionic Lock region of BtuBp in vivo similarly to in vitro.
(A) Uptake plots for Peptide$_{9\text{-}23}$ for (Left) biologically duplicated *in vivo* data (solid lines; circles and triangles) (Apo: black; B12-bound state: red) and (Middle) previously reported triplicated *in vitro* data (broken lines; circles, triangles, and squares) (Apo: grey; B12-bound state: magenta).[15] Deuteration levels are normalized to account for back exchange levels. Right: overlapped uptake curves of *in vivo* and *in vitro* uptake curves. (B) Model of BtuBp's conformational change upon B12 binding. The left and right states are observed in the HDX-MS as apo and B12-bound states, respectively. The structure on the right is modeled per HDX-MS data. The middle plot is a crystal structure of BtuB in a B12-bound state and is not observed in HDX-MS. Sidechains for the *Ionic Lock* residues are shown as yellow sticks. B12 is shown as magenta sticks. The *Ionic Lock* region is colored red. Figure adapted from Zmyslowski *et al*., 2022.[15]

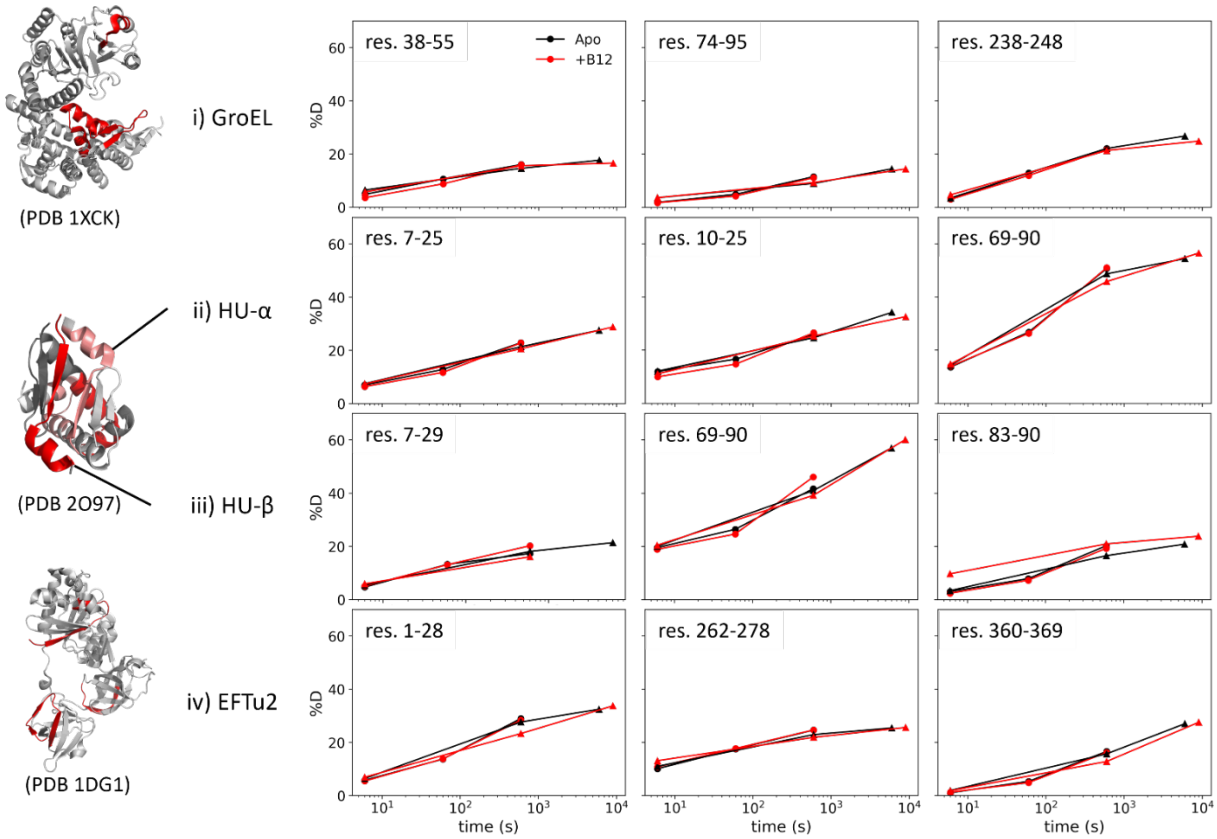

Figure 3.4: HDX of endogenous E. coli proteins measured in experiments targeting BtuB. Structures are shown for the following proteins, with respective numbers of assigned peptides and sequence coverage: i) GroEL: 21 peptides, 46.9%; ii) Histone-like DNA binding protein α chain (HU-α): 12 peptides, 67.8%; iii) HU-β: 10 peptides, 88.9%; iv) Elongation factor Tu 2 (EF-Tu2): 13 peptides, 41.4%. Uptake plots show biologically duplicated data (circles and triangles) in the absence (black) and presence (red) of B12. The locations of the peptides shown are highlighted in red (except for HU-α peptides which are in salmon) in the corresponding structures.

3.1.11 Supplementary figures

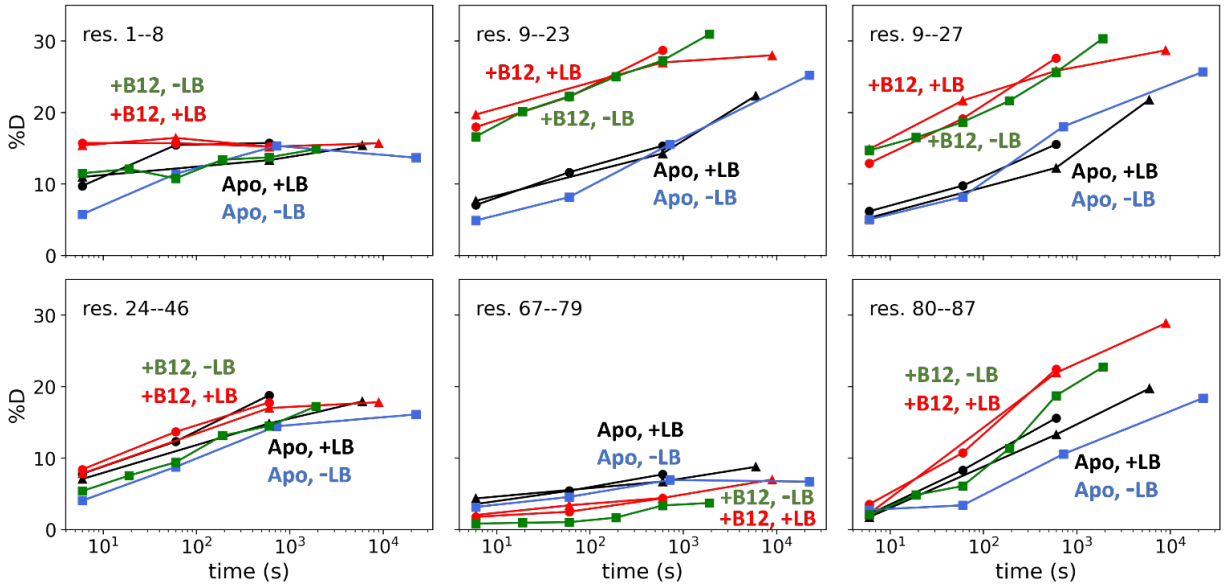

Figure 3.5: BtuBp's HDX is independent of the choice of carbon source within sampled label times. Uptake plots show data in the apo and B12-bound states of BtuBp labeled in D_2O buffer supplemented with (biological duplicates; circles and triangles) and without (squares) LB media.

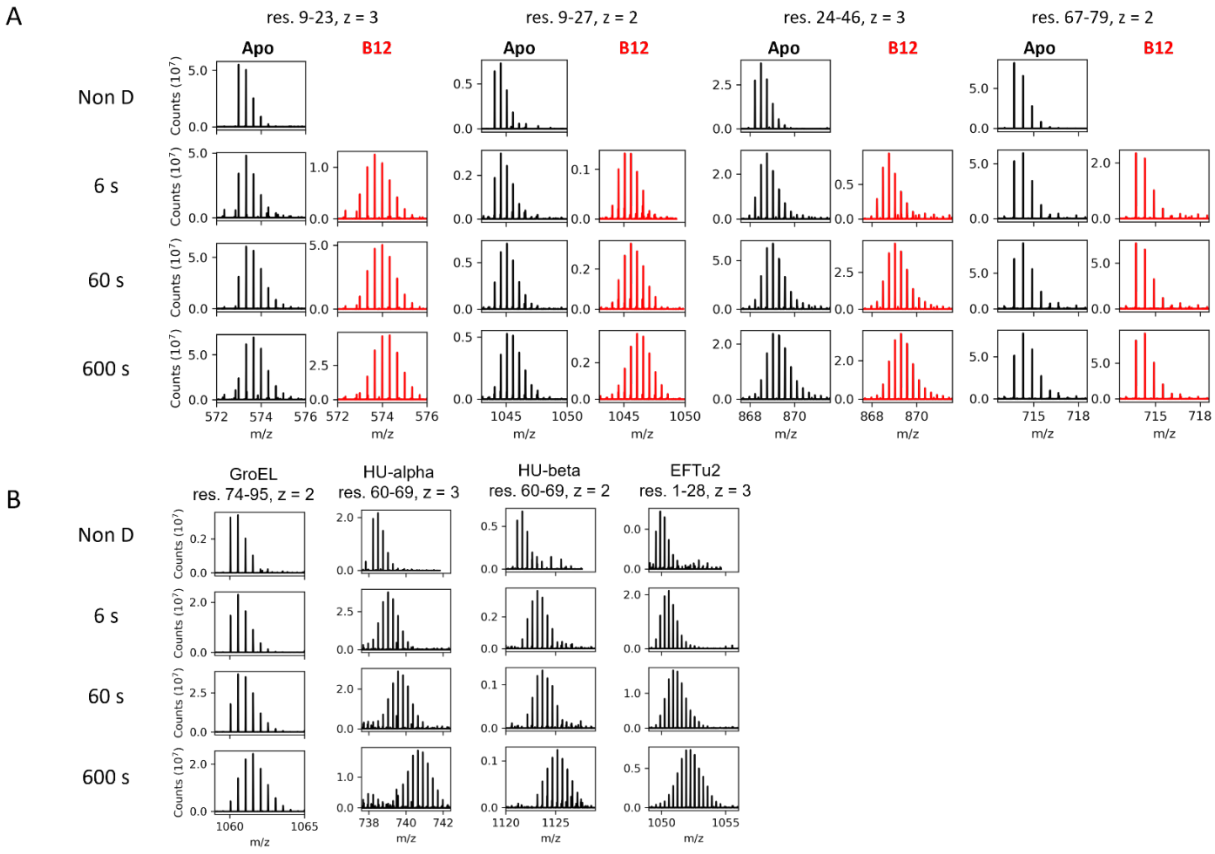

Figure 3.6: Mass spectra of a set of representative peptides.
Mass spectra show peptides that are undeuterated and deuterated for 6 s, 60 s, and 600 s, for (A) BtuBp (black: apo; red: B12-bound state) and (B) several endogenous proteins whose HDX was measured in the same experiments in the absence of B12.

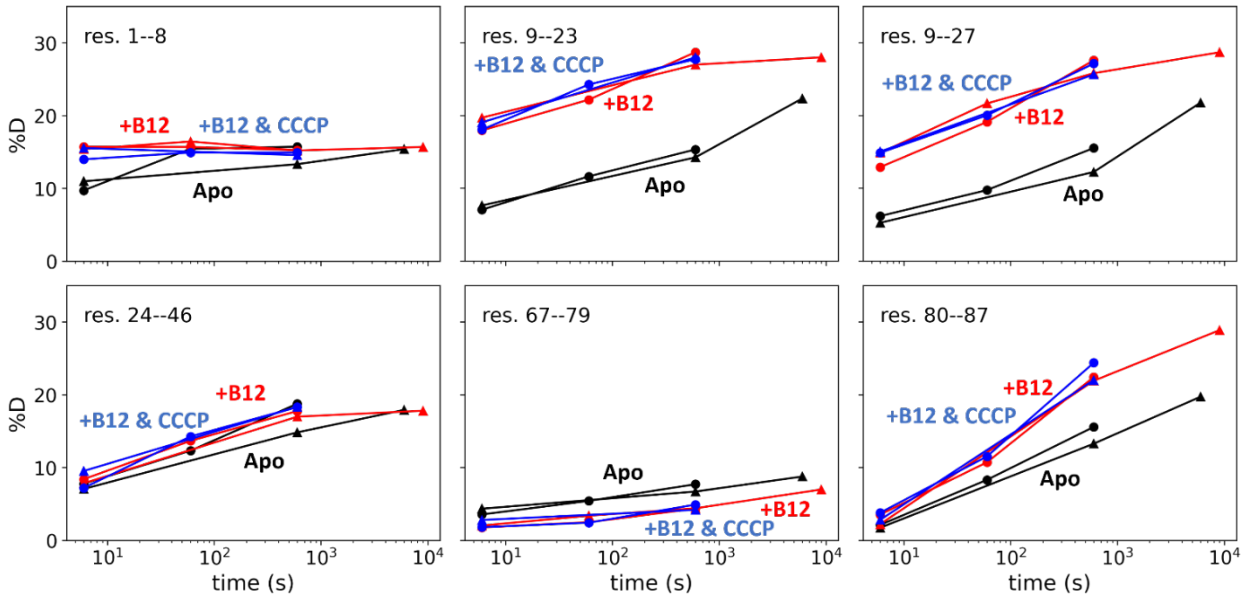

Figure 3.7: B12 binding-induced dynamics in BtuBp are insensitive to dissipation of the proton motive force via CCCP.
Uptake plots show biologically duplicated data (circles and triangles) for BtuBp in the apo state (black), B12-bound state (red), and in the presence of B12 and CCCP (blue).

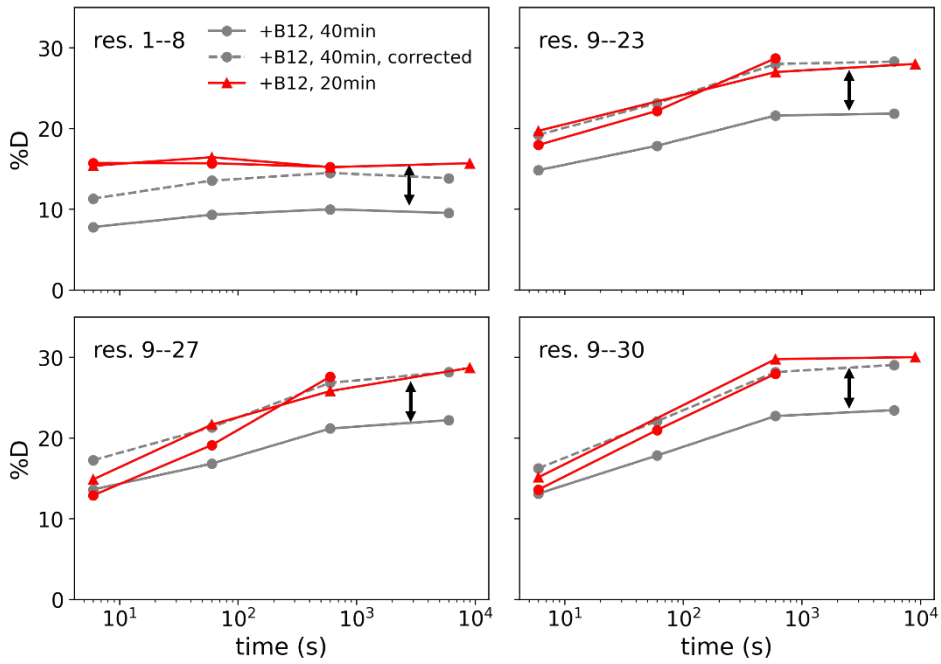

Figure 3.8: HDX back exchange occurs primarily during the post-quench sample work-up. An increase in ultracentrifugation time from 20 min (red. Biological duplicates shown as circles and triangles) to 40 min (grey circles) results in elevated back exchange levels (arrows) as indicated by a decrease in the maximum deuteration level ($\%D_{max}$) when a peptide is fully deuterated (indicated by the arrows). Grey dashed lines show expected k_{chem}-corrected deuteration levels if the 40-min centrifugation were only 20 min. Only peptides that become fully deuterated are shown (i.e., BtuBp's amino terminus in the B12-bound state).

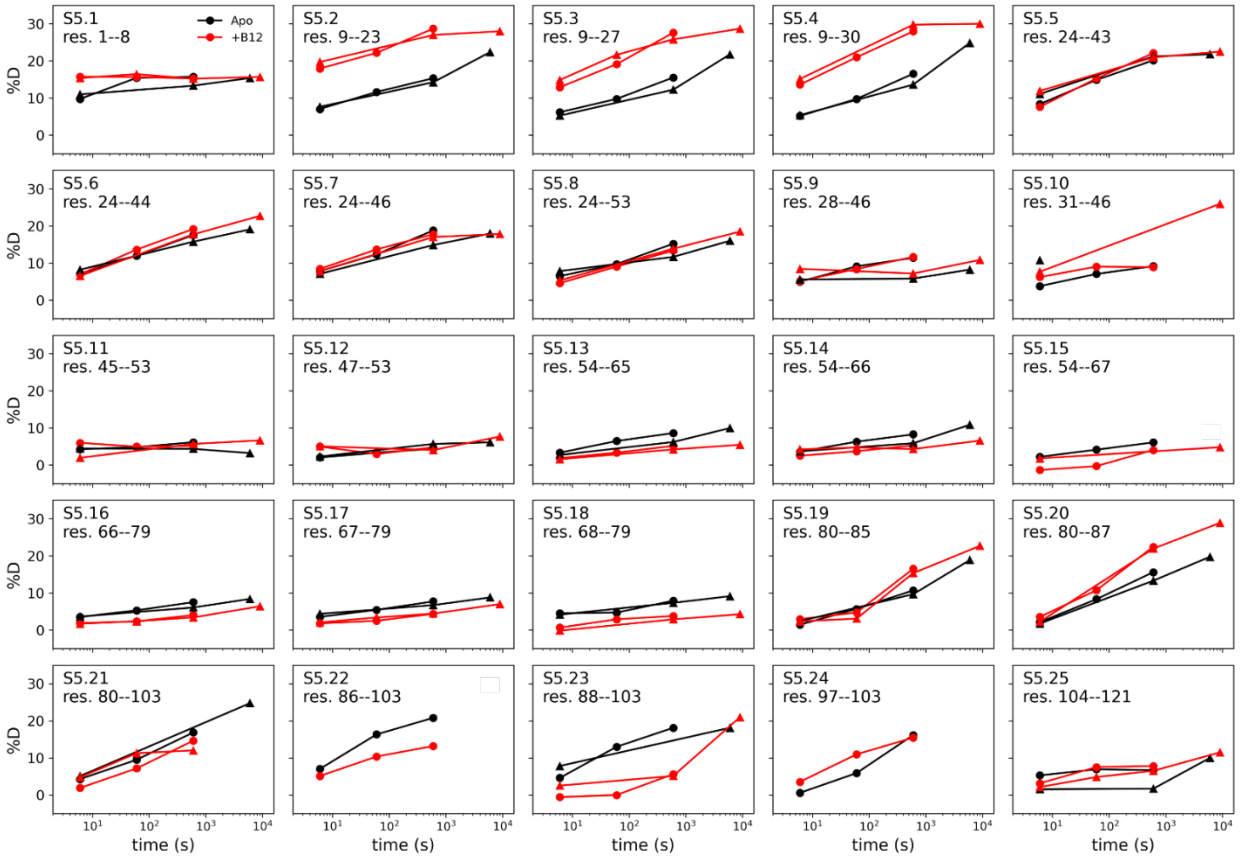

Figure 3.9: Uptake curves for all available BtuBp peptides.
Two biological replicates are shown as circles and triangles. Apo: black; B12-bound state: red. Incomplete uptake curves are shown in cases where not every time point within a biological replicate was confidently measured.

Table 2: HDX summary table.

Data Set	Apo	+B12	+B12, +CCCP
HDX reaction details	50 mM NaPi, 150 mM NaCl, 1x LB, 0.8% DMSO, pD_{read} = 6.8, 22 °C	50 mM NaPi, 150 mM NaCl, 1x LB, 0.8% DMSO, 16 µM B12, and 1.6 mM $CaCl_2$, pD_{read} = 6.8, 22 °C	50 mM NaPi, 150 mM NaCl, 1x LB, 0.8% DMSO, 5 µM CCCP, 16 µM B12, and 1.6 mM $CaCl_2$, pD_{read} = 6.8, 22 °C
HDX time course (sec)	6, 60, 600, 6000	6, 60, 600, 9000	6, 60, 600
HDX control samples	t_{HDX} = 9000 s in the presence of B12 serves as the maximally labeled control for the amino-terminus. In-exchange control: HDX with 6 s labeling time on ice at pD_{read} = 6.8	Same as Apo	Same as Apo
Back-exchange	Not measured	71.1% / 0.8% (mean / standard deviation) calculated from t_{HDX} = 9000 s of peptides covering the *IL* region	Not measured
# of Peptides	25	25	25
Exchangeable sequence coverage	78% of BtuBp	78% of BtuBp	78% of BtuBp
Average peptide length / Redundancy	15.4 / 0.6	15.4 / 0.6	15.4 / 0.6
Replicates	2 (biological)	2 (biological)	2 (biological)
Repeatability (mean / standard deviation)	0.26 Da / 0.28 Da (1.8% / 1.6%) (calculated from Δ#D (Δ%D) of the two replicates for all peptides at t_{HDX} = 6 s and 600 s)	0.20 Da / 0.20 Da (1.4% / 1.1%) (calculated from Δ#D (Δ%D) of the two replicates for all peptides at t_{HDX} = 6 s and 600 s)	0.23 Da / 0.35 Da (1.7% / 2.7%) (calculated from Δ#D (Δ%D) of the two replicates for all peptides at t_{HDX} = 6 s and 600 s)

Table 3: Top 20 E. coli K12 proteome search hits ranked by the number of identified peptides. 346/4438 of sequences are found.

No.	Description	Uniprot Entry	Coverage (%)	#Peptides	MW (kDa)
1	Vitamin B12 transporter BtuB	P06129	51.63 (whole protein) / 92% (BtuBp)	30 (whole protein) / 25 (BtuBp)	68
2	Chaperonin GroEL	P0A6F5	50.91	25	57
3	DNA-binding protein HU-α	P0ACF0	80.00	24	10
4	Elongation factor Tu 2	P0CE48	48.48	21	43
5	Probable ATP-dependent helicase lhr	P30015	17.17	20	169
6	Elongation factor Tu 1	P0CE47	48.48	19	43
7	Protein RhsD	P16919	18.02	17	160
8	Uncharacterized protein YeeJ	P76347	10.35	16	248
9	Protein RhsB	P16917	16.37	15	159
10	Respiratory nitrate reductase 1 α chain	P09152	15.32	14	140
11	DNA-binding protein HU-β	P0ACF4	92.22	13	9
12	Uncharacterized protein YhdP	P46474	15.96	13	139
13	Protein RhsC	P16918	13.24	13	158
14	Protein RhsA	P16916	13.22	13	156
15	Intermembrane transport protein YebT	P76272	15.62	11	95
16	Cytosol aminopeptidase	P68767	24.45	10	55
17	RecBCD enzyme subunit RecC	P07648	14.17	10	129
18	DNA translocase FtsK	P46889	11.66	10	147
19	NADP-dependent malic enzyme	P76558	16.60	9	82
20	50S ribosomal protein L24	P60624	65.38	8	11

3.1.12 References

(1) Englander, S. W. Hydrogen Exchange and Mass Spectrometry: A Historical Perspective. *J. Am. Soc. Mass Spectrom.* **2006**, *17* (11), 1481–1489.

(2) Mayne, L.; Kan, Z.-Y.; Sevugan Chetty, P.; Ricciuti, A.; Walters, B. T.; Englander, S. W. Many Overlapping Peptides for Protein Hydrogen Exchange Experiments by the Fragment Separation-Mass Spectrometry Method. *J. Am. Soc. Mass Spectrom.* **2011**, *22* (11), s13361-011-0235–4.

(3) James, E. I.; Murphree, T. A.; Vorauer, C.; Engen, J. R.; Guttman, M. Advances in Hydrogen/Deuterium Exchange Mass Spectrometry and the Pursuit of Challenging Biological Systems. *Chem. Rev.* **2021**, acs.chemrev.1c00279.

(4) Del Mar, C.; Greenbaum, E. A.; Mayne, L.; Englander, S. W.; Woods, V. L. Structure and Properties of -Synuclein and Other Amyloids Determined at the Amino Acid Level. *Proc. Natl. Acad. Sci.* **2005**, *102* (43), 15477–15482.

(5) Hebling, C. M.; Morgan, C. R.; Stafford, D. W.; Jorgenson, J. W.; Rand, K. D.; Engen, J. R. Conformational Analysis of Membrane Proteins in Phospholipid Bilayer Nanodiscs by Hydrogen Exchange Mass Spectrometry. *Anal. Chem.* **2010**, *82* (13), 5415–5419.

(6) Costello, S. M.; Shoemaker, S. R.; Hobbs, H. T.; Nguyen, A. W.; Hsieh, C.-L.; Maynard, J. A.; McLellan, J. S.; Pak, J. E.; Marqusee, S. The SARS-CoV-2 Spike Reversibly Samples an Open-Trimer Conformation Exposing Novel Epitopes. *Nat. Struct. Mol. Biol.* **2022**.

(7) Martens, C.; Politis, A. A Glimpse into the Molecular Mechanism of Integral Membrane Proteins through Hydrogen–Deuterium Exchange Mass Spectrometry. *Protein Sci.* **2020**, *29* (6), 1285–1301.

(8) Masson, G. R.; Burke, J. E.; Ahn, N. G.; Anand, G. S.; Borchers, C.; Brier, S.; Bou-Assaf, G. M.; Engen, J. R.; Englander, S. W.; Faber, J.; Garlish, R.; Griffin, P. R.; Gross, M. L.; Guttman, M.; Hamuro, Y.; Heck, A. J. R.; Houde, D.; Iacob, R. E.; Jorgensen, T. J. D.; Kaltashov, I. A.; Klinman, J. P.; Konermann, L.; Man, P.; Mayne, L.; Pascal, B. D.; Reichmann, D.; Skehel, M.; Snijder, J.; Strutzenberg, T. S.; Underbakke, E. S.; Wagner, C.; Wales, T. E.; Walters, B. T.; Weis, D. D.; Wilson, D. J.; Wintrode, P. L.; Zhang, Z.; Zheng, J.; Schriemer, D. C.; Rand, K. D. Recommendations for Performing, Interpreting and Reporting Hydrogen Deuterium Exchange Mass Spectrometry (HDX-MS) Experiments. *Nat. Methods* **2019**, *16* (7), 595–602.

(9) Noinaj, N.; Guillier, M.; Barnard, T. J.; Buchanan, S. K. TonB-Dependent Transporters: Regulation, Structure, and Function. *Annu. Rev. Microbiol.* **2010**, *64*, 43–60.

(10) Chimento, D. P.; Mohanty, A. K.; Kadner, R. J.; Wiener, M. C. Substrate-Induced Transmembrane Signaling in the Cobalamin Transporter BtuB. *Nat. Struct. Mol. Biol.* **2003**, *10* (5), 394–401.

(11) Shultis, D. D.; Purdy, M. D.; Banchs, C. N.; Wiener, M. C. Outer Membrane Active Transport: Structure of the BtuB:TonB Complex. *Science* **2006**, *312* (5778), 1396–1399.

(12) Celia, H.; Noinaj, N.; Buchanan, S. K. Structure and Stoichiometry of the Ton Molecular Motor. *Int. J. Mol. Sci.* **2020**, *21* (2), 375.

(13) Nyenhuis, D. A.; Nilaweera, T. D.; Cafiso, D. S. Native Cell Environment Constrains Loop Structure in the Escherichia Coli Cobalamin Transporter BtuB. *Biophys. J.* **2020**, *119* (8), 1550–1557.

(14) Nilaweera, T. D.; Nyenhuis, D. A.; Cafiso, D. S. Structural Intermediates Observed Only in Intact Escherichia Coli Indicate a Mechanism for TonB-Dependent Transport. *eLife* **2021**, *10*, e68548.

(15) Zmyslowski, A. M.; Baxa, M. C.; Gagnon, I. A.; Sosnick, T. R. HDX-MS Performed on BtuB in E. Coli Outer Membranes Delineates the Luminal Domain's Allostery and Unfolding upon B12 and TonB Binding. *Proc. Natl. Acad. Sci.* **2022**, *119* (20), e2119436119.

(16) Balusek, C.; Gumbart, J. C. Role of the Native Outer-Membrane Environment on the Transporter BtuB. *Biophys. J.* **2016**, *111* (7), 1409–1417.

(17) Jordan, L. D.; Zhou, Y.; Smallwood, C. R.; Lill, Y.; Ritchie, K.; Yip, W. T.; Newton, S. M.; Klebba, P. E. Energy-Dependent Motion of TonB in the Gram-Negative Bacterial Inner Membrane. *Proc. Natl. Acad. Sci. U. S. A.* **2013**, *110* (28), 11553–11558..

(18) Gresock, M. G.; Kastead, K. A.; Postle, K. From Homodimer to Heterodimer and Back: Elucidating the TonB Energy Transduction Cycle. *J. Bacteriol.* **2015**, *197* (21), 3433–3445.

(19) Nilaweera, T. D.; Nyenhuis, D. A.; Nakamoto, R. K.; Cafiso, D. S. Disulfide Chaperone Knockouts Enable In Vivo Double Spin Labeling of an Outer Membrane Transporter. *Biophys. J.* **2019**, *117* (8), 1476–1484.

(20) Lukasik, S. M.; Ho, K. W. D.; Cafiso, D. S. Molecular Basis for Substrate-Dependent Transmembrane Signaling in an Outer-Membrane Transporter. *J. Mol. Biol.* **2007**, *370* (5), 807–811.

(21) Kadner, R. J.; Heller, K.J. Mutual inhibition of cobalamin and siderophore uptake systems suggests their competition for TonB function. *J Bacteriol.* **1995**, 177(17):4829-4835.

(22) Higgs, P. I.; Larsen, R. A.; Postle, K. Quantification of Known Components of the Escherichia Coli TonB Energy Transduction System: TonB, ExbB, ExbD and FepA. *Mol. Microbiol.* **2002**, *44* (1), 271–281.

(23) Bradbeer, C. The Proton Motive Force Drives the Outer Membrane Transport of Cobalamin in Escherichia Coli. *J. Bacteriol.* **1993**, *175* (10), 3146–3150.

(24) Krewulak, K. D.; Vogel, H. J. TonB or not TonB: is that the question?. *Biochem Cell Biol.* **2011**, 89(2):87-97.

(25) Vigenschow, H., Przuntek, H., and Lawaczeck, R. On the exchange of H2O/D2O molecules across membranes of erythrocyte ghosts from patients with Huntington's disease and from normal individuals. *J Neurol*. **1984**, 231, 54-55

(26) Kuwahara, M.; Verkman, A. S. Direct Fluorescence Measurement of Diffusional Water Permeability in the Vasopressin-Sensitive Kidney Collecting Tubule. *Biophys. J.* **1988**, *54* (4), 587–593.

(27) Lawaczeck, R. Water Permeability through Biological Membranes by Isotopic Effects of Fluorescence and Light Scattering. *Biophys. J.* **1984**, *45 (3),* 491–494.

(28) Yao, X.; Dürr, U. H. N.; Gattin, Z.; Laukat, Y.; Narayanan, R. L.; Brückner, A.-K.; Meisinger, C.; Lange, A.; Becker, S.; Zweckstetter, M. NMR-Based Detection of Hydrogen/Deuterium Exchange in Liposome-Embedded Membrane Proteins. *PLoS ONE* **2014**, *9* (11), e112374.

(29) Schink, S. J.; Biselli, E.; Ammar, C.; Gerland, U. Death Rate of E. Coli during Starvation Is Set by Maintenance Cost and Biomass Recycling. *Cell Syst.* **2019**, *9* (1), 64-73.e3.

(30) Fang, M.; Wang, Z.; Cupp-Sutton, K. A.; Welborn, T.; Smith, K.; Wu, S. High-Throughput Hydrogen Deuterium Exchange Mass Spectrometry (HDX-MS) Coupled with Subzero-Temperature Ultrahigh Pressure Liquid Chromatography (UPLC) Separation for Complex Sample Analysis. *Anal. Chim. Acta* **2021**, *1143*, 65–72.

(31) Anderson, K. W.; Hudgens, J. W. Chromatography at −30 °C for Reduced Back-Exchange, Reduced Carryover, and Improved Dynamic Range for Hydrogen–Deuterium Exchange Mass Spectrometry. *J. Am. Soc. Mass Spectrom.* **2022**.

(32) Cooper G. M. The Cell: A Molecular Approach. 2nd ed. Cell Membranes. Sunderland, MA: Sinauer Associates, **2000**.

3.2 HDX-MS conducted on yeast Pab1 in live bacteria

3.2.1 Summary

This chapter describes the preliminary data for *in vivo* HDX-MS conducted on poly(A)-binding protein, Pab1, a stress granule marker that forms condensates upon heat shock. HDX measured in live *E. coli* cells expressing Pab1 highlights a more protected second RNA recognition motif (RRM2) than purified Pab1 in the soluble state, pointing to interactions in the cellular environment that are lost during purification. The success of measuring HDX in BtuB, Pab1, and endogenous *E. coli* proteins suggests that the ability to measure HDX *in vivo* is generalizable which opens up a wide range of HDX studies on proteins in their native context.

3.2.2 Motivation

The success of measuring HDX in BtuB and other endogenous *E. coli* proteins[1] motivated us to extend the application of in vivo HDX to other biological systems in which a native cellular environment may promote different functions than minimal buffers. Pab1 is a stress granule marker that forms condensates upon heat shock. The interactions of Pab1 with endogenous RNA and proteins may confer dynamics and therefore condensation mechanisms that are distinct from isolated Pab1. Previous studies from our lab found that purified Pab1 phase separates through a sequential activation mechanism driven by local unfolding of RRMs.[2] It was of interest to investigate how a crowded cellular environment alters the dynamics of Pab1 and whether the same phase separation mechanism observed *in vitro* is preserved *in vivo*.

3.2.3 Materials and methods

Construct design: The construct of Pab1 used for in vivo HDX was initially designed for the application of the low-pH purification tag, which is a designed peptide-based affinity tag that can purify proteins at extreme acidic conditions, including the HDX quench conditions at pH 2.5. Therefore, other than the His-tag at the N-terminus, the Pab1 construct includes residues 1-10 from DesG at the C-terminus that was connected to Pab1 with two GGS repeats. The residues 1-10 from DesG served as the affinity tag. However, it was later discovered that the low-pH purification tag does not display a high enough affinity to the binding partner. Nevertheless, the 16 additional residues at the C-terminus of Pab1 was expected to minimally affect the dynamics and functions of Pab1. Additionally, Pab1 was expressed in *E. coli* rather than yeast to allow for direct comparison between *in vivo* HDX and the available *in vitro* HDX data.

Pab1 expression: Pab1 construct was transformed into BL21 *E. coli* cells. 0.5 L of LB culture was inoculated with 5 mL of overnight starting culture and then cells were grown at 37 °C. When the optical density reached 0.6, cells were cooled down at room temperature for 30 min, and then induced with 0.2 mM IPTG for 4 h at 30 °C.

HDX labeling and cell lysis: 15 mL of cells after induction was washed twice with 15 mL of H_2O buffer containing 20 mM NaPi, 100 mM NaCl, 2% glucose, pH 7.4. After the washes, cells were resuspended with 450 uL H_2O buffer. Final cells are ~25-30x concentrated compared to cell density

after induction.

HDX in a solution of 90% deuterium (D) content was initiated by diluting 6 µL of concentrated cells pre-chilled on ice in an H_2O buffer into 54 uL of ice-chilled D_2O buffer containing 20 mM NaPi, 100 mM NaCl, 2% glucose, pD_{read} 7.0. HDX reactions were all carried out on ice. HDX was quenched at 10 s, 40 s, and 85 s by directly flash freezing in LN2, and stored in -80 °C until lysis. Two HDX reactions were carried out at room temperature for 20 h 30 min and 20 h 40 min as highly labeled controls. Note that the pD_{read} used for in vivo HDX was one unit higher than in vitro HDX on Pab1, which was performed at pD_{read} 6.0. This was because protons do not efficiently permeate cell membrane and therefore the labeling pD needs to match the cytosolic pH, which is approximately 7.4. The *in vivo* HDX data shown in the Chapter 3.2.4 HDX results and discussion are corrected for the pH-dependent k_{chem} effect by displaying the corrected time points, i.e., 100 s, 400 s, and 850 s.

Quenched cells were lysed by cryo-milling for 10 cycles. Each cycle was 1.5 min long at 30 Hz frequency. Lysed cells were stored in -80 °C until LC-MS analysis.

LC-MS: Pulverized lysates were resolubilized by adding 400 uL of ice-chilled quench buffer containing 600 mM Glycine at pH 2.5 and rigorous pipetting. Lysate was clarified by filtering through a spin filter at 12 k rpm for 30 s at 2 °C. The insoluble fraction was resolubilized by adding 100 uL of ice-chilled quench buffer containing 8 M urea. Protein precipitates were removed by filtering through a spin filter at 12 k rpm for 30 s at 2 °C. Additional 100 uL of quench buffer containing no urea was added to the filtrate to reach a final urea concentration of 4 M. The total 200 uL of sample was immediately subject to LC-MS analysis. LC-MS and HDX data analysis all

followed the same protocol as described in Chapter 2.1.6 Materials and Methods.

3.2.4 HDX results and discussion

3.2.4.1 Peptide assignments for Pab1 from in vivo HDX

Pab1 was overexpressed and the major protein species in the lysate (Figure 3.10). LC-MS analysis of Pab1 labeled in live *E. coli* cells yielded high MS signal-to-noise ratios and comparable peptide assignment results as those obtained from in vitro HDX-MS studies on Pab1. Specifically, we obtained a TIC of 2E9 for each LC-MS experiment. When searching against 10 protein sequences, including proteins that had been subjected to the same LC-MS and common protein contaminants, we obtained a sequence coverage of 99.02% for Pab1 with a total of 306 peptides and 1371 spectra. When searching against 4438 sequences of E. coli strain K12 proteome obtained from Uniprot, including Pab1 sequence, we obtained a sequence coverage of 92.5% for Pab1 with a total of 163 peptides and 958 spectra.

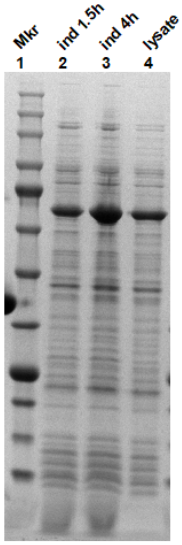

Figure 3.10: SDS-PAGE gel showing samples used for in vivo HDX-MS of Pab1.
Lane 1: protein ladder; lane 2-3: E. coli induced with IPTG for 1.5 h and 4 h, respectively; lane 4: E. coli lysate after 4 h of induction.

3.2.4.2 Soluble Pab1 had a less dynamic RRM2 in live cells than purified soluble Pab1

HDX patterns for RRM1, RRM3, and RRM4 for Pab1 labeled in live *E. coli* highly resembled the HDX for purified Pab1 (Figure 3.11 & Figure 3.12). Interestingly, all available peptides covering RRM2 for Pab1 labeled in live cells exhibited no deuteration at the longest effective labeling time compared to ~50% deuteration levels (Figure 3.11 & Figure 3.12). The highly reduced deuteration levels for the *in vivo* samples suggest that Pab1 in a native *E. coli* cellular environment displayed a less dynamic RRM2 in the soluble state than purified Pab1. The reduced dynamics of RRM2 *in vivo* may indicate binding between Pab1 and other biomolecules in *E. coli* through the RRM2 interface, especially RNAs as Pab1 is an RNA-binding protein. Further investigation is required

to identify the nature of the reduced dynamics of RRM2 and whether such phenomenon influences Pab1 phase separation in a native cellular environment.

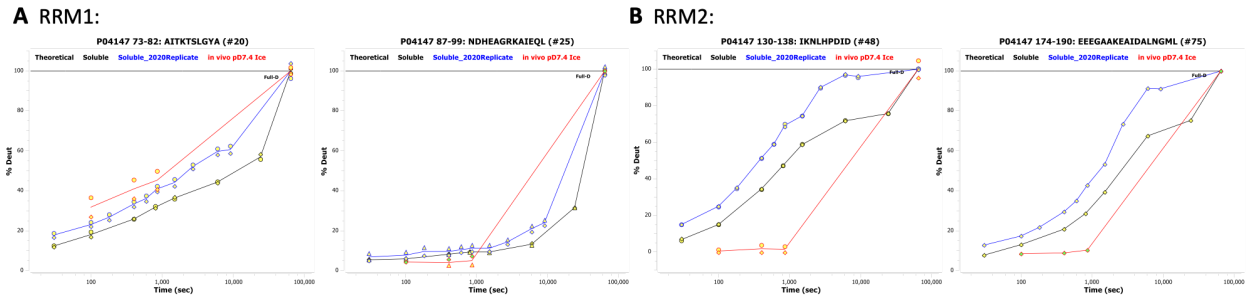

Figure 3.11: Uptake plots for representative peptides at RRM1 (A) and RRM2 (B) comparing Pab1 HDX in vivo and in purified proteins.
Black and blue: two replicates of HDX on purified Pab1 in the soluble state. Red: HDX on Pab1 in live *E. coli*.

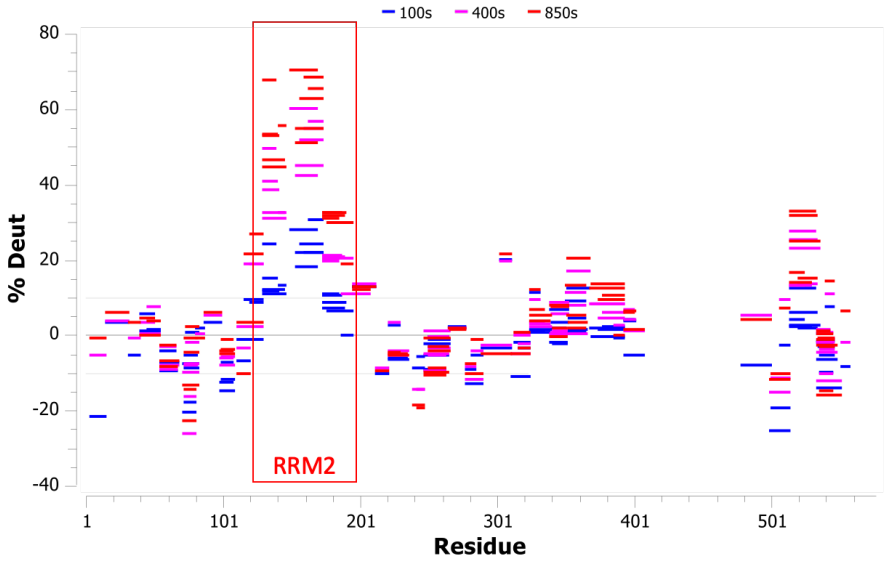

Figure 3.12: Woods plot showing the %D differences for Pab1 labeled in vivo and as purified proteins.

Each bar represents a peptide at the corresponding residue numbers. The plot shows three time points – 100 s, 400 s, 850 s. Positive %D represents higher deuteration levels in purified Pab1 than Pab1 labeled in live E. coli. The red boxed region indicates peptides covering the sequences for RRM2.

In addition to reduced dynamics observed at RRM2, we also observed different HDX patterns for the C-terminal domain of Pab1. Although purified Pab1 exhibited unimodal mass spectra, indicating the presence of a homogeneous population in which Pab1 molecules display similar dynamics, Pab1 *in vivo* exhibited bimodal mass spectra for peptides covering the C-terminus (Figure 3.13). The presence of the bimodal spectra suggests that Pab1 in live cells likely displayed two conformations at the C-terminus with distinct stability, and the two populations are slowly interconverting at a time constant longer than the HDX labeling times. The nature of the observed bimodality warrants further investigation.

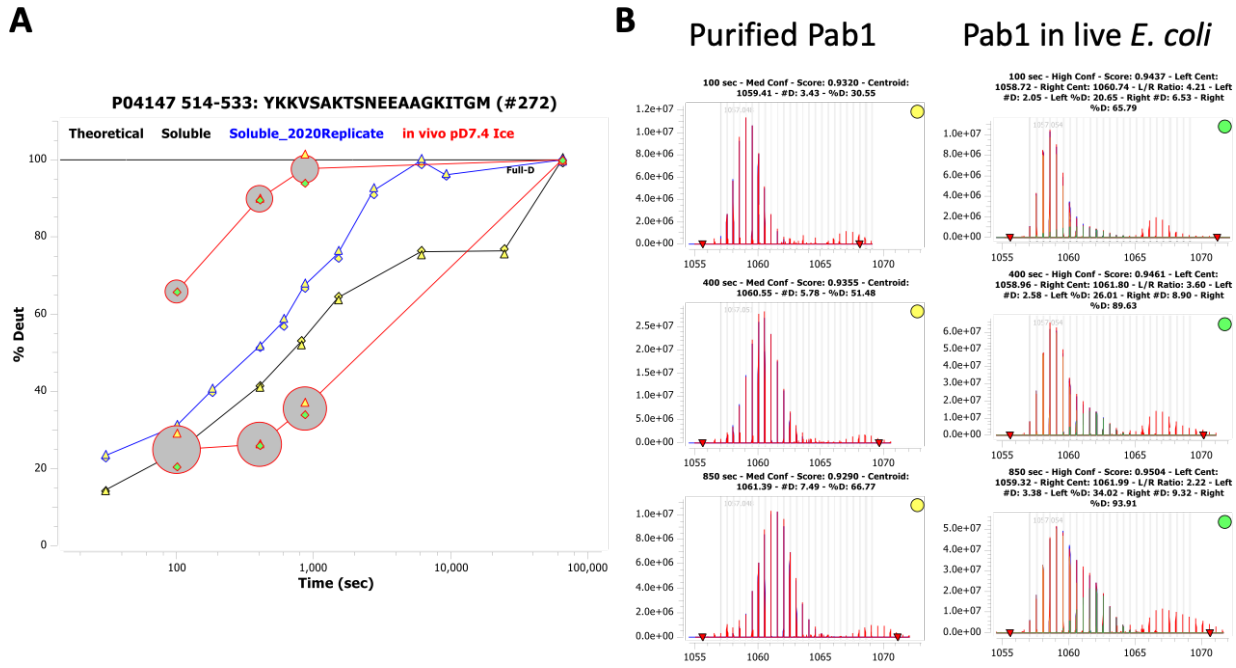

Figure 3.13: Pab1 in live *E. coli* exhibits conformational heterogeneity at the C-terminus.
(A) Uptake plots of a representative peptide covering Pab1's C-terminal domain. Black and blue: two replicates of HDX on purified Pab1 in the soluble state. Red: HDX on Pab1 in live *E. coli*. Bubbles show bimodality. The sizes of the bubble represent relative fractions of the two populations. (B) Raw mass spectra for purified Pab1 (red spectra) and Pab1 labeled in live cells (spectra colored in orange and green, indicating the two populations) over labeling time.

4 PUSHING THE TECHNIQUE OF HDX-MS TO MEMBRANE PROTEINS IN NANODISCS AND LIPOSOMES

4.1 Advancing the technique of HDX-MS on membrane proteins in a lipid bilayer

4.1.1 Motivations

To date, the majority of HDX-MS studies performed on membrane proteins are for detergent-solubilized systems while a small fraction of the studies is on membrane proteins embedded in nanodiscs. However, questions remain as to the thermodynamics of a membrane protein in a micelle versus in a lipid bilayer. That is, does a membrane protein solubilized in detergent micelles exhibit the same dynamics as in a lipid bilayer?

Detergents, although most of the time serve as the first step of membrane protein purification and reconstitution and are relatively easy to use, present questions as their intrinsic plasticity allowing them to form a micelle with flexible shapes when solubilizing a membrane protein. The flexibility of detergent molecules permits them to be inserted at many places surrounding the hydrophobic surface of a membrane protein. As a result, even though detergents provide solubilization of the membrane protein, they do not provide the native environment that would be provided by a lipid bilayer with a higher degree of rigidity. Other membrane environments, such as membrane curvature and tension, are also lost when using a micelle.

Nanodiscs have been widely used to investigate the mechanisms of membrane proteins in a more native membrane mimetic. Nanodiscs provide a lipid bilayer and membrane tension, which results in a more native-like environment. However, the mechanism through which HX occurs for

a membrane protein placed in nanodiscs remains to be investigated. Exchange for an amide proton can only occur when it is not participating in hydrogen bonds, meaning that a residue has to unfold first before it can exchange its amide proton with solvent protons or deuterons. However, what does an unfolded polypeptide chain look like for membrane proteins? A folded transmembrane helix is stabilized in a lipid bilayer through interactions between the side chains and the alkyl chains from the lipids. Once the transmembrane helix unfolds, the polypeptide backbone is exposed and the stabilization between the side chains and the lipids is lost. Therefore, it is highly unfavorable for an unfolded helix to stay in the membrane. As a result, it is highly likely that the unfolded chain will exit out of the membrane and enter the aqueous solvent before it can refold and return to the membrane. However, there is another issue remaining, which is when an unfolded helix exits the membrane, the total volume that occupies the membrane is reduced and hence can create a gap in the membrane. In a native membrane or a liposome, the gap will be rapidly filled up by other lipids, accompanied by a slight shrinkage of the cell membrane or the liposome. In nanodisc, however, such shrinkage is more energetically costly because the volume of the nanodisc is somewhat defined by the size of the membrane scaffolding protein (MSP). Therefore, it remains to be determined to what level the dynamics of a membrane protein resemble when it is embedded in a liposome compared to a nanodisc or a micelle. To achieve this, I explored the application of HDX-MS to membrane proteins embedded in liposomes.

To date, there are very few studies of HDX-MS on proteoliposomes. Anderson et al. 2018 demonstrated that by using an automated phospholipid removal platform that employs zirconium oxide (ZrO_2) beads and nanofilters, they can obtain 66% sequence coverage for a single-pass transmembrane protein FcγRIIa embedded in liposomes. Yet no studies as far as we know have

been done on proteoliposomes containing multipass transmembrane proteins, which we expect will present more challenges compared to the single-pass membrane protein due to a more complicated folding and unfolding process. One great challenge is that the presence of large amounts of lipids largely hinders proteolysis and LC-MS, and efforts need to be made to remove the lipids from the LC and the MS.

Given the motivations described above, in Chapter 4.1, I describe optimizations I performed on each component of the HDX-MS pipeline to achieve optimal sequence coverage and signal-to-noise levels with minimized carryover for membrane proteins in liposomes, including sample preparation, HDX, proteolysis, LC, and MS.

4.1.2 Proteoliposome sample preparation for HDX-MS

When intended to be used for functional assays or structural determinations, the liposome reconstitution protocol for each membrane protein is individually optimized to achieve a high enough yield and ideally uniform orientations of the membrane protein in the bilayer. For HDX-MS studies, it is reasonable to start from the established reconstitution protocol and optimize from there. Particularly, the optimized protocol should aim for minimal lipid:protein ratio. This is because the presence of lipids largely hinders the LC-MS process by causing issues including poor digestion, column fouling, and ion suppression. Reconstitution protocols used for functional or structural studies usually prefer a high lipid:protein ratio, sometimes even one membrane protein per liposome, to allow for single molecule analysis. Therefore, one should screen for different lipid:protein ratios and find the lowest ratio possible to generate enough protein samples.

Having a mixture of inside-out and outside-out orientations of the membrane protein in the liposome usually presents a great challenge to the particle alignment process in structural studies. For HDX-MS studies, one can in fact sometimes benefit from having mixed orientations. If a liposome is relatively large, and hence minimal curvature, and has the same conditions inside and outside, then inside-out and outside-out proteins should have the same dynamics. As one changes the conditions of the "extracellular" side of the liposome, proteins with different orientations will behave differently. For example, for KvAP, a voltage-sensitive K^+ channel, as one induce negative voltage for the lumen of the liposome, outside-out KvAP molecules will experience negative potential while inside-out KvAP molecules will experience positive potential with the same magnitude. Based on KvAP's current to voltage response, molecules experiencing negative potential will open while those experiencing positive potential will stay closed. If the stability for the open and closed KvAP molecules are similar enough, one may see bimodality in the MS spectra where the two isotopic distributions correspond to the KvAP molecules in the two different orientations. Being able to tell the orientation of the membrane proteins in the liposome and being able to observe their dynamics from the same measurement, provide an excellent internal control for measuring the conformational changes of a membrane protein in response to environmental changes. Therefore, it is not as critical for HDX-MS studies to obtain a uniform orientation of membrane proteins during the reconstitution and sometimes efforts need to be made to obtain an equal distribution of the orientations for the purpose of being able to measure different conformations at the same time.

Additionally, because HDX rates scale exponentially with the pH, one should be mindful of the pH when reconstituting a membrane protein into liposomes. Once a membrane protein is

inserted into liposomes and detergents are removed, the pH for the liposome lumen can not be changed without perturbing the integrity of the liposomes. Therefore, the HDX reaction has to be initiated under the same pH at the liposome lumen or else the “intracellular” and the “extracellular” side of the protein will experience different pH and hence have different intrinsic exchange rates. One exception is the study of pH-sensitive membrane proteins, in which a pH gradient is purposefully established to activate the protein. Under this condition, one needs to take account into the pH-dependent exchange rates in addition to pH-induced conformational changes.

4.1.3 Optimize protease digestion and signal-to-noise for membrane proteins in liposomes

The most common rate-limiting step for an HDX-MS study is obtaining a good peptide map. This task is highly dependent on having extensive protease digestion. Poor digestion will result in very few peptides and a low sequence coverage, resulting in little useful information in the HDX-MS study. Since membrane proteins are generally highly stable and require nonpolar solvents, it is extra challenging to obtain extensive digestion. Fortunately, it is very common that after a few MS/MS attempts, one obtains high sequence coverage and redundancy for the soluble domains but not for the transmembrane domain (TMD). Here I list a few parameters that I have explored in attempts to good peptide maps for the membrane proteins I have worked on, including KvAP, prestin and variants, and SLC26A9.

4.1.3.1 Quench conditions and detergents

The first parameter I optimized was quench conditions, including the buffer, denaturants, reducing reagents, and detergents.

Low pH Quench buffer

In most of my HDX-MS experiments, I used 600 mM Glycine, pH 2.5, as my quench buffer. Phosphate and formic acid (FA) are also common HDX quench buffers and are used by other HDX-MS studies in the literature. The reason for choosing glycine over phosphate is that the latter precipitates with a variety of divalent ions and detergents which are often necessary to keep membrane proteins from precipitating, and FA can sometimes precipitate membrane proteins as well. Nevertheless, I did not find significant differences between 600 mM Glycine and 1% FA as the quench buffer.

Denaturants

Denaturants are commonly used in the quench buffer to assist in solubilizing and unfolding the protein which improves protease digestion. Among these, guanidinium chloride (Gdm) and urea are most commonly used, and one needs to control the final concentration of the denaturants to prevent denaturing, and hence, deactivating the protease. Generally, soluble pepsin can tolerate 1 M of Gdm or 2 M of urea whereas immobilized pepsin is more resistant to unfolding and can tolerate up to 2 M of Gdm or 4 M of urea even after repeated usage. Because Gdm is charged and large amounts of denaturants are used, it usually cannot be completely removed at the desalting step and residual Gdm can cause ion suppression issues during MS, leading to poor signal-to-noise

levels for peptides of interest. Gdm also precipitates with a variety of molecules. In my initial attempts to obtain a peptide map for KvAP, I used 4 M Gdm in my quench (2 M Gdm final). Later I discovered that 8 M urea instead can significantly increase the s/n of the KvAP peptides and I used 8 M urea for all subsequent HDX-MS experiments including those performed on prestin and SLC26A9. One concern regarding the use of urea is the carbamylation reaction which modifies the side chain of lysines. The first step for the carbamylation reaction is the conversion of urea into cyanide. This step is highly pH and temperature dependent. At quench condition of pH 2.5 and 0 °C, the reaction is slowed down considerably. At equilibrium, only ~10 μM of cyanide is present for a solution containing 8 M urea at pH 3, 0 °C, after 50 days. Given the reasons above, I assumed that carbamlyation for my quenched protein was not significant.

Reducing reagents

Reducing reagents are required in quench buffer when the protein of interest forms disulfide bonds. Some studies report that adding TCEP assists protease digestion even for proteins without disulfide bonds. However, because high concentrations of TCEP (0.25 ~ 1 M final) are usually used to compensate for the slowed reaction rates at low pH, this leads to ion suppression as well due to incomplete desalting. For my HDX-MS studies, I tested whether the addition of TCEP improves the digestion for prestin, but negative effects were observed and hence no TCEP was used for any of the reported HDX-MS experiments in my dissertation.

Detergents

Lastly and most importantly for membrane proteins is the use of detergents in the quench buffer. To achieve efficient protease digestion, one must break the liposomes to expose the lumen side of the membrane proteins. Detergents are commonly used to solubilize liposomes and ZrO_2 beads have been shown to effectively remove lipids from nanodiscs for HDX-MS studies.[68] Incomplete solubilization of vesicles can lead to poor digestion for at least two reasons: 1) ZrO_2 removes lipids that are still associated with the protein, resulting in protein loss; 2) lipid removal by ZrO_2 is less efficient because it is hard for ZrO_2 to pull down large vesicles versus lipid/detergent mixed micelles.

What detergent should be used and how much? Different detergents solubilize liposomes via different mechanisms, associated with different solubilizing rates.[69] Because quenched HDX reaction must be analyzed by LC-MS immediately to minimize back exchange, the selected detergent should have a high vesicle-solubilizing rate. The vesicle-solubilizing rates for various commonly used detergents have been characterized by Lete & Goni 2019 via turbidity measurements.[69] Additionally, the concentration of detergents needed to solubilize lipid vesicles varies by detergent and is not only dependent on the critical micellar concentration (CMC). The required detergent concentration should follow the equation below, described by Lichtenberg et al., 2013:[70]

$$[Detergent]_{total} \geq D_w^{sol} + R_e^{sol}[lipid] \quad \text{(Equation 1)}$$

Where D_w^{sol} is the concentration of detergent in an aqueous environment at the completion of vesicle solubilization, and R_e^{sol} is the detergent-to-lipid ratio required for complete vesicle solubilization. The total amount of detergent used should also be sufficient to all micelle molecules

to solubilize all the protein molecules, i.e., detergent concentrations should also follow the equation:

$$[Detergent]_{total} \geq [protein] * (aggregation\ number) + CMC \quad \text{(Equation 2)}$$

where aggregation number is the number of detergent molecules required to form one micelle. Finally, if possible, detergents with a low CMC should be used to avoid overloading MS with detergents. Additionally, non-ionic detergents are preferred to avoid ion suppression.

Based on the above criteria, I tested the following detergents – DDM, DM, Triton X-100, C12E9, C12E8, FC12, LDAO, and OG. Among which, DDM, Triton X-100, C12E9, C12E8, and FC12 were used initially on KvAP studies. To evaluate the efficiency of digestion, I compared the extracted ion current (XIC) for 6 KvAP peptides rather than comparing the peptide search results to focus more on the raw MS1 s/n instead of the MS2 results. The six KvAP peptides were chosen because they cover regions of KvAP whose conformations may change upon the closing or opening of the channel. The identity, m/z for the monoisotopic peak, and the retention time (RT) for the six peptides are: 1) Peptide 62-80, m/z=763.08, RT~7.2-7.4; 2) Peptide 86-102, m/z=938.55, RT~9.3; 3) Peptide 170-184, m/z=847.93, RT~8; 4) Peptide 194-215, m/z=1050, RT~9; 5) Peptide 201-215, m/z=725.44, RT~8.3-9.1; 6) Peptide 235-252, m/z=964.53, RT~6.7-7.5. DDM was used as the reference, and the relative XIC intensity for the six peptides using different detergents were reported in Table 4. A detergent blank run was done before every run to ensure that no carryover.

Table 4: Detergent screening in the quench buffer to increase the signal-to-noise of KvAP peptides.

Detergent and final concentration	Peptide 62-80	Peptide 86-102	Peptide 170-184	Peptide 194-215	Peptide 201-215	Peptide 235-252	Notes
DDM, 0.1%	1x	1x	1x	1x	1x	1x	
Triton - X100, 0.2%	2x	7x	10x	4.7x	22x	5x	Very broad elution and suppressed peptide signals, like PEG.
C12E9, 0.07%	1.5x	4x	3x	4x	20x	5x	Not analytical grade and had a very broad elution and suppressed peptide signals similarly to Triton-X100.
FC12, 0.17%	2x	2x	1.5	1x	10x	3x	
C12E8, 0.055%	6x	35x	15x	8x	47x	15x	No detergent carryover at 10-40% ACN (RT before 13 min).

From Table 4, it was clear that among the tested detergents, C12E8 resulted in the best peptide s/n with XICs 6~47-fold higher than the XICs when DDM was used. It is worth noting that DDM, although being used in a number of HDX-MS studies on membrane proteins embedded in nanodiscs, is a very slow vesicle-solubilizing detergent, as evidenced by a tubidity of 87% after one minute of incubation of egg PC LUV with DDM.[69] Triton X-100, although being generally not used in LC-MS studies due to its heterogeneity and hence widespread elution and ion suppression, was still tested in hopes of obtaining a KvAP peptide map because our choices of fast-solubilizing detergents was very limited. Although the C12E8 (Analytical Grade, Anatrace) I used was analytical grade, it still had some heterogeneity which was manifested by a broad elution from 3.6 min to 12 min of the ACN gradient. Thankfully, the majority of the C12E8 species eluted after 12 min, separated from where most of the peptides elute (before 12 min) (Figure 4.1). Overall,

the use of C12E8 significantly and reproducibly increased the s-n of KvAP peptides.

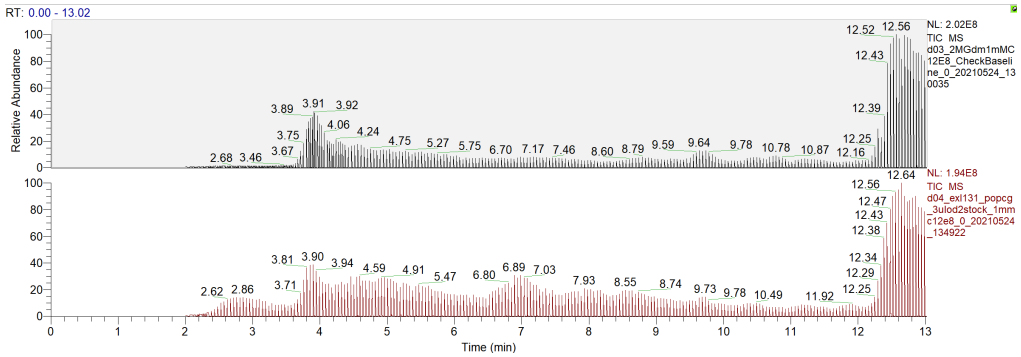

Figure 4.1 Elution profile of the quench buffer containing C12E8 (top, black) and KvAP peptides quenched with C12E8 (bottom, red).

In my later attempts to obtain a peptide map for SLC26A9 embedded in liposome, I tested the detergents LDAO and OG. Both generated decent peptide s/n, but every time LDAO was used, the isocratic pressure for the LC increased by ~200 psi and very slowly decreased over the run and pepsin washes. I suspect that LDAO might precipitate under acidic conditions and hence, led to the increased isocratic pressure, although I could not find reports from the literature to support this hypothesis. OG is a fast-solubilizing detergent. Nanodrop readings of turbidity dropped to noise level immediately after mixing SLC26A9 proteoliposomes with OG. However, the CMC for OG is high and hence a high concentration is required to solubilize liposomes. This issue can be resolved by adding an SEC column after the protease column to separate peptides and OG molecules, i.e., divert the flow to waste after peptides elute and before OG elutes.

Overall, the use of detergent for HDX-MS studies on membrane protein is essential to the success. The main item is that after the quench, one should find the condition that uses the minimal amount of detergent to keep the membrane protein soluble before protease digestion, and ideally,

destabilize the protein to allow more complete digestion. This usually requires a final detergent concentration to be above its CMC so that micelles are still intact to solubilize the membrane protein. For certain detergents with a very slow demicellelation time, on the order of minutes and hours, such as LNMG and GDN, it is possible to have a final detergent concentration lower than its CMC as the micelles will not disassemble before the membrane protein arrives the protease column.

4.1.3.2 Protease and protease cartridges

Protease options for HDX-MS studies are limited to aspartyl proteases due to the need for keeping quenched reaction at low pH (i.e., < pH 2.5) to minimize back exchange. The most common protease used is pepsin. Other proteases that have been employed in HDX-MS studies include rhizopuspepsin (protease type XVIII), aspergillopepsin (protease type XIII, or FPXIII), nepenthesin I (Nep I), and nepenthesin II (Nep II).[71] For my HDX-MS studies, I mainly explored the usage of pepsin and FPXIII for protease digestion. When studying a new protein, one should test all proteases available to evaluate their digestion levels. It is worth noting that although different proteases have cleavage preferences, so far no pattern has been found in terms of what protease provides the highest digestion for a given protein based on the protein's sequence and/or structure. Therefore, to find the protease that generates the best peptide map (i.e., high sequence coverage and high redundancy), one has to test them one by one systematically. Different combinations of protease can also be used. For example, a mixed protease column packed with pepsin and FPXIII, or two protease columns in tandem.

One can also choose to perform the protease digestion online or offline. Online digestion involves flowing the quenched HDX reaction containing intact polypeptide chain through the LC into a column with immobilized protease. For offline digestion, soluble protease is directly added to the quenched mixture and digestion is carried out by incubation on ice for a few minutes before the mixture containing the peptides is loaded onto the LC-MS. In general, online digestion yields better efficiency due to multiple reasons, including high local protease concentration, closer protease contact, better protease exposure due to the flow, and more destabilized protein under LC pressure compared to atmosphere pressure. There are instances where offline digestion generates more peptides. For example, when the protein of interest is protected by other molecules in the solution, or when the protein adopts a very non-globular shape which may prevent it from entering the protease column where the beads are tightly packed.

For KvAP, the identity of the peptides and peptide XIC did not change significantly when a mixed pepsin/FPXIII protease column was used compared to when a pepsin-only column was used. Therefore, I concluded that FPXIII did not assist in the digestion of KvAP. Offline digestion reproducibly generated fewer peptides than online digestion, independent of the identity of the protease. As I will discuss in the next section on LC and carryover, membrane proteins can have a significant amount of unwanted carryover from prior runs. After employing the major modifications to the LC as discussed below, I discovered that when a plastic cartridge (1 mm ID × 2 cm, IDEX C-128) instead of a metal cartridge (2 mm ID × 2 cm, IDEX C-130B) was used to house the immobilized protease, the carryover for the stickiest peptides dropped from 70-100% to 20-30%. Metal surface likely binds to the charged head groups of the lipids, which bind to membrane proteins, resulting in high carryover. When I cleaned the metal frits from the metal

cartridges by bath sonication in 10% FA, the solution after sonication was significantly more turbid than before sonication, supporting the idea that the reason for high carryover when using a metal protease cartridge is the binding between the metal surface and the lipids. Given the same reasoning, the difference in carryover was unlikely caused by the plastic cartridge being four times smaller in volume than the metal cartridge, although having a smaller cartridge can potentially reduce carryover by serving as a smaller reservoir.

4.1.3.3 LC and carryover

Reverse phase liquid chromatography (RPLC) is the most commonly used LC method for HDX-MS studies. Generally, peptides produced by protease digestion are captured by a trap column. The valve containing the trap column is then switched to redirect the flow to the binary pump which delivers a gradient of ACN through the trap column to elute the peptides. The peptides are then further separated by the analytical column. For most HDX-MS studies on proteins, C8 and C18 are commonly used as a trap column and/or an analytical column as their long alkyl chains can effectively bind to peptides and release them in the presence of a certain %ACN. In general, C18 binds to peptides more tightly than C8 due to its longer alkyl chains and hence stronger hydrophobility. Peptides generated from membrane proteins can be more hydrophobic due to the presence of more hydrophobic side chains than peptides from soluble proteins. Therefore, C18 can sometimes bind to peptides from membrane proteins too strongly, resulting in elution at a very high %ACN or even requiring a stronger organic solvent. For my initial HDX-MS experiments, I used a C8 trap column and a C18 analytical column per recommendations by the Nest Group. Most

peptides eluted before 40% ACN and stretching the ACN gradient and/or collect MS spectra at high %ACN did not help identify more peptides.

One of the main challenges for HDX-MS studies on membrane proteins is the potential for high carryover. Sources of carryover include every part of the LC, including the syringe, the injection port, lines, valves, frits, and of course columns. Different wash solutions have been explored to clean the LC so as to reduce carryover and they have been tested in my HDX-MS studies on KvAP. In the following description of screening conditions to reduce carryover, the metrics used are the XICs of the 6 example peptides that are prone to carryover, rather than the peptide search results for MS/MS. The reason for using XICs instead of search results is that so that the raw signal-to-noise levels are traced to minimize biases arise from differences in the MS/MS results due to the presence of different contaminants from run to run.

The carryover levels for KvAP were extraordinarily high. A detergent-containing blank run following the sample run contained peptide XICs that were 10-fold higher than those observed in the sample run. It is worth noting that carryover was observed in blank runs containing all the buffers but the detergent, emphasizing the mechanism of carryover – undigested and/or partially digested KvAP molecules stayed trapped in or upstream of the protease column, slowly being digested during the gradient of the sample run and could only be eluted when a detergent was introduced. Because each LC-MS run is 35 min including the column cleaning time, the trapped KvAP molecules had more time to be cleaved into peptides then the standard 2 min digestion time, resulting in a 10-fold increase in the XICs.

To analyze the main source of carryover, one can remove or bypass each part of the LC and see when the carryover is largely reduced. For KvAP, when the standard HDX-MS protocol

for lipid-containing membrane protein was used[72] in which DDM was used in the quench buffer, the main source of carryover was the trap column. When I replaced DDM with C12E8, the carryover from the trap column was greatly reduced, and the main source became the protease column. It was likely that C12E8 had a weaker binding ability to the trap column than DDM, and therefore hosted more KvAP peptides in the trap column. It was unlikely, however, that the carryover from the protease column was increased due to the usage of C12E8. Rather the main source was shifted to the first column that the sample passed through because the amount of peptides that bound too strongly to the trap was reduced. To reduce the carryover from the protease column and the trap column, various wash solutions were injected after a sample run and before a C12E8 blank run, and carryover from the test peptides was analyzed from the XICs in the C12E8 blank run. The results were presented in Table 5. From the table it was clear that conventional cleaning solutions to the pepsin column did not significantly reduce the carryover, while detergent-containing wash solutions were the most effective. Specifically, combining ionic and nonionic detergents, namely 0.1% foscholine-12 (FC12) and 0.11% C12E8, largely reduced the carryover from the pepsin column by 100-fold, from ~1000% to <10%. Because large amounts of detergent were used to clean the pepsin column, I flanked the two detergent washes with a conventional "cleanmix" of (5% (v/v) ACN/ 5% (v/v) IPA/ 20% (v/v) AcOH/70% (v/v) ddH2O[73]) wash to minimize ion suppression caused by residual detergents. The final wash solutions for the pepsin column after each sample injection were 100 uL injections of cleanmix, 0.1% FC12 in 0.1% FA, 0.11% C12E8 in 0.1%FA, and cleanmix. The wash injections were programmed into the PAL method to be performed by the robot during the ACN gradient so that no extra time or labor was spent outside the initial method programming stage. Regarding carryover from other columns,

washing C8, C18, and the syringe with 50% TFE (for C8, reverse and forward flow) helped reducing carryover, but the effect was not as significant as washing pepsin column with 0.1% FC12.

Table 5: Wash solutions tested to reduce KvAP carryover from the LC columns.

No.	Wash methods	%Carryover[a]
1	Pepsin column: 2*100 uL[b] cleanmix[c]; C8: cleanmix + magic mix[d] + 90% IPA, forward + reverse flow;	25-160%
2	Pepsin column: 2*100 uL cleanmix; C8: 2*100 uL 50% TFE;	11-180%
3	Pepsin column: 2*100 uL cleanmix; C8: cleanmix + 2*100 uL 50% TFE, reverse + forward flow; C18: 50% TFE	40-300%
4	Pepsin column: pepsin wash[e] + cleanmix + 250uL 0.1% FC12 in 0.1%FA, reverse (disconnect the column) + forward flow; C8: cleanmix + 2*100 uL 50% TFE; C18: 50% TFE;	0-100%
5	Pepsin column: pepsin wash + cleanmix + 0.1% FC12 in FA + cleanmix; C8: cleanmix + magic mix + 90% IPA + 2*100 uL 50% TFE, reverse + forward flow; C18: 50% TFE	0-30%
6	Pepsin column: 250 uL cleanmix + 0.1% FC12 in 0.1%FA + 0.11% C12E8 in 0.1%FA; C8: 250 uL cleanmix + 90% IPA + 50% TFE + 80% MeOH + 80% ACN, reverse flow, then cleanmix forward flow.	0-20%
7	Pepsin column: cleanmix + 0.1% FC12 in 0.1% FA + 0.11% C12E8 in 0.1%FA + cleanmix; C8: cleanmix + 90% IPA + 50% TFE + 80% MeOH + 80% ACN, reverse flow, then cleanmix forward flow.	0-10%

[a]%Carryover = peptide XIC in the C12E8-containing buffer run/peptide XIC in the sample run. XICs for six KvAP transmembrane peptides were used due to their high carryover and their importance in KvAP function and therefore a range of %carryover was reported in the table for each condition.

[b]Unless otherwise noted, 100 uL of each solution was injected. 2*100 uL means two injections were executed and each injection contained 100 uL of solution.

[c]Cleanmix: 5% (v/v) ACN/ 5% (v/v) IPA/ 20% (v/v) AcOH/70% (v/v) ddH_2O. From Majumdar *et al., JASMS*, 2012.[73]

[d]Magic mix: ACN:MeOH:IPA:H2O=1:1:1:1, 1% FA (typically 0.1-2% FA). Recommended by Waters to remove contaminants from HPLC.

[e]Pepsin wash: 1.5 M Gdm-HCl, 4% (v/v) MeOH, 0.8% (v/v) FA. From Jia *et al., Nature Comm.,* 2020.[74]

To further reduce the carryover from the trap column and the potential column fouling issue, I replaced the C8 column with a trap column self-packed with POROS20R2 resin in a plastic cartridge (1 mm ID × 2 cm, IDEX C-128) (referred to as an R2 column for short). The benefit of using a self-packed column was the higher flexibility of replacing the old column with a new column to prevent persistent carryover from accumulated proteins or detergents. CirAp (a largely disordered peptid) was used to compare the binding and elution ability as well as the separation efficiency of an R2 trap column with those of a C8 trap column, and no significant difference was found. Therefore, for my future HDX-MS studies, an R2 trap column was used instead of a C8 trap column.

Although the usage of C12E8 and the four solution washes to the pepsin column greatly reduced the carryover for KvAP, the stickiest peptides still suffered from 70-100% carryover. Further attempts to reduce carryover were summarized in Table 6. Among all the conditions tested, changing the protease cartridge from a metal cartridge to a plastic cartridge drastically reduced the carryover levels for the stickiest peptides from 70-100% to 20-30%, likely because the plastic cartridge retained fewer lipids due to weaker electrostatics between the surface of the cartridge and the lipid phospholipid head group, as compared to a metal cartridge. Additionally, I found that metal frits, just like metal surface, retained large amounts of lipids which could not be cleaned by sonicating in cleanmix, but the lipids could be effectively removed when sonicating the frits in 10% FA, likely due to disruption of the electrostatic interactions as well.

Table 6: Conditions tested to further reduce KvAP carryover.

No.	Condition tested	Notes[a]
1	Changed loop to 30cm peek	x
2	Chased[b] with 50 uL 2M Gdm quench/1 mM C12E8	2-4 x higher VSD signal than KvAP injection with no chase, but up to 5x lower VSD signal than its carryover
3	Chased with 50 uL 2M Gdm quench/1 mM C12E8	x
4	Chased with 50 uL 2M Gdm quench/2 mM C12E8	x
5	Chased with 50 uL 0.1%FA/1 mM C12E8, 2x digestion & desalting time	x
6	Chased with 100 uL 0.1%FA/1 mM C12E8, isocratic flow rate = 200 uL/min, standard digestion & desalting time	x
7	No. 2 + 1000 psi isocratic pressure restrictor pre-waste line	x
8	Chased with 2 M Gdm quench/2 mM DDM	x
9	Pulse in 3 uL 2% DDM post filter	x
10	Pulse in 3 uL 1.1% C12E8 post filter	x
11	Pulse in 6 uL 1.1% C12E8 post filter	x
12	Pepsin packed with plastic cartridge, new frits.	Reduced carryover of the stickiest peptide from 70-100% (metal cartridges) to 20-30% (plastic cartridges).
13	Pepsin packed with metal cartridge, changed frits to ones that were never contamininated with lipids.	Sonicating the old protease column frits in 10% FA for 20-25 min makes the solution visibly cloudy, suggesting that lipids got stripped off from frits by FA, likely through electrostatics. Protease column packed with those 10% FA sonicate cleaned frits did not have the high pressure issue anymore. For future reference, all protease column frits that may be lipid contaminated need to be sonicated in 10% FA for cleaning.

[a]An "x" means that cleaning condition did not result in a significant difference in carryover.
[b]Chase was performed by injecting the specified solution into the sample loop right before injecting the sample, and because the flow for the sample loop was reversed during loading, the chase solution was sent to the rest of the LC after the sample.

4.1.4 Summary of the optimized HDX-MS protocol for KvAP

Given the optimizations on sample preparation, protease digestion, signal-to-noise levels, and carryover levels for KvAP described above, here I provide a summary of the final HDX-MS protocol for KvAP.

HDX reaction was initiated by diluting 2 uL of 50 uM KvAP in POPC/POPG (3:1) liposomes (protein:lipid ~ 1:6 w/w) with 28 uL of the labeling buffer made with D_2O. The HDX reaction was quenched via the addition of 30 μL of ice-chilled quench buffer consisting of 27 uL of 600 mM Glycine, pH 2.5, 8 M urea and 3 uL of 1.1% C12E8/ddH_2O. The mixture was incubated on ice for 1 min to fully solubilize the liposomes, and then 3 μL of a 300 mg/mL aqueous suspension of ZrO2-coated silica (Sigma-Aldrich, reference no. 55261-U) was added to remove the lipids. The solution was incubated on ice for another 1 min before detergent solubilized KvAP was obtained by filtering the resulting mixture through a cellulose acetate spin cup (Thermo Pierce, Waltham, Massachusetts, reference no. 69702) by centrifugation for 30 s at 13,000 g, 2 °C. The filtrate was either flash frozen in a dry ice/ethanol bath and stored at -80 °C until injection onto the LC-MS system or was directly injected into the LC-MS system.

Upon injection, the protein was digested online by a pepsin (Sigma-Aldrich P6887) mixed protease column maintained at 20 °C. Protease columns were prepared in-house by coupling the protease to a resin (Thermo Scientific POROS 20 Al 430 aldehyde activated resin 1602906) and hand-packing into a column (1 mm ID × 2 cm, IDEX C-128). After digestion, peptides were desalted by flowing across a hand-packed trap column (Thermo Scientific POROS R2 reversed-phase resin 1112906, 1 mm ID × 2 cm, IDEX C-128) at 5 °C. The total time for digestion and desalting was 2.5 min at 100 μL/min of 0.1% formic acid at pH 2.5. Peptides were then separated

on a C18 analytical column (TARGA, Higgins Analytical, TS-435 05M5-C183, 50 x 0.5 mm, 3 μm particle size) via a 14-min, 10–60% (vol/vol) ACN (0.1% FA) gradient applied by a Dionex UltiMate-3000 pump. During the ACN gradient the pepsin column was washed by four sequential 100 uL injections consisting of cleanmix, 0.1% FC12 in 0.1% FA, 0.11% C12E8 in 0.1%FA, and cleanmix to reduce carryover. Eluted peptides were analyzed by a Thermo Q Exactive mass spectrometer. MS data collection, peptide assignments by SearchGUI version 4.0.25, and HDX data processing by HDExaminer 3.1 (Sierra Analytics) were performed as described in Chapter 2.1.6.

It is worth noting that although attempts were made to remove the lipids from the LC-MS, a significant amount of lipids were retained in the LC and sent to the MS. We frequently encountered MS signal-to-noise issues such as low calibration mixture signals and unstable sprays. Many of the issues arose from lipid contamination at the needle and/or the optics of the MS, and the latter can cause charging issues. Therefore, frequent routine maintenance and cleaning, even deep cleaning, generally are necessary when working with membrane proteins containing detergents and/or lipids.

4.2 Probing voltage-dependent conformation changes of KvAP using HDX-MS under an applied electric field

4.2.1 Abstract

The protocol for HDX-MS studies on proteoliposomes developed in Chapter 4.1 was applied to a voltage-dependent K^+ channel, KvAP, reconstituted in liposomes. By applying membrane potential through a K^+ gradient and an ionophore, the dynamic and thermodynamic responses of KvAP to

voltage were measured at the peptide level and the residue level for the selectivity filter. No significant HDX response was observed under applied membrane potential likely due to minor changes of the biological system itself and sample preparation. Future directions to advance the technique of electric field HDX-MS are listed at the end. Overall, this study serves as a proof-of-principle for future HDX-MS studies on proteoliposomes under applied membrane potential.

4.2.2 Introduction

Voltage-dependent membrane proteins detect changes in membrane potential via a voltage sensor domain (VSD) and transduce electrical signals across the cell membrane by interchanging their conformations between open and closed states.[75] This regulates various physiological processes, including the generation and propagation of action potentials and the regulation of cell differentiation.[76,77] Voltage-sensing membrane proteins usually function as tetramers, and each subunit contains six transmembrane helices (S1-S6), with S1-S4 forming the VSD and S5-S6 forming the pore domain.[78,79] The activation mechanism of VSD is highly conserved and well studied. The primary voltage sensor, the S4 helix, carries three to eight positively charged residues that are stabilized in the membrane via forming salt bridges between the negatively charged residues of S1-S3.[75,78] The aqueous environment of the crevices within the VSD leads to an electric field that is highly focused on a narrow hydrophobic region.[78,79] Upon depolarization of the plasma membrane, S4 translates so as to transfer its “gating charges” across the electric field by either large transmembrane movements or crevices rearrangement.[78,79]

How does a voltage-dependent membrane protein convert electrical energy of the membrane potential into the mechanical energy needed for conformational changes? How are

those structural alterations related to the functions? Thanks to recent advances of structural techniques, atomic resolution structures of many voltage-dependent membrane proteins in their open and closed states are resolved via X-ray crystallography and cryo-EM, and their voltage-sensing elements have been characterized. Although we can infer the mechanism of a voltage-dependent membrane protein from its structures, those static images do not provide direct information as to protein conformational dynamics and energy landscapes that underlie its mechanism and function. Moreover, even though we can access various structural states of a voltage-dependent membrane protein by changing buffer composition and creating mutations, all the structures are determined at 0 mV membrane potential. This creates gaps in understanding the voltage-sensing mechanism of a target protein. One of the most pervasively used solution-based approaches to study conformational dynamics of voltage-dependent membrane proteins is electron paramagnetic resonance spectroscopy (EPR).[4] However, this technique requires generating multiple site-directed mutations and, apart from the possibility of disrupting a protein's native structure, is rather low throughput.[4]

HDX is a powerful biophysical technique that allows us to directly monitor the hydrogen-bond patterns of a protein's backbone amides in solution, and hence provides direct evidence on the protein's conformational fluctuations without incorporation of any mutations or synthetic probes.[80] Structured, hydrogen-bonded backbone amides are protected from solvent deuterium and therefore will have slow H-to-D exchange. Amides involved in conformational transitions may be exposed to deuterium and therefore have faster H-to-D exchange. Combining HDX with MS, one can perform HDX measurements on large and complex proteins, with only submicromolar concentrations, and sometimes obtain residue level resolution.[80,81] This is particularly beneficial

for studying membrane proteins, which are usually difficult to purify and large in size. HDX-MS has been mostly used to study folding and dynamics of soluble proteins[7] and aggregation prone intrinsic disordered proteins.[8,9] In the past decade, HDX-MS has been increasingly applied to membrane proteins in lipid nanodiscs and detergent to study membrane topology and ligand-induced conformational changes.[11,12] To fill in the gaps between our understanding of static high-resolution structures acquired at 0 mV membrane potential and mechanistic functions of voltage-dependent membrane proteins, we need a method to characterize protein dynamics under applied voltage.

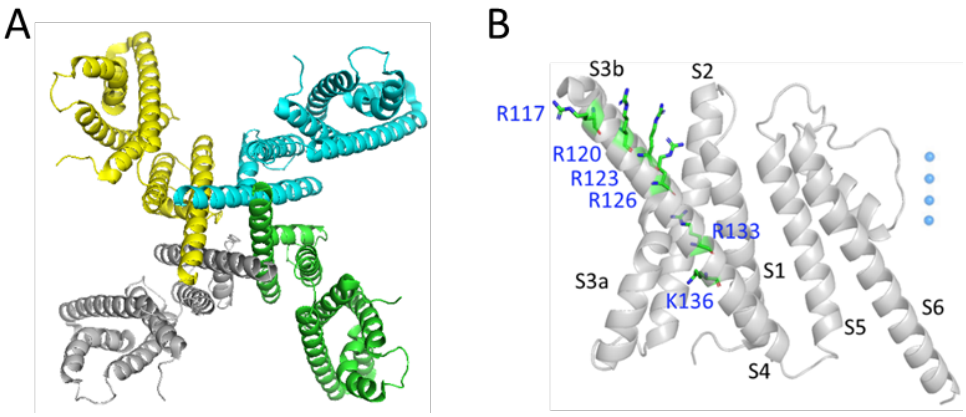

Figure 4.2: Ribbon representation of KvAP cryo-EM structure.
A) KvAP tetramer, viewed along the 4-fold axis, from the intracellular side. B) A single subunit of KvAP consists of six transmembrane helices (S1-S6). Viewed parallel to the membrane with the extracellular side up. Sticks show six basic residues on S4. Blue spheres show a queue of K+ ions in selectivity filter. Figure adopted from Tao and MacKinnon, 2019.[84]

KvAP is a Kv channel expressed in archaebacterium *Aeropyrum Pernix*. Crystal structures of KvAP reveal that it adopts the same topology as other Kv channels.[82,83] KvAP transports K^+ ions as tetramers, and each subunit consists of six transmembrane helices (S1-S6), including the VSD (S1-S4) and the pore (S5-S6) (Figure 4.2).[82] The N terminus of S4 contains six positively charged residues (Arg and Lys), known as "gating charges", that are stabilized by basic residues

in S1-S3 (Figure 4.2). The helix-turn-helix element made from S3b and S4 is the proposed voltage-sensing element.[82] The structures of KvAP in its open and closed states suggest that when the cell membrane is depolarized, S4 carries the gating charges across the electric field of the membrane through large rigid body movements and therefore moves the S5 helices to open the pore.[82,83]

The structural dynamics of KvAP have also been characterized by accessibility measurements. Site-directed spin labeling and EPR reveal that S4 is highly dynamic and although it resides at the protein-lipid interface, the gating charges are shielded from the hydrophobic environment.[85] Biotin-avidin accessibility measurements show that the outward force exerted on S4 by membrane electric field can lead to S4 movement across the membrane with a distance of 15-20 Å.[86] These observations on S4 translation upon activation agree with the recent cryo-EM structure of KvAP that reveals it to be a non-domain swapped voltage sensor that has distinguishable features from most other voltage-sensing ion channels.[84]

In this study, I developed protocols to monitor conformational fluctuations and energetics of a voltage-dependent membrane protein, KvAP, in liposomes in both resting and activated states with HDX-MS. We chose KvAP as our model protein because it has been investigated extensively in the past several decades and, as a result, its structures, voltage sensing mechanism, and conformational changes in open and closed states have been well characterized. Since proteins were reconstituted into a closed compartment, voltage was applied by creating a charge separation via diffusion potential generated by an ion gradient across the vesicle. By characterizing the hydrogen-bond patterns of KvAP under 0 mV and under applied voltage, I identified regions with changes in the hydrogen-bond stability as the channel underwent open-to-close state transition.

4.2.3 Results

4.2.3.1 Establishing a membrane potential

To apply voltage to liposomes, I first generated empty azolectin liposomes without KvAP. Empty liposomes in 1 mM KCl was diluted into a solution containing the same buffer composition but 200 mM KCl. A K^+ ionophore valinomycin was added to create a K^+ diffusion gradient.[87] As positive K^+ ions being transported across the lipid bilayer, a net positive charge accumulated on the inside of the liposome and a net negative charge accumulated on the outside. This created a charge separation and in turn generated an electric field. Net K^+ transport stopped when K^+ concentrations and the voltage across the lipid bilayer (Δφ) reached an equilibrium, described by the Nernst equation:

$$\Delta\varphi = \frac{RT}{F} ln \frac{[K+]out}{[K+]in} \qquad \text{(Equation 3)}$$

Because there will be ion leakage around the protein, the actual Δφ will be lower than the calculated Δφ. Therefore, I used a voltage-sensing dye Oxonol VI to quantitatively measure the Δφ. Oxonol VI is a ratiometric fluorescence probe that carries a negative charge. It re-distributes in the presence of inner-positive membrane potential, which leads to a shift of its emission spectrum towards a longer wavelength.[87,88] I first calibrated the fluorescence response of Oxonol VI to Δφ by monitoring its fluorescence intensity ratio at 640 nm and 614 nm under different K+ gradients. The calibration curve agreed well with that obtained from Holoubek et al., 2003.[87] The membrane potential was relatively stable with minimal leakage over the course of 5 hours. With the calibration curve of the membrane potential, I then reconstituted KcsA proteins into azolectin liposomes, and measured the membrane potential without a K^+ gradient and with a 1 mM/180 mM K^+ (in/out) gradient using Oxonol VI fluorescence. Some membrane leakage due to the presence

of KcsA molecules was observed as the calculated potential under a 1 mM/180 mM K^+ (in/out) gradient was only 73 mV as compared to 133 mV for empty liposomes. Similar to empty liposomes, the membrane potential was stable over the course of hours (Figure 4.3 E).

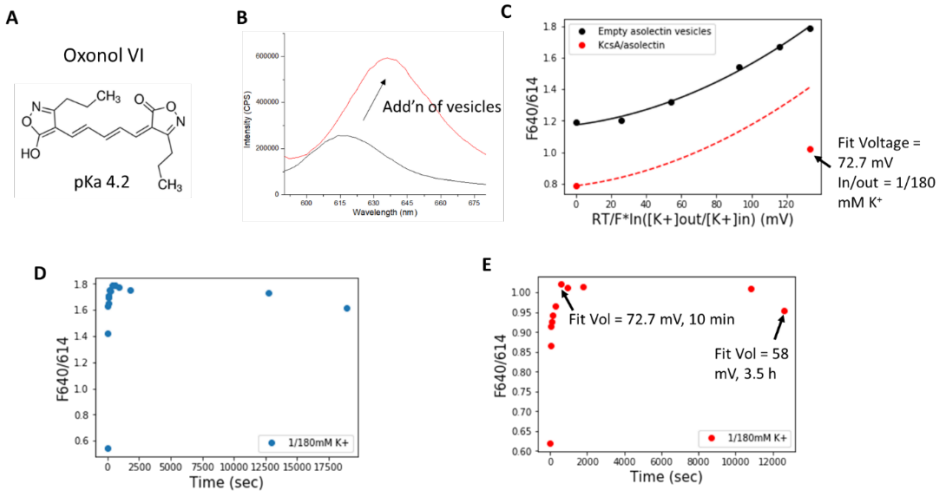

Figure 4.3: Ratiometric fluorescence measurements of membrane potential.
A) The voltage-sensing dye Oxonol VI used in this study to measure membrane potential. B) An example of the fluorescence emission spectra of Oxonol VI before (black) and after (red) the addition of empty azolectin vesicles. C) Estimation of the membrane potential by Oxonol VI fluorescence measurement using K^+ gradient-based calibration. The x-axis depicts the theoretical potential calculated from the K^+ gradient using the Nerst equation, and y-axis depicts the ratio of the fluorescence emission intensities of Oxonol VI at 640 nm and 614 nm. Data were fitted by a polynomial of the second order.[87] Red data points depict the fluorescence reponses of azolectin proteoliposome containing KcsA under a 1/1 mM K^+ and a 1/180 mM K^+ (in/out) gradient. The red dashed line depicts the estimated fluorescence under various K^+ gradients if the leakge of the KcsA proteoliposome equals that of the empty liposomes. D-E) Changes of the membrane potential over time for the empty liposome (D) and the KcsA-containing proteoliposome (E) measured by the fluorescence intensity ratio at 640 nm and 614 nm.

4.2.3.2 Obtaining a peptide map for KvAP

The HDX-MS protocol used for the studies of KvAP is described in detail in Chapters 4.1.4 & 4.2.5. Figure 4.4 describes the detailed protocol with optimization steps I developed highlighted in red. The protocol generated 71 unique KvAP peptides, with a 75% sequence coverage of the

TMD (Figure 4.5). Among the transmembrane helices, the S1, S2, and the extracellular portion of the S4 had poor sequence coverage, while other regions had decent coverage especially the pore domain which had near full coverage. However, later in the HDX-MS studies of KvAP, the MS had signal-to-noise issues so that many of the low-signal peptides, especially the ones covering the VSD, were no longer detectable.

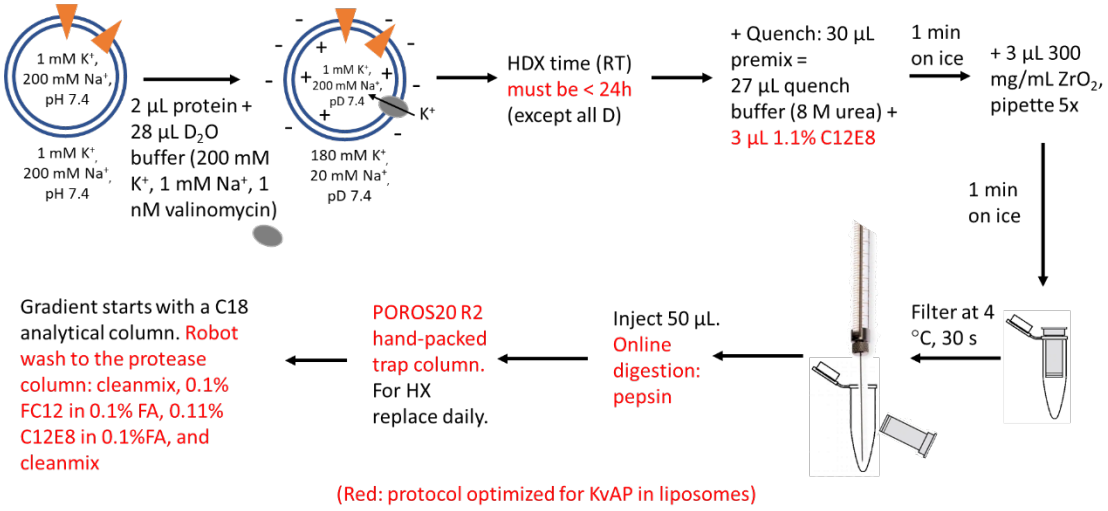

Figure 4.4: Modified workflow for running KvAP proteoliposome samples in LC-MS.

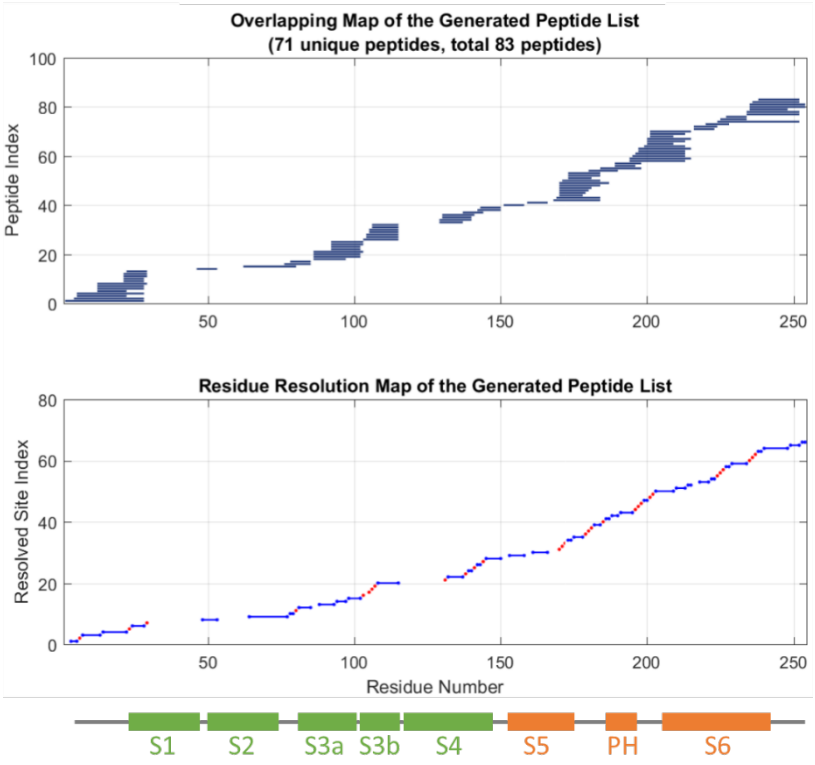

Figure 4.5: The sequence coverage of KvAP.
Top: each blue bar represents one peptide, with the x-axis being the residue number. Middle: residue resolution of the generated peptide list. Red dots indicate single residue resolution. Bottom: the secondary structures of KvAP aligned with the residue number.

4.2.3.3 HDX-MS on KvAP liposomes under membrane potential

In summary, the HDX for KvAP at different regions varied greatly, highlighting the broad stability range within the protein. The VSD of KvAP exhibited the slowest HDX, pointing to its high stability, while the pore domain displayed faster HDX with a lower stability (Figure 4.6 & Figure 4.7). Exchange was completed at the earliest time point collected (i.e., 10s) for the N- and C-terminus of KvAP, pointing to their intrinsic instability (Figure 4.7). To our disappointment, we did not observe significant differences induced by membrane potential (Figure 4.6 & Figure 4.7).

However, we were able to obtain site resolved resolution of thermodynamics at the selectivity filter (Figure 4.8). For the rest of this subchapter, I provide a detailed description of the HDX results for KvAP in the presence and absence of membrane potential.

The KvAP construct used in this study contained residues 14-295, mutations A15L and C260S, and a 6xHis tag at the C-terminus with a TEV cleavage site. KvAP was expressed in *E. coli*, purified via Ni affinity chromatography and size exclusion chromatography using DDM as the purification detergent, and then was reconstituted into liposomes at pH 7.4 in 1 mM K^+. Reconstituted proteoliposomes were immediately used for HDX labeling (i.e., labeling was initiated within 24 h of reconstitution). A membrane potential was established by a 1/180 (in/out) mM K^+ gradient and the addition of 1 nM valinomycin. This ratio could lead to a 3 kcal mol^{-1} change in stability, to be reported by changes in HDX rates. HDX was measured in the absence and presence of an established membrane potential at pD_{read} 7 at room temperature.

All peptides showed exchange within the longest labeling time of ~10^5s, suggesting that the overall apparent stability of KvAP is within 8.4 kcal/mol, given a k_{chem} of $(100\ ms)^{-1}$ at pD_{read} 7 and room temperature. Regions closer to the membrane-water interface, namely the termini of the TM helices, exchanged faster than regions residing in the center of the membrane, namely the middle of the TM helices (Figure 4.6). This is consistent with the notion that water crevices are formed from both intracellular and extracellular sides of the membrane, especially for the VSD. Peptides forming the pore domain, particularly the linker between S5 and the pore helix, pore helix, selectivity filter, and S6, all exhibited faster exchange than peptides forming the VSD, highlighting the lower stability of the pore domain than the VSD (Figure 4.7). The observed low stability of the

pore domain likely originates from the greater solvent accessibility than the rest of the TM helices of KvAP.

Strikingly, multiple overlapping peptides were obtained at regions covering the selectivity filter, allowing us to observe site resolved thermodynamics of the selectivity filter of KvAP by subtracting the deuteration levels of the overlapping peptides (Figure 4.8). The selectivity filter exhibited an apparent stability of ~4.2 kcal/mol, with an exchange rate of ~1/100 s^{-1}. Interestingly, the N-terminal half of the selectivity filter appeared to be more stable than the C-terminal half by ~1.4 kcal/mol, with an apparent protection factor of $4*10^3$ and $4*10^2$, respectively. This difference in stability highlights that the top half (i.e., the C-terminal half) of the selectivity filter possesses a greater flexibility in coordinating K^+ ions than the bottom half (i.e., the N-terminal half) as the channel transitions between the open and the closed states.

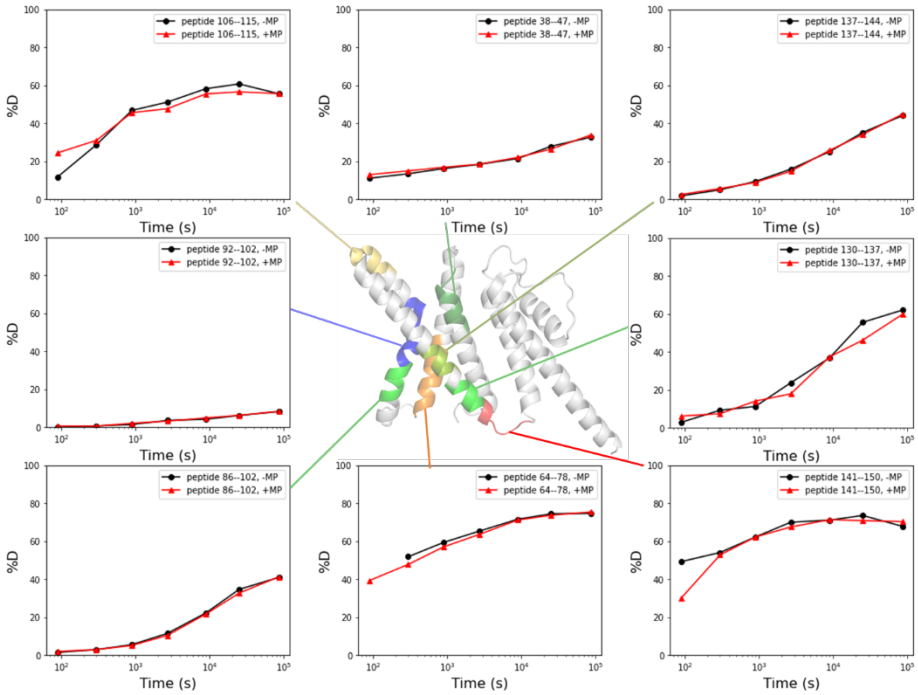

Figure 4.6: HDX for the voltage-sensing domain of KvAP.
One uptake plot for the colored region in the structure is shown, with the peptide sequence shown on the top right. -MP and +MP stand for in the absence and presence of a membrane potential, respectively.

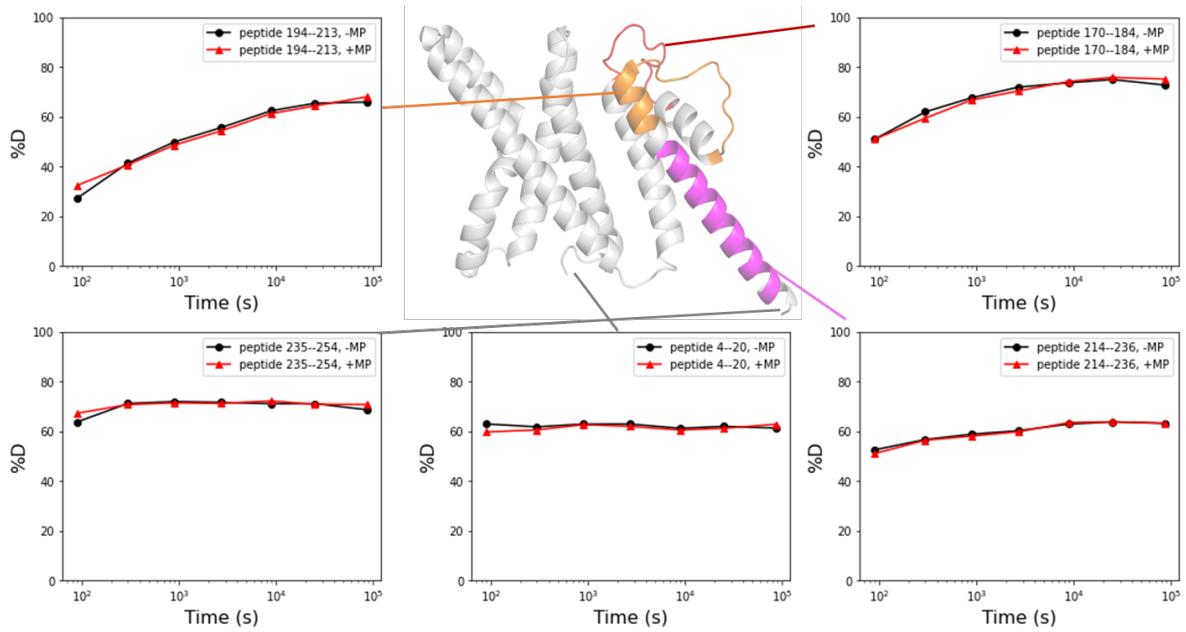

Figure 4.7: HDX for the pore domain and the termini of KvAP.

One uptake plot for the colored region in the structure is shown, with the peptide sequence shown on the top right. -MP and +MP stand for in the absence and presence of a membrane potential, respectively. Structures of peptide 4-20 and peptide 235-254 are not resolved.

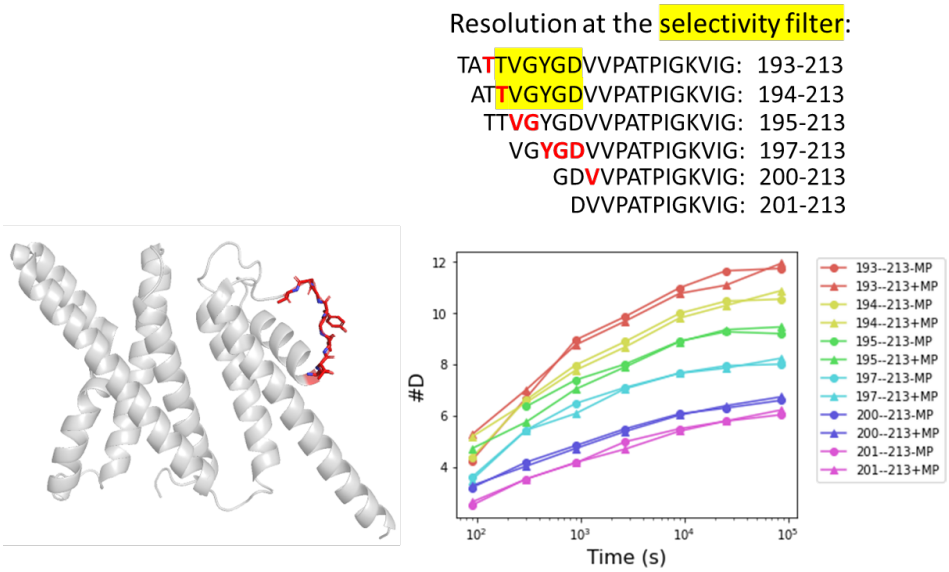

Figure 4.8: Site resolved HDX for the selectivity filter of KvAP.
-MP and +MP stand for in the absence and presence of a membrane potential, respectively.

4.2.4 Discussion and next steps

In this study, I developed protocol for measuring HDX-MS while applying voltage across proteoliposome bilayers and applied it to KvAP. The HDX results provided detailed thermodynamic and dynamic information for KvAP at the peptide level and even at the residue level for the selectivity filter. Although no significant HDX response was observed under applied membrane potential, this study serves as a proof-of-principle for future HDX-MS studies on proteoliposomes.

Two potential reasons can explain the observed little HDX changes under membrane potential. First, minimal hydrogen-bond pattern changes are expected for K^+ channels during their conformational transition according to the known structures[84] and previous solvent accessibility measurements.[89,90] Conformational changes in the VSD are mostly rigid body movements in which the S4 helix containing the arginine residues rotates and translates in the membrane, leading to conformational changes of the pore domain. Such rigid body movements cannot be identified via HDX. Additionally, conformational rearrangements at the selectivity filter identified by structures are mainly reorientations of the carbonyl groups of the peptide backbone and stability changes for the amides are likely to be minimal. The second explanation for the unchanged HDX under membrane potential is the potential flaws in the sample preparation including mixed orientation of KvAP in liposomes, vesicle multi-lamellarity, and membrane leakage. Below I discuss each of thes factors.

A membrane protein can be inserted into liposomes in an inside-out or an outside-out orientation. The relative orientation is dependent on the identity of the protein as well as the reconstitution protocol. If both orientations of KvAP were present in the present HDX-MS study,

then the two KvAP populations experienced membrane potentials of opposite sign. According to Ruta et al., 2003[91] and other functional studies, KvAP fully opens under a positive potential. Therefore, I expect that outside-out KvAP molecules that experienced a positive potential adopted the same conformations as KvAP when no potential was applied, while the inside-out KvAP molecules underwent open-to-close conformational transition as they experienced a negative potential. Such conformational heterogeneity would be identified by HDX/MS as bimodal isotopic distributions arising from peptides coming from each orientation. However, in the present HDX-MS study, I did not observe consistent bimodality when a membrane potential was applied. This was likely because the hydrogen-bond patterns for KvAP adopting the two conformations were highly similar, and the two isotopic distributions were inseparable. Because the expected hydrogen-bond pattern changes for K^+ channels are so small, it is advised that a different voltage-sensing membrane protein should be used to develop HDX-MS methods under a membrane potential. Ideally, the model protein should have large folding or unfolding events induced by a membrane potential such large HDX changes are expected. In this case, under an applied voltage, proteins orienting differently will exhibit clear bimodal mass spectra and one can observe the thermodynamics of both conformations simultaneously.

In addition, vesicle multi-lamellarity can result in small HDX changes under voltage. KvAP molecules embedded in encapsulated vesicles will not experience the same membrane potential as those embedded in the outermost vesicle. In the present study, multi-lamellarity was reduced by carrying out HDX right after the reconstitution process. For future studies, one should extrude the proteoliposomes right before HDX (which will also scramble the orientations), and/or measure the size homogeneity of the proteoliposomes via dynamic light scattering (DLS) or

electron microscopy. Importantly, LUVs should appear clear by eye whereas multilamellar vesicles will appear to be cloudy due to large amounts of light scattering.

The last factor to be discussed here is membrane leakage. Leakage can be caused by the presence of membrane proteins, incomplete removal of detergents, lipid oxidation, etc. DM and DDM, the two detergents used for reconstitution and purification, respectively, can be detected by the MS as they elute off the LC around 30-45% ACN. In the present study, neither detergent was detected for KvAP proteoliposomes, suggesting that leakage caused by incomplete detergent removal was a minimal effect. Lipid oxidation was minimized by carrying out the reconstitution process followed by immediate HDX. Based on Figure 4.3, membrane leakage was minimal, and an established membrane potential should persist for hours. For future studies, a different method such as BioBeads can be used to further ensure complete detergent removal.

In conclusion, this study serves as a proof-of-principle that uses HDX-MS to probe the dynamics and thermodynamics of a voltage-dependent membrane protein under an applied membrane potential. Future studies are required with a different model protein that exhibits large folding events in response to voltage. Overall, HDX-MS on physiologically important ion channels can uncover structural and dynamics changes that lead to functionally distinct conformational states in solution. Establishment of this method will transition our focus on membrane protein structural biology from static structures to characterization of protein dynamics and energy landscapes.

4.2.5 Materials and methods

4.2.5.1 KvAP expression and purification

BL21(DE3) cells were transformed with a plasmid containing KvAP in a pET28(a) vector. One colony was inoculated in 50 mL LB media supplemented with 50 ug/mL kanamycin and grew at 37 °C overnight. 5 mL of the overnight culture was diluted to 500 mL ZYM-5052 autoinducing media[92] with 100 ug/mL kanamycin and incubated in 37 °C shaking at 240 rpm for 24 h for expression. Cells were harvested by centrifugation at 5500 rpm for 15 min at 4 °C. Each liter of cells was resuspended in 20 mL of lysis buffer (50 mM Tris, 100 mM KCl, 10 mM $MgSO_4$, 25 µg/mL Dnase I, 1 mM PMSF, pH8). Cells were glass homogenized. More lysis buffer was added to bring the total volume to 50 mL per liter of cells and then cells were incubated at room temperature rotating for 30 min.

Cells were lysed via 3.5 cycles of French Press. Inclusion bodies and cell debris were removed by centrifugation at 6000 rpm for 15min at 4 °C. The supernatant was ultracentrifuged at 37,000 rpm for 30 min at 4 °C to pellet the membrane fraction. The membrane pellet was glass homogenized in 20 mL of lysis buffer. KvAP was extracted with 40 mM DDM at 4 °C in the cold room rotating overnight (~20 h). After extraction, the mixture was clarified by ultracentrifugation at 40,000 rpm for 1 h at 4 °C. The supernatant was used to purify KvAP via Co affinity batch purification. Binding of KvAP to Co resin was carried out in the cold room rotating for 1 h. Co resin was washed with ~80 mL of lysis buffer containing 1 mM DDM and 20 mM imidazole. KvAP was eluted with 2 mL *3 of lysis buffer containing 1 mM DDM and 400 mM imidazole. The elute was concentrated with a 30 kDa cutoff spin concentrator and buffer exchanged with a PD-10 de-salting column into the low K^+ vesicle buffer (20 mM Tris, 1 mM KCl, 200 mM NaCl,

pH 7.4) supplemented with 1 mM DDM. The His-tag was cleaved by adding 0.5 mg of home-made TEV protease and incubating the mixture rotating overnight at 4 °C. After the TEV cleavage, KvAP with cleaved His-tag was purified by running the mixture through the Co column twice. The flow through was concentrated with a 30 kDa cutoff spin concentrator to 65 µL with a A280 absorbance of 6.31.

4.2.5.2 KvAP proteoliposome reconstitution

On the same day of KvAP Co affinity purification, 5 mg of POPC/POPG (3:1, w/w) lipids were dried in a desiccator. Purified KvAP in 1 mM DDM was further concentrated to ~30 µL. Lipids were rehydrated with 520 µL low K^+ vesicle buffer and vortexed with a mixer for ~25 min. The liposomes were homogenized by 5 cycles of freeze/thaw and 51 times extrusion with a 100 nm membrane. To 400 µL lipids, 20 µL of 10% DM stock (dissolved in ddH2O) was added to reach a final DM concentration of 10 mM and the mixture was rotated at 4 °C for 30min to solubilize the lipids. KvAP in DDM was then added and the mixture was rotated at 4 °C for 2 h for KvAP insertion into the lipid bilayer (lipid:protein ~ 9.5:1 w/w, 410:1 mol/mol). After incubation, detergents were removed by running the mixture through a BioRad ENrich™ SEC 650 10 x 300 Column. Peaks containing the proteoliposomes were combined and the proteoliposomes were pelleted via ultracentrifugation at 100,000 g at 4 °C for 1 h 5 min. The pellet containing KvAP proteoliposomes was resuspended with 150 µL of low K^+ vesicle buffer.

4.2.5.3 HDX-MS on KvAP

HDX for KvAP proteoliposomes follow the protocol described in Chapter 4.1.4 and Figure 4.4. Note that HDX was initiated within 24 h of reconstitution in vesicle buffers containing either low K^+ (20 mM Tris, 1 mM KCl, 200 mM NaCl, pD_{read} 7.0) or high K^+ (20 mM Tris, 200 mM KCl, 1 mM NaCl, pD_{read} 7.0) at room temperature.

4.2.6 Supplementary figures

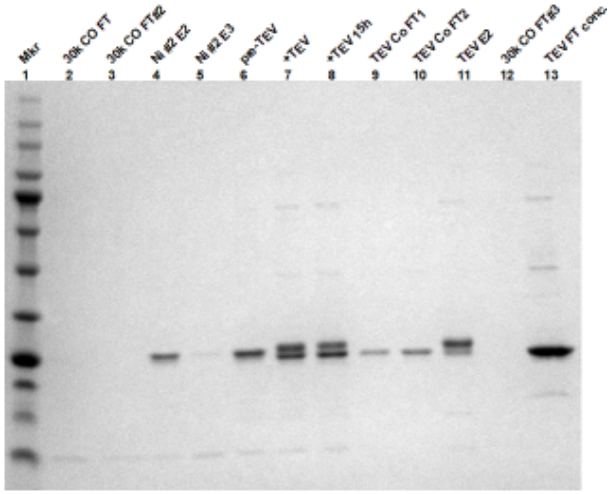

Figure 4.9: 4-20% gel for KvAP Co purification.

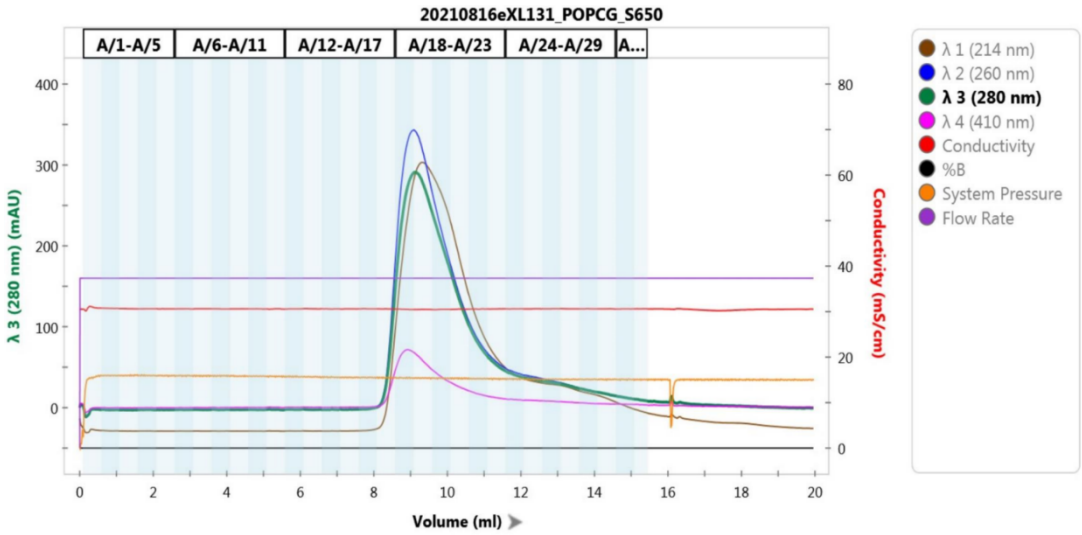

Figure 4.10: SEC chromatogram for liposome reconstitution of KvAP.

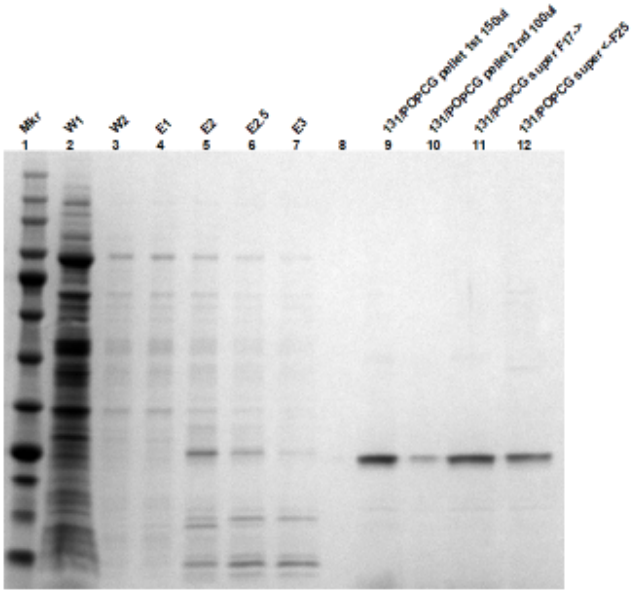

Figure 4.11: 4-20% gel for liposome reconstitution of KvAP (lanes 9-12).

5 EFFECTS OF BIOLOGICAL SOLVENTS ON THE FOLDING OF PROTEIN BACKBONES

5.1 Summary

This chapter describes work characterizing the solvent quality of water to polypeptide backbones as well as the effects of biological solvents on the folding of protein backbones. An IDP consisting of high glycine-content was used as a proxy for a polypeptide backbone. Chapter 5.2 details SAXS and HX/NMR measurements showing that polypeptide backbones did not promote contraction in a minimal buffer condition nor the presence of biological solvents. Chapter 5.3 summarizes how the work presented in Chapter 5.2 contributes to the large picture of the publication "How hydrophobicity, salt, and sidechains affect the dimensions of disordered proteins" by Baxa M., Lin X., et al., 2024.

5.2 Does a polypeptide backbone contract in water and in biological solvents?

5.2.1 Introduction

The notion that hydrophobic effects drive protein folding is widely accepted. However, many IDPs do not show contraction in an aqueous solvent and rather behave as self-avoiding random walk (SARW), including IDPs whose sequences contain similar hydrophobic content as those of folded proteins. Interestingly, snow flea anti-freeze protein (sfAFP), a protein containing 46% glycine and very few hydrophobic residues, folds in an oxidizing environment with six PP2 helices even in the absence of a hydrophobic core (Figure 5.1). These phenomena raise a few questions

regarding how proteins fold. Is water a good solvent for IDPs? Is hydrophobic effect sufficient to drive protein folding? Is contraction driven by side chains or polypeptide backbones? Do biological solvents promote contraction of IDPs?

In attempts to answer the above questions, I used the reduced form of sfAFP (red-sfAFP) as a proxy for polypeptide backbone and poly-glycine, and evaluated its extent of contraction and hydrogen-bonding patterns in a standard reductionist buffer and the presence of key biological solvents.

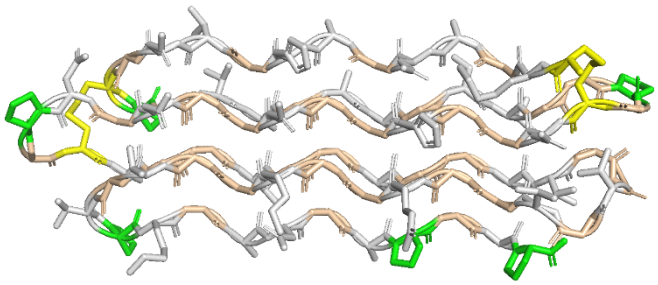

Figure 5.1: The crystal structure of sfAFP under oxidizing conditions (PDB 2PNE).
Tan: glycine residues; yellow: cysteine residues forming disulfide bonds; green: proline residues.

5.2.2 Results

To investigate whether the red-sfAFP adopted any residual structure, I performed circular dichroism (CD) on red-sfAFP. The CD spectrum exhibited characteristics of a fully unfolded protein without alpha-helical or beta-sheet features (Figure 5.2 A). NMR hetNOE measurements showed that all residues of red-sfAFP, including the glycine residues, exhibited nanosecond internal motion, a characteristic of disorder (Figure 5.2 B).

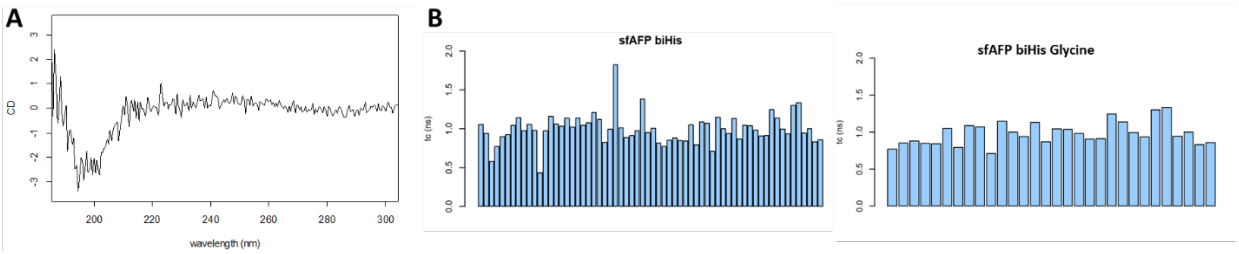

Figure 5.2: CD and NMR hetNOE measurements showing red-sfAFP is unfolded.

Early SEC-SAXS results suggested that although water is a good solvent for red-sfAFP, with a solvent quality ν of 0.539±0.00, red-sfAFP did not fully behave as a SARW at which a ν of 3/5 is expected. Such discrepancy in solvent quality suggested that red-sfAFP might form mild contraction in water. Additionally, polypeptide chains that are unstructured in a common reductionist buffer may behave differently in a physiological condition. For example, although NaCl is most widely used as a salt in buffers, the concentration of intracellular K^+ is in fact ~10-fold higher than that of Na^+.[93] Additionally, buffers commonly used in biochemical and biophysical studies do not contain key metabolites that may affect protein folding. It has also been reported that ATP acts as a key biological hydrotrope that assists protein folding in physiological conditions, which may explain why the concentration of ATP is in excess in cells.[94] Therefore, to answer the questions whether the low level of contraction we observed under SEC-SAXS in red-sfAFP was due to the formation of transient hydrogen bonds, and whether the presence of key biological solvents promote the contraction of a polypeptide backbone, I measured the millisecond H-to-H exchange using the NMR method "CLEANEX-PM" on red-sfAFP variants with different glycine stretches and under different buffer conditions.

Lyophilized 15N labeled red-sfAFP was dissolved in the following buffers: 1) “Standard buffer”: 50 mM KPi, 1 mM TCEP, pH 7.0; 2) “KGlu buffer”: 50 mM KPi, 1 mM TCEP, 20 mM NaCl, 50 mM KCl, 100 mM KGlutamate, 0.5 mM $MgCl_2$; 3) “KGlu/ATP” buffer: 50 mM KPi, 1 mM TCEP, 20 mM NaCl, 50 mM KCl, 100 mM KGlutamate, 0.5 mM $MgCl_2$, 10 mM ATP. The concentrations of each buffer component were determined based on current understanding of physiological concentrations.[93] Comparing hydrogen-bond patterns of red-sfAFP in these three buffers evaluated the effects of key biological solvents, including K^+, glutamate anions, divalent anions (Mg^{2+}), and ATP, on polypeptide backbones.

In agreement with the CD and NMR hetNOE results that red-sfAFP being unfolded, the $^1H^{15}N$-HSQC spectra of red-sfAFP showed little peak dispersion regardless of the presence of biological solvents (Figure 5.3 A). The HSQC spectra for red-sfAFP under the three buffers were indistinguishable, suggesting that no significant folding event was induced by the biological solvents. To investigate whether red-sfAFP forms any transient hydrogen bonds, I measured the millisecond H-to-H exchange using the NMR method “CLEANEX-PM”. The HX rates for red-sfAFP under all conditions tested were the same, including the glycine residues, suggesting that no additional hydrogen bond was formed in the presence of the biological solvents (Figure 5.3 B).

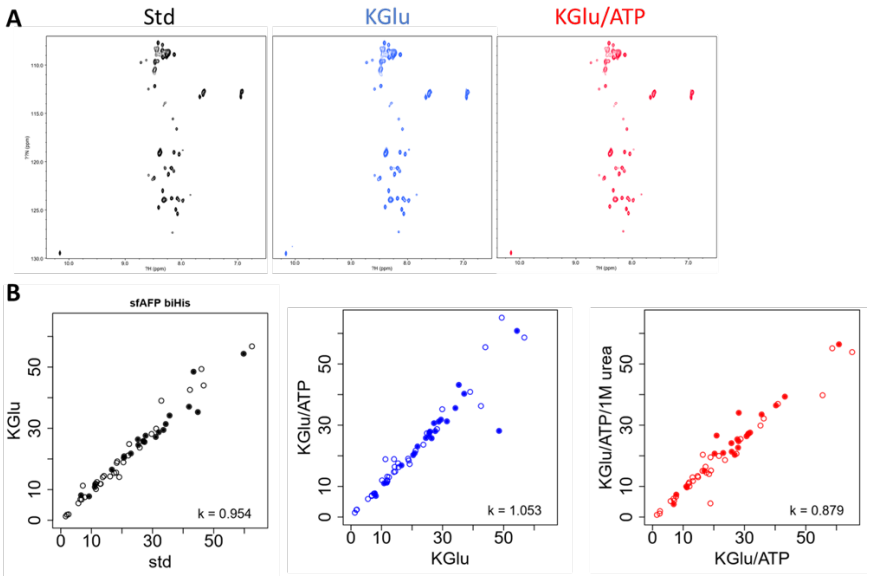

Figure 5.3: HSQC spectra and HX rates of red-sfAFP are unaffected by the presence of biological solvents.
(A) $^{1}H^{15}N$-HSQC spectra of red-sfAFP in the "Standard buffer", "KGlu buffer", and "KGlu/ATP" buffer. (B) Comparison of the HX rates measured by CLEANEX-PM for red-sfAFP in various buffers. The "KGlu/ATP/1 M urea" buffer contained the same composition as the "KGlu/ATP" buffer in addition to the presence of 1 M urea.

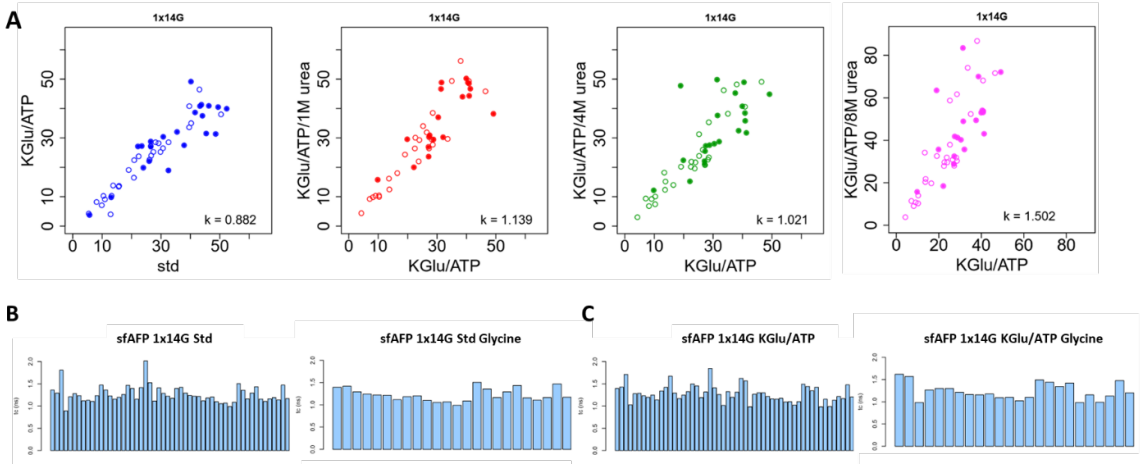

Figure 5.4: The glycine-clustered mutant of red-sfAFP did not form hydrogen-bonds and were unstructured.
(A) Comparison of the HX rates measured by CLEANEX-PM for the 1x14G mutant of red-sfAFP in various buffers. The "KGlu/ATP/4 M urea" and "KGlu/ATP/8 M urea" buffer contained the same composition as the "KGlu/ATP" buffer in addition to the presence of 4 M and 8 M urea, respectively. The plotted HX rates were not correct for the urea effects on k_{chem}. (B-C) The hetNOE measurements on 1x14G in the "Standard buffer" (B) and "KGlu/ATP" buffer (C).

Although we did not have assignments on which HSQC peak corresponded to which residue, the measured HX rates appeared to be 2-fold slower than the k_{chem} (Figure 5.7). Such protection of ~2 persisted even in the presence of 1 M urea (Figure 5.3B). Even though we could not identify the source of the observed protection, the fact that it was unaffected by urea suggested that it was unlikely due to the presence of residual hydrogen bonds.

To investigate whether a polypeptide backbone can drive contraction, we shuffled the sequence of red-sfAFP to create clusters of glycine residues while keeping the overall sequence composition unchanged (Figure 5.8). The new constructs were named "1x14G" and "3x7G", representing red-sfAFP with 14 consecutive glycine residues and red-sfAFP with 3 repeats of 7 consecutive glycine residues, respectively.

HX rates measured by CLEANEX-PM for 1x14G stayed the same under all buffer conditions tested, suggesting that polypeptide backbones do not drive the formation of hydrogen bonds in a reductionist buffer or the presence of biological solvents (Figure 5.4). The addition of 4 M or 8 M urea did not affect the exchange rates, after accounting for the slowing effect of urea on $k_{chem,}$[33] further supporting the absence of hydrogen bonds for the 1x14G red-sfAFP (Figure 5.4). Additionally, nanosecond internal motion for 1x14G was measured by hetNOE, consistent with the protein being unstructured (Figure 5.4). SAXS measurements showed that both 1x14G and 3x7G exhibited SARW, with a $\nu = 0.577\pm0.020$ and 0.576 ± 0.004 (Figure 5.5), suggesting the lack of contraction. Addition of 2 M Gdm increased the ν of 3x7G slightly to 0.603 ± 0.006 (Figure 5.5).

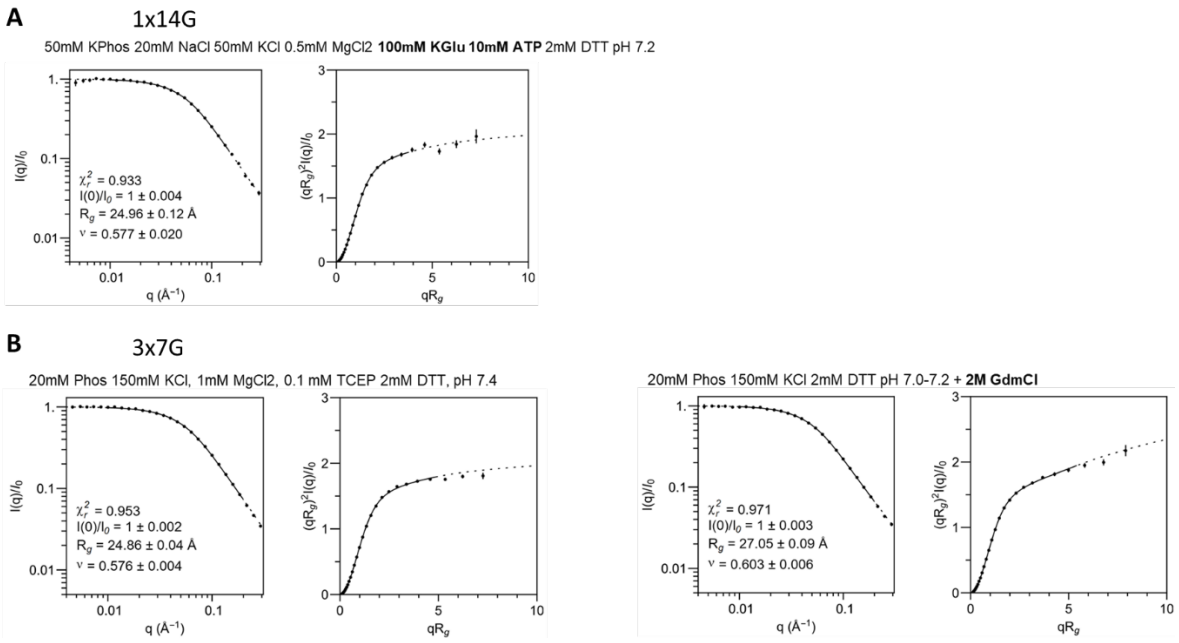

Figure 5.5: SAXS measurements on mutants of red-sfAFP containing various glycine stretches show SARW behaviors.
(A) 1x14G; (B) 3x7G. The buffers used were indicated in the figure.

5.2.3 Discussion

Red-sfAFP is a disordered protein with high glycine-content and no hydrophobic core. By measuring the hydrogen-bond stability and solvent quality of red-sfAFP, we show that it does not contract by forming backbone hydrogen bonds. This lack of contraction suggests that polypeptide backbones are not the major mediator to promote protein contraction for disordered proteins. This conclusion, together with our measurements of solvent quality for the other protein, PNt, contributes to the major conclusion of the publication "How hydrophobicity, salt, and sidechains affect the dimensions of disordered proteins" (Baxa, Lin, et al., 2024), which is discussed in Chapter 5.3.

5.2.4 Materials and methods

Detailed methods can be found in the “Materials & Methods” section of the publication “How hydrophobicity, salt, and sidechains affect the dimensions of disordered proteins” (Baxa, Lin, et al., 2024).

5.2.5 Supplementary figures

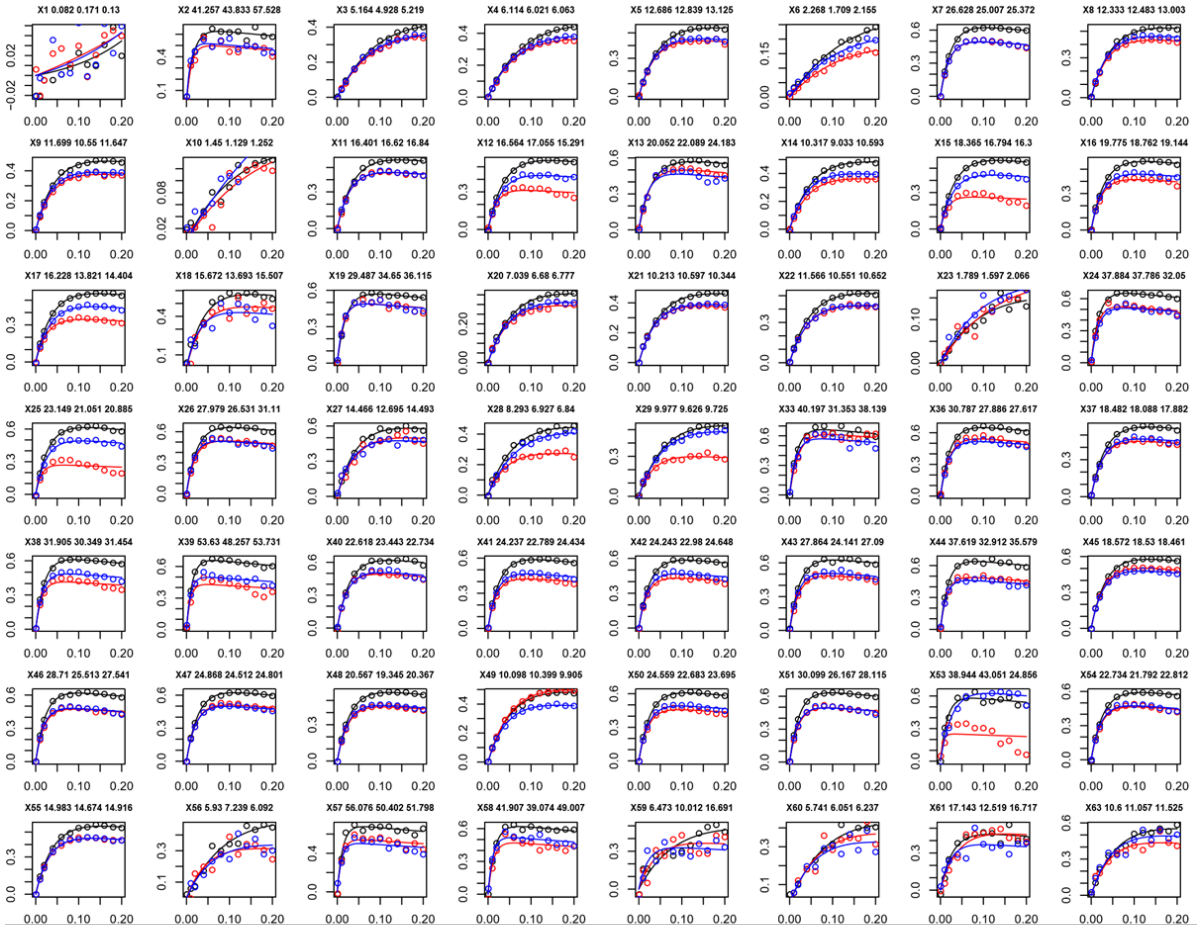

$$\frac{V}{V_0} = \frac{k}{(R_{1A,app} + k - R_{1B,app})} \times \{\exp(-R_{1B,app}\tau_m) - \exp[-(R_{1A,app} + k)\tau_m]\},$$

Figure 5.6: Fitting HX rates for the CLEANEX-PM measurements on red-sfAFP.
Black: the “Standard buffer”; blue: the “KGlu buffer”; red: the “KGlu/ATP” buffer. Circles: data points; lines: fitting based on the equation at the bottom of the figure.

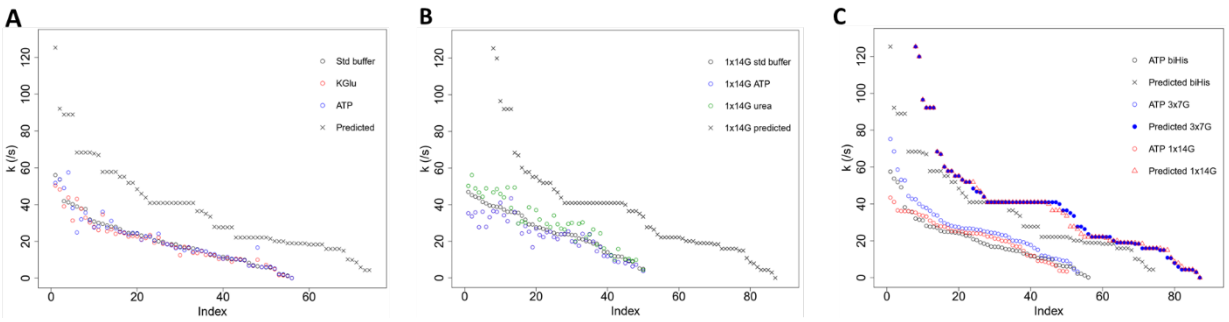

Figure 5.7: Protection factors for red-sfAFP are less than 2.

Super biHis:
SCKGADGADGVNGHPGDAGAAGSVGGPGCDGGHGGNGGNGNPGHAGGVGGAGGASGGTGNGGWGGKGGSGTPRGADGAPGAP

1x14G:
CKGADGAHGVNGCPGTAGAAGSVGGPGCDHNNGGGGGGGGGGGGGNPGCAVAASGTGVGGWGGKGGSGTPKGADGAPGAPGSHHWHHHHHH

3x7G:
CKGADGAHGVNGCPGTAGAAGSVGGPGCDHNNGGGGGGGNPGCAVAASGGGGGGGGTGVWKSGGGGGGGTPKGADGAPGAPGSHHWHHHHHH

Figure 5.8: Sequences of red-sfAFP and its variants used in this study.
"Super biHis" is the red-sfAFP construct used with wild type glycine residue patterns.

5.3 Contribution to the publication Baxa M., Lin X., et al., 2024

A fraction of the data presented in Chapter 5.2 is included in the publication by Baxa, Lin, et al., 2024, titled "How hydrophobicity, salt, and sidechains affect the dimensions of disordered proteins". Below summarizes the major conclusions of the publication and how work presented in Chapter 5.2 contributes to the big picture of understanding protein folding principles.

The observation that the HX/NMR results of red-sfAFP are indistinguishable in minimal buffer compared to biological buffer indicates that major biological solvents do not promote the formation of hydrogen bonds for the polypeptide backbone. SAXS studies showed that red-sfAFP persists as a SARW at elevated temperatures, in contrast to temperature-dependent contraction observed in an IDP consisting of sequences of a foldable protein, PNt (the N-terminal domain of

pertactin). Such difference between red-AFP and PNt suggests that the contraction of PNt under elevated temperatures is driven by interactions between hydrophobic side chains rather than the backbone. Overall, our results highlight that hydrophobic effect alone is insufficient to drive chain collapse and other stabilizing factors, such as hydrogen-bonds, are needed to stabilize proteins.

6 CONCLUSIONS AND FUTURE DIRECTIONS

By developing and applying HDX-MS and HX-NMR methods on various membrane proteins both *in vitro* and *in vivo*, we directly probed protein conformational fluctuations critical for function but invisible to most other structural approaches.

Prestin, the only piezoelectric member of the SLC26 family of anion transporters, exhibits conformational changes that underlie the acute hearing sensitivity for mammals. The major question remained in the field is what differentiates prestin as a motor protein from the highly homologous anion transporters having similar structural blueprints. Prestin's voltage-dependent conformational changes are driven by the putative displacement of residue Arg399 and other residues within the transmembrane domain, following the binding of a Cl^- anion at a conserved binding site formed by amino termini of the TM3 and TM10 helices. However, a major conundrum arises: How can a negatively charged anion that binds near, and in principle should neutralize the positively charged Arg399, actually promote prestin's voltage sensitivity? By comparing the energetic and conformational differences between prestin and its mammalian transporter relatives, we show that the conformational stability of the helices associated with the anion-binding site accounts, in large part, for prestin's distinct differentiation from its transporter-evolutionary origin. Cl^- binding to prestin is tightly coupled to the folding of the binding site, an event that is critical for areal expansion. The HDX-MS results, together with MD simulations, argue that the folding equilibrium of the anion-binding site plays a novel and central role in prestin's voltage-sensing mechanism and electromotility.

Despite the power of HDX-MS at probing protein dynamics, the reversible nature of HDX labels has largely limited the application to *in vitro* systems. Therefore, I developed the first

protocol for *in vivo* HDX-MS on membrane proteins and applied it to BtuB, a TonB-dependent B12 transporter found in *E. coli* outer membranes. HDX-MS measured in living *E. coli* cells showed that B12 alone is sufficient to break a critical salt bridge in BtuB, leading to the unfolding of the amino terminus for TonB binding. My *in vivo* HDX-MS results corroborate the conclusions from our previous *in vitro* HDX-MS study of the allostery initiated by B12 binding.

Additionally, *in vivo* HDX-MS conducted on Pab1 in live *E. coli* cells highlights a less dynamic RRM2 than purified Pab1, pointing to interactions in the cellular environment that are lost during purification. To fully understand Pab1's condensation mechanisms, further HDX-MS measurements will be carried out in yeast cells where native interactions with other cellular components are preserved. Other than BtuB and Pab1, HDX for a variety of endogenous *E. coli* proteins was also successfully measured. This suggests that the ability to measure HDX *in vivo* is generalizable which opens up a wide range of HDX studies on proteins in their native context.

Technical improvements on HDX-MS were investigated to push the technique to MPs in a more biologically relevant lipid environment. Compared to detergent micelles, nanodiscs and liposomes preserve more native MP dynamics and function. However, the presence of large amounts of lipids presents great challenges to proteolysis and LC-MS, issues that have hindered measurements with HDX-MS. We detailed optimizations on each component of the HDX-MS pipeline, including sample preparation, HDX, proteolysis, LC, and MS, to achieve optimal sequence coverage and signal-to-noise levels for MPs in lipid bilayers. The technique was applied to a voltage-dependent K^+ channel, KvAP, reconstituted in liposomes. By applying membrane potential through a K^+ gradient and ionophore, the thermodynamic responses of KvAP to voltage were measured.

How do biological solvents affect the folding of protein backbone? Millisecond H-to-H exchange on a glycine-rich disordered protein, red-sfAFP, indicates that major biological solvents do not promote the formation of hydrogen bonds for the polypeptide backbone.

In conclusion, my studies on prestin have deepened our understanding of mammalian hearing sensation. I have significantly advanced the utility of HDX-MS to *in vivo* systems and MPs embedded in lipid bilayers. Lastly, I have used HX methods on disordered proteins to study protein folding principles. Overall, my work on HDX-MS and MPs have advanced our knowledge of MP functions and mechanisms from a distinct thermodynamic perspective.

REFERENCES

1. Narang, D., Lento, C. & J. Wilson, D. HDX-MS: An Analytical Tool to Capture Protein Motion in Action. *Biomedicines* **8**, 224 (2020).
2. Eigen, M. Proton Transfer, Acid-Base Catalysis, and Enzymatic Hydrolysis. Part I: ELEMENTARY PROCESSES. *Angew. Chem. Int. Ed. Engl.* **3**, 1–19 (1964).
3. Eyring, H. The Activated Complex in Chemical Reactions. *J. Chem. Phys.* **3**, 107–115 (1935).
4. Claxton, D. P., Kazmier, K., Mishra, S. & Mchaourab, H. S. Navigating Membrane Protein Structure, Dynamics, and Energy Landscapes Using Spin Labeling and EPR Spectroscopy. in *Methods in Enzymology* vol. 564 349–387 (Elsevier, 2015).
5. Bai, Y., Milne, J. S., Mayne, L. & Englander, S. W. Primary Structure Effects on Peptide Group Hydrogen Exchange. *Proteins* **17**, 75–86 (1993).
6. Nguyen, D., Mayne, L., Phillips, M. C. & Englander, S. W. Reference parameters for protein hydrogen exchange rates. *J. Am. Soc. Mass Spectrom.* **29**, 1936–1939 (2018).
7. Walters, B. T., Mayne, L., Hinshaw, J. R., Sosnick, T. R. & Englander, S. W. Folding of a large protein at high structural resolution. *Proc. Natl. Acad. Sci.* **110**, 18898–18903 (2013).
8. Zhang, Y. *et al.* Pulsed hydrogen–deuterium exchange mass spectrometry probes conformational changes in amyloid beta (Aβ) peptide aggregation. *Proc. Natl. Acad. Sci.* **110**, 14604–14609 (2013).
9. Del Mar, C., Greenbaum, E. A., Mayne, L., Englander, S. W. & Woods, V. L. Structure and properties of -synuclein and other amyloids determined at the amino acid level. *Proc. Natl. Acad. Sci.* **102**, 15477–15482 (2005).

10. Chen, R. *et al. Sequential Activation and Local Unfolding Control Poly(A)-Binding Protein Condensation*. http://biorxiv.org/lookup/doi/10.1101/2022.09.21.508844 (2022) doi:10.1101/2022.09.21.508844.
11. Li, M. J., Guttman, M. & Atkins, W. M. Conformational dynamics of P-glycoprotein in lipid nanodiscs and detergent micelles reveal complex motions on a wide time scale. *J. Biol. Chem.* **293**, 6297–6307 (2018).
12. Redhair, M., Clouser, A. F. & Atkins, W. M. Hydrogen-deuterium exchange mass spectrometry of membrane proteins in lipid nanodiscs. *Chem. Phys. Lipids* **220**, 14–22 (2019).
13. Dallos, P., Zheng, J. & Cheatham, M. A. Prestin and the cochlear amplifier. *J. Physiol.* **576**, 37–42 (2006).
14. Sfondouris, J., Rajagopalan, L., Pereira, F. A. & Brownell, W. E. Membrane Composition Modulates Prestin-associated Charge Movement. *J. Biol. Chem.* **283**, 22473–22481 (2008).
15. Liberman, M. C. *et al.* Prestin is required for electromotility of the outer hair cell and for the cochlear amplifier. *Nature* **419**, 5 (2002).
16. Dong, X., Ospeck, M. & Iwasa, K. H. Piezoelectric Reciprocal Relationship of the Membrane Motor in the Cochlear Outer Hair Cell. *Biophys. J.* **82**, 1254–1259 (2002).
17. Bavi, N. *et al.* The conformational cycle of prestin underlies outer-hair cell electromotility. *Nature* **600**, 553–558 (2021).
18. Ge, J. *et al.* Molecular mechanism of prestin electromotive signal amplification. *Cell* **184**, 4669-4679.e13 (2021).
19. Butan, C. *et al.* Single particle cryo-EM structure of the outer hair cell motor protein prestin. *Nat. Commun.* 40 (2022).

20. Garaeva, A. A. & Slotboom, D. J. Elevator-type mechanisms of membrane transport. *Biochem. Soc. Trans.* **48**, 1227–1241 (2020).
21. Walter, J. D., Sawicka, M. & Dutzler, R. Cryo-EM structures and functional characterization of murine Slc26a9 reveal mechanism of uncoupled chloride transport. *eLife* **8**, e46986 (2019).
22. Chi, X. *et al.* Structural insights into the gating mechanism of human SLC26A9 mediated by its C-terminal sequence. *Cell Discov.* **6**, 55 (2020).
23. Oliver, D. *et al.* Intracellular Anions as the Voltage Sensor of Prestin, the Outer Hair Cell Motor Protein. *Science* **292**, 2340–2343 (2001).
24. Rybalchenko, V. & Santos-Sacchi, J. Cl− flux through a non-selective, stretch-sensitive conductance influences the outer hair cell motor of the guinea-pig. *J. Physiol.* **547**, 873–891 (2003).
25. Rybalchenko, V. & Santos-Sacchi, J. Anion Control of Voltage Sensing by the Motor Protein Prestin in Outer Hair Cells. *Biophys. J.* **95**, 4439–4447 (2008).
26. Song, L. & Santos-Sacchi, J. Conformational State-Dependent Anion Binding in Prestin: Evidence for Allosteric Modulation. *Biophys. J.* **98**, 371–376 (2010).
27. Bai, J.-P. *et al.* Prestin's Anion Transport and Voltage-Sensing Capabilities Are Independent. *Biophys. J.* **96**, 3179–3186 (2009).
28. Gorbunov, D. *et al.* Molecular architecture and the structural basis for anion interaction in prestin and SLC26 transporters. *Nat. Commun.* **5**, 3622 (2014).
29. Hamuro, Y. Quantitative Hydrogen/Deuterium Exchange Mass Spectrometry. *J. Am. Soc. Mass Spectrom.* **32**, 2711–2727 (2021).

30. Schaechinger, T. J. *et al.* A synthetic prestin reveals protein domains and molecular operation of outer hair cell piezoelectricity. *EMBO J.* **30**, 2793–2804 (2011).
31. Smit, J. H. *et al.* Probing Universal Protein Dynamics Using Hydrogen–Deuterium Exchange Mass Spectrometry-Derived Residue-Level Gibbs Free Energy. *Anal. Chem.* **93**, 12840–12847 (2021).
32. Santos-Sacchi, J. & Navaratnam, D. Physiology and biophysics of outer hair cells: The cells of Dallos. *Hear. Res.* 108525 (2022) doi:10.1016/j.heares.2022.108525.
33. Lim, W. K., Rösgen, J. & Englander, S. W. Urea, but not guanidinium, destabilizes proteins by forming hydrogen bonds to the peptide group. *Proc. Natl. Acad. Sci.* **106**, 2595–2600 (2009).
34. Ramesh, R. *et al.* Uncovering metastability and disassembly hotspots in whole viral particles. *Prog. Biophys. Mol. Biol.* **143**, 5–12 (2019).
35. Zmyslowski, A. M., Baxa, M. C., Gagnon, I. A. & Sosnick, T. R. HDX-MS performed on BtuB in E. coli outer membranes delineates the luminal domain's allostery and unfolding upon B12 and TonB binding. *Proc. Natl. Acad. Sci.* **119**, e2119436119 (2022).
36. Lin, X., Zmyslowski, A. M., Gagnon, I. A., Nakamoto, R. K. & Sosnick, T. R. Development of in vivo HDX-MS with applications to a TonB-dependent transporter and other proteins. *Protein Sci.* **31**, e4402 (2022).
37. Merkle, P. S. *et al.* Substrate-modulated unwinding of transmembrane helices in the NSS transporter LeuT. *Sci. Adv.* **4**, eaar6179 (2018).
38. Martens, C. *et al.* Direct protein-lipid interactions shape the conformational landscape of secondary transporters. *Nat. Commun.* **9**, 4151 (2018).

39. Schaechinger, T. J. & Oliver, D. Nonmammalian orthologs of prestin (SLC26A5) are electrogenic divalent/chloride anion exchangers. *Proc. Natl. Acad. Sci.* **104**, 7693–7698 (2007).

40. Muallem, D. & Ashmore, J. An Anion Antiporter Model of Prestin, the Outer Hair Cell Motor Protein. *Biophys. J.* **90**, 4035–4045 (2006).

41. Santos-Sacchi, J., Navarrete, E. & Song, L. Fast Electromechanical Amplification in the Lateral Membrane of the Outer Hair Cell. *Biophys. J.* **96**, 739–747 (2009).

42. Tan, X. *et al.* A motif of eleven amino acids is a structural adaptation that facilitates motor capability of eutherian prestin. *J. Cell Sci.* **125**, 1039–1047 (2012).

43. Tang, J., Pecka, J. L., Fritzsch, B., Beisel, K. W. & He, D. Z. Z. Lizard and Frog Prestin: Evolutionary Insight into Functional Changes. *PLoS ONE* **8**, e54388 (2013).

44. Hilser, V. J. & Thompson, E. B. Intrinsic disorder as a mechanism to optimize allosteric coupling in proteins. *Proc. Natl. Acad. Sci.* **104**, 8311–8315 (2007).

45. McPherson, D. R. Sensory Hair Cells: An Introduction to Structure and Physiology. *Integr. Comp. Biol.* **58**, 282–300 (2018).

46. Alvarez, F. J. D., Orelle, C. & Davidson, A. L. Functional Reconstitution of an ABC Transporter in Nanodiscs for Use in Electron Paramagnetic Resonance Spectroscopy. *J. Am. Chem. Soc.* **132**, 9513–9515 (2010).

47. Clark, M. D., Contreras, G. F., Bavi, N., Haller, P. R. & Perozo, E. An optimized protocol for on-column nanodisc formation. *Biophys. J.* **121**, 464a–465a (2022).

48. Masson, G. R. *et al.* Recommendations for performing, interpreting and reporting hydrogen deuterium exchange mass spectrometry (HDX-MS) experiments. *Nat. Methods* **16**, 595–602 (2019).

49. Warren, J. R. & Gordon, J. A. On the Refractive Indices of Aqueous Solutions of Urea. *J. Phys. Chem.* **70**, 297–300 (1966).

50. Hageman, T. S. & Weis, D. D. Reliable Identification of Significant Differences in Differential Hydrogen Exchange-Mass Spectrometry Measurements Using a Hybrid Significance Testing Approach. *Anal. Chem.* **91**, 8008–8016 (2019).

51. Jumper, J. M., Faruk, N. F., Freed, K. F. & Sosnick, T. R. Accurate calculation of side chain packing and free energy with applications to protein molecular dynamics. *PLOS Comput. Biol.* **14**, e1006342 (2018).

52. Jumper, J. M., Faruk, N. F., Freed, K. F. & Sosnick, T. R. Trajectory-based training enables protein simulations with accurate folding and Boltzmann ensembles in cpu-hours. *PLOS Comput. Biol.* **14**, e1006578 (2018).

53. Sali, A. & Blundell, T. L. Comparative protein modelling by satisfaction of spatial restraints. *J. Mol. Biol.* **234**, 779–815 (1993).

54. Lomize, A. L., Todd, S. C. & Pogozheva, I. D. Spatial arrangement of proteins in planar and curved membranes by PPM 3.0. *Protein Sci. Publ. Protein Soc.* **31**, 209–220 (2022).

55. Kimanius, D., Dong, L., Sharov, G., Nakane, T. & Scheres, S. H. W. New tools for automated cryo-EM single-particle analysis in RELION-4.0. *Biochem. J.* **478**, 4169–4185 (2021).

56. Punjani, A., Rubinstein, J. L., Fleet, D. J. & Brubaker, M. A. cryoSPARC: algorithms for rapid unsupervised cryo-EM structure determination. *Nat. Methods* **14**, 290–296 (2017).

57. Rosenthal, P. B. & Henderson, R. Optimal determination of particle orientation, absolute hand, and contrast loss in single-particle electron cryomicroscopy. *J. Mol. Biol.* **333**, 721–745 (2003).

58. Afonine, P. V. *et al.* Real-space refinement in PHENIX for cryo-EM and crystallography. *Acta Crystallogr. Sect. Struct. Biol.* **74**, 531–544 (2018).

59. Brown, A. *et al.* Tools for macromolecular model building and refinement into electron cryo-microscopy reconstructions. *Acta Crystallogr. D Biol. Crystallogr.* **71**, 136–153 (2015).

60. Pettersen, E. F. *et al.* UCSF ChimeraX: Structure visualization for researchers, educators, and developers. *Protein Sci. Publ. Protein Soc.* **30**, 70–82 (2021).

61. Weis, D. D., Wales, T. E., Engen, J. R., Hotchko, M. & Ten Eyck, L. F. Identification and characterization of EX1 kinetics in H/D exchange mass spectrometry by peak width analysis. *J. Am. Soc. Mass Spectrom.* **17**, 1498–1509 (2006).

62. Engen, J. R. & Komives, E. A. Complementarity of Hydrogen/Deuterium Exchange Mass Spectrometry and Cryo-Electron Microscopy. *Trends Biochem. Sci.* **45**, 906–918 (2020).

63. Keller, J. P. *et al.* Functional Regulation of the SLC26-Family Protein Prestin by Calcium/Calmodulin. *J. Neurosci.* **34**, 1325–1332 (2014).

64. Takahashi, S. *et al.* Deletion of exons 17 and 18 in prestin's STAS domain results in loss of function. *Sci. Rep.* **9**, 6874 (2019).

65. Engstrom, T. *et al.* High-resolution single-particle cryo-EM of samples vitrified in boiling nitro-gen. *IUCrJ* **8**, 867–877 (2021).

66. Lin, C.-W. & Gai, F. Microscopic Nucleation and Propagation Rates of an Alanine-Based α-Helix. *Phys. Chem. Chem. Phys. PCCP* **19**, 5028–5036 (2017).

67. Bock, L. V. & Grubmüller, H. Effects of cryo-EM cooling on structural ensembles. *Nat. Commun.* **13**, 1709 (2022).

68. Martens, C., Shekhar, M., Lau, A. M., Tajkhorshid, E. & Politis, A. Integrating hydrogen–deuterium exchange mass spectrometry with molecular dynamics simulations to probe lipid-modulated conformational changes in membrane proteins. *Nat. Protoc.* **14**, 3183–3204 (2019).
69. Lete, M. G. *et al.* Fast and slow biomembrane solubilizing detergents: Insights into their mechanism of action. *Colloids Surf. B Biointerfaces* **183**, 110430 (2019).
70. Lichtenberg, D., Ahyayauch, H. & Goñi, F. M. The Mechanism of Detergent Solubilization of Lipid Bilayers. *Biophys. J.* **105**, 289–299 (2013).
71. Möller, I. R. *et al.* Improving the Sequence Coverage of Integral Membrane Proteins during Hydrogen/Deuterium Exchange Mass Spectrometry Experiments. *Anal. Chem.* **91**, 10970–10978 (2019).
72. Adhikary, S. *et al.* Conformational dynamics of a neurotransmitter:sodium symporter in a lipid bilayer. *Proc. Natl. Acad. Sci.* **114**, E1786–E1795 (2017).
73. Majumdar, R. *et al.* Minimizing Carry-Over in an Online Pepsin Digestion System used for the H/D Exchange Mass Spectrometric Analysis of an IgG1 Monoclonal Antibody. *J. Am. Soc. Mass Spectrom.* **23**, 2140–2148 (2012).
74. Jia, R. *et al.* Hydrogen-deuterium exchange mass spectrometry captures distinct dynamics upon substrate and inhibitor binding to a transporter. *Nat. Commun.* **11**, 6162 (2020).
75. Cournia, Z. *et al.* Membrane Protein Structure, Function, and Dynamics: a Perspective from Experiments and Theory. *J. Membr. Biol.* **248**, 611–640 (2015).
76. Yang, M. & Brackenbury, W. J. Membrane potential and cancer progression. *Front. Physiol.* **4**, (2013).

77. Zhang, J., Chen, X., Xue, Y., Gamper, N. & Zhang, X. Beyond voltage-gated ion channels: Voltage-operated membrane proteins and cellular processes. *J. Cell. Physiol.* **233**, 6377–6385 (2018).

78. Bezanilla, F. How membrane proteins sense voltage. *Nat. Rev. Mol. Cell Biol.* **9**, 323–332 (2008).

79. Palovcak, E., Delemotte, L., Klein, M. L. & Carnevale, V. Evolutionary imprint of activation: The design principles of VSDs. *J. Gen. Physiol.* **143**, 145–156 (2014).

80. Englander, S. W. Hydrogen exchange and mass spectrometry: A historical perspective. *J. Am. Soc. Mass Spectrom.* **17**, 1481–1489 (2006).

81. Jaswal, S. S. Biological insights from hydrogen exchange mass spectrometry. *Biochim. Biophys. Acta BBA - Proteins Proteomics* **1834**, 1188–1201 (2013).

82. Jiang, Y. *et al.* X-ray structure of a voltage-dependent K+ channel. *Nature* **423**, 33–41 (2003).

83. Lee, S.-Y., Lee, A., Chen, J. & MacKinnon, R. Structure of the KvAP voltage-dependent K+ channel and its dependence on the lipid membrane. *Proc. Natl. Acad. Sci.* **102**, 15441–15446 (2005).

84. Tao, X. & MacKinnon, R. Cryo-EM structure of the KvAP channel reveals a non-domain-swapped voltage sensor topology. *eLife* **8**, e52164 (2019).

85. Perozo, E., Cortes, D. M. & Cuello, L. G. Three-dimensional architecture and gating mechanism of a K+ channel studied by EPR spectroscopy. *Nat. Struct. Biol.* **5**, 459–469 (1998).

86. Ruta, V., Chen, J. & MacKinnon, R. Calibrated Measurement of Gating-Charge Arginine Displacement in the KvAP Voltage-Dependent K+ Channel. *Cell* **123**, 463–475 (2005).

87. Holoubek, A., Večeř, J., Opekarová, M. & Sigler, K. Ratiometric fluorescence measurements of membrane potential generated by yeast plasma membrane H+-ATPase reconstituted into vesicles. *Biochim. Biophys. Acta BBA - Biomembr.* **1609**, 71–79 (2003).

88. Apell, H.-J. & Bersch, B. Oxonol VI as an optical indicator for membrane potentials in lipid vesicles. *Biochim. Biophys. Acta BBA - Biomembr.* **903**, 480–494 (1987).

89. Cuello, L. G., Cortes, D. M. & Perozo, E. Molecular Architecture of the KvAP Voltage-Dependent Kþ Channel in a Lipid Bilayer. **306**, 6 (2004).

90. Li, Q., Wanderling, S., Sompornpisut, P. & Perozo, E. Structural basis of lipid-driven conformational transitions in the KvAP voltage-sensing domain. *Nat. Struct. Mol. Biol.* **21**, 160–166 (2014).

91. Ruta, V., Jiang, Y., Lee, A., Chen, J. & MacKinnon, R. Functional analysis of an archaebacterial voltage-dependent K+ channel. *Nature* **422**, 180–185 (2003).

92. Studier, F. W. Protein production by auto-induction in high-density shaking cultures. *Protein Expr. Purif.* **41**, 207–234 (2005).

93. Philips, R. M. & R. » What are the concentrations of free metabolites in cells? http://book.bionumbers.org/what-are-the-concentrations-of-free-metabolites-in-cells/.

94. Patel, A. *et al.* ATP as a biological hydrotrope. *Science* **356**, 753–756 (2017).